

DEMONSTRATING GAS-PHASE HARVESTING CAPABILITIES AT THE NSCL
THROUGH THE PRODUCTION AND COLLECTION OF ^{76}Kr AND ^{77}Kr

By

Hannah Kaitlyn Clause

A DISSERTATION

Submitted to
Michigan State University
in partial fulfillment of the requirements
for the degree of

Chemistry – Doctor of Philosophy

2021

ABSTRACT

DEMONSTRATING GAS-PHASE HARVESTING CAPABILITIES AT THE NSCL THROUGH THE PRODUCTION AND COLLECTION OF ^{76}Kr AND ^{77}Kr

By

Hannah Kaitlyn Clause

The nearly completed Facility for Rare Isotope Beams (FRIB) operated by Michigan State University is expected to deliver beams of exotic nuclei for fundamental nuclear science research. As FRIB fulfills this mission, many other by-product radionuclides will be simultaneously produced that could be collected without interference to the primary experiment. These co-produced radionuclides will be available as both gaseous and dissolved species in various locations throughout FRIB, but particularly in the water-filled primary beam dump just after the production target. By recycling the water through a chemical system, it will be possible to collect the radionuclides through a process known as “isotope harvesting.”

In order to access the by-product radionuclides in the FRIB beam dump from both the aqueous and gaseous phases, a water-filled beam blocker and harvesting system have been developed and tested at the National Superconducting Cyclotron Laboratory (NSCL), a heavy-ion fragmentation facility similar to FRIB with less capabilities and lower beam intensities. Previous harvesting experiments at the NSCL focused on the feasibility of aqueous-phase harvesting of various radionuclides from different reaction and chemical systems; however, little research into the feasibility of simultaneously harvesting gaseous radionuclides from the system has been done.

To demonstrate gas-phase harvesting capabilities at the NSCL and the future FRIB, a gas processing line was designed to be implemented during a low-intensity 150 MeV/nucleon ^{78}Kr irradiation of water with the intent to collect ^{76}Kr and ^{77}Kr to use as generators for ^{76}Br and ^{77}Br ,

respectively. Before using the harvesting system in the ^{78}Kr irradiation, the durability of the materials and the chemical and physical behavior of the gas stream were tested during a low-intensity 140 MeV/nucleon ^{40}Ca irradiation. And following the ^{78}Kr irradiation, the chemical state of the gas stream was further analyzed during a high-intensity 140 MeV/nucleon ^{48}Ca irradiation. Through this work, target materials were tested, radiolysis products were measured, and the first true test of the gas-phase harvesting capabilities at the NSCL was demonstrated. The insight gained from the experiments described here will lead to successful gas-phase harvesting experiments at FRIB to produce and collect noble gas generators.

ACKNOWLEDGEMENTS

The simultaneous completion of this degree along with my Master's degree in Forensic Science would not have been possible without some really amazing people by my side along the way. First and foremost, I would like to thank my advisor, Dr. Greg Severin. I will be forever thankful that you took a chance on me and allowed me to be one of the founding members of your group. My graduate school journey would not have been the same without you in it. I have learned so much from you over the last five years – about realms of chemistry I had never imagined diving into, about what it takes to be a good professor and advisor, and about what is truly important in life. Thank you for creating an environment that was always inclusive, always understanding, and always fun. I would also like to thank the other members of my committee, Dr. Gary Blanchard, Dr. Dave Morrissey, and Dr. Ruth Smith, who have each had a large impact on my growth as a graduate student.

To my current and past colleagues of the isotope harvesting group, it has been amazing to get to know each and every one of you and watch this group grow: I am so proud to be a part of it. To Paige, thanks for being a great office-mate and conference buddy – we made some great memories together both in and out of the lab! Thank you Morgan, Wes, and Chloe for always providing helping hands during every experiment and for chatting about life in the downtime. Sam and Scott, thank you for taking the time to read through this thesis and provide feedback. I wish you both the best as you complete your degrees. And to Kathi, thank you immensely for all of your help during my krypton experiments and for all of your helpful suggestions and ideas.

A huge thank you to my best friend and partner in life, Cole. Thank you for sticking this out with me. I know it has been a roller coaster, but I could not have finished this without you by

my side. Thank you for always reminding me that I am up for the challenge, never passing up an adventure with me, and always buying me the best treats on the hard days. You are my favorite. To my work from home coworker and best pup around, Wrigley, thank you for always making sure there was time for playing, cuddles, and walks. You spread joy everywhere you go and have made this working from home (and overall graduate school) experience so much better.

And finally, thank you to my family and friends. The infamous Drug Squad, thank you both for becoming some of my best friends – even after moving away and starting new chapters. Our daily check-ins have kept me sane and never fail to bring a smile to my face on even the toughest days. I am so grateful that this graduate school journey brought us together. To Momma and Daddy, I can't thank either of you enough. From the days of building replicas of Grandfather Mountain in elementary school through all the many years of schooling that have brought us here, you have both instilled in me the meaning of hard work and never shying away from a challenge. Because of you, I never thought anything could be unobtainable or too difficult to achieve. Without you, I never would have believed in myself enough to try. Thank you for being my biggest cheerleaders through the most difficult five years of my life so far.

In loving memory of my Granny, I dedicate this dissertation to you as well. I finally completed them both and my only regret was that you weren't here to see me do it. Thank you for always believing in me and always pushing me to be the best version of myself – in school and in life. Love you Bunches.

“In their hearts humans plan their course, but the Lord establishes their steps.”

Proverbs 16:9

I am so grateful that God's plan for my life is bigger than my own. He is the Way Maker.

TABLE OF CONTENTS

LIST OF TABLES	ix
LIST OF FIGURES	x
I. Introduction	1
1.1 The Potential of Isotope Harvesting at FRIB	1
1.2 The Demonstration of Isotope Harvesting Capabilities at the NSCL	2
1.3 Gas-Phase Harvesting of Krypton Isotopes to Generate Bromine Daughters	5
1.3.1 Theranostic Applications of ^{76}Br and ^{77}Br in Nuclear Medicine	8
1.4 Research Objectives	11
REFERENCES	13
II. The Development and Evolution of the Isotope Harvesting System	18
2.1 First Iteration: Low Intensity ^{40}Ca Irradiation	21
2.1.1 Target Design	21
2.1.2 Water System	23
2.1.3 First Iteration of Water System Conclusions	29
2.2 Second Iteration: ^{78}Kr Irradiation	30
2.2.1 Target Design	30
2.2.2 Water System	33
2.2.3 Second Iteration of Water System Conclusions	38
2.3 Conclusions	39
REFERENCES	41
III. The Analysis of the Ti64 Target Material and Rate of Radiolysis Production during a ^{40}Ca Irradiation	44
3.1 Introduction	44
3.2 Materials and Methods	46
3.2.1 $^{40}\text{Ca}^{+20}$ Irradiation	46
3.2.2 Gaseous Isotope Collection	48
3.2.3 Radiolysis Product Determination	49
3.2.4 Surface Analysis of the Titanium Window	51
3.3 Results and Discussion	54
3.3.1 $^{40}\text{Ca}^{+20}$ Irradiation	54
3.3.2 Gaseous Isotope Collection	56
3.3.3 Radiolysis Product Determination	58
3.3.4 Surface Analysis	60
3.4 Conclusions	66
APPENDIX	69
REFERENCES	77

IV. The Investigation of Gas-Phase Harvesting Capabilities at the NSCL during a ^{78}Kr Irradiation.....	80
4.1 Introduction.....	80
4.2 Materials and Methods.....	81
4.2.1 ^{78}Kr Irradiation.....	81
4.2.2 $^{76,77}\text{Kr}$ Quantification and Qualification	83
4.2.3 Online Collection of $^{76,77}\text{Kr}$	87
4.2.4 Generation of $^{76,77}\text{Br}$ from $^{76,77}\text{Kr}$	88
4.2.5 Radioactive Bromine Elutions	91
4.3 Results and Discussion	92
4.3.1 ^{78}Kr Irradiation.....	92
4.3.2 $^{76,77}\text{Kr}$ Quantification and Qualification	93
4.3.3 Generation of $^{76,77}\text{Br}$ from $^{76,77}\text{Kr}$	96
4.3.4 Radioactive Bromine Elutions	99
4.4 Conclusions.....	101
APPENDIX.....	103
REFERENCES	105
V. Improvements to the System in Preparation for Gas-Phase Harvesting at FRIB	108
5.1 Introduction.....	108
5.2 Catalytic Recombination of Hydrogen and Oxygen	110
5.2.1 Hydrogen Recombiner Testing Materials and Methods	111
5.2.2 Hydrogen Recombiner Testing Results	113
5.2.3 Hydrogen Recombiner Testing Conclusions	117
5.3 Metal Organic Frameworks for Gas Collection.....	119
5.3.1 The Potential of SIFSIX-3-Cu MOF for Gas Collection	120
5.4 Conclusions.....	121
REFERENCES	122
VI. Conclusions and Future Work	124
6.1 Conclusions.....	124
6.2 Future Work	125
REFERENCES	128

LIST OF TABLES

Table 3.1: Gamma spectroscopy data obtained from sequential measurements of the soda lime trap over a period of 40 minutes	57
Table 3.2: The average hydrogen gas production and <i>apparent</i> G-values during each segment of irradiation	60
Table 3.3: Comparison of the semi-quantification of the elemental composition of the non-irradiated and irradiated Ti64 disks. All calculations are in weight percent.	66
Table 4.1: Volumes of water used to elute ^{76/77} Br isotopes from traps 1, 2, and 3.	91
Table 4.2: Activity calculated from the real-time gamma measurement results from the NPI detector. These activities were used to fit the mass transport model.	93
Table 4.3: Production and the location of online collection results of ⁷⁶ Kr and ⁷⁷ Kr*	96
Table 4.4: Total bromine activity measurements (kBq) resulting from elution rinses	101
Table 6.1: Examples of possible gaseous radioisotopes for harvesting at FRIB. ⁹	127

LIST OF FIGURES

Figure 1.1: Schematic of the Facility for Rare Isotope Beams⁴..... 1

Figure 1.2: Illustration of the A1900 Fragment Separator at the current NSCL. The solid target is positioned after the first dipole magnet in the A1900 to be replaced by the water-filled target.⁸ 3

Figure 1.3: A schematic representation of isotope harvesting from the NSCL. As the stable primary beam interacts with a foil target secondary beams are produced. A large portion of the primary beam is left unreacted is separated from the secondary beams in the A1900. Using a flowing-water target, desired radioisotopes can be harvested from the aqueous and gaseous phases..... 4

Figure 1.4: Representation of the decay schemes of ^{76/77}Kr to the ^{76/77}Br daughters including the half-lives of each radioisotope.^{20,21} 6

Figure 1.5: Predicted production of ^{76/77}Kr after 4 hours of irradiation at full beam power at the NSCL. This graph also shows the generation of ^{76/77}Br through the decay of the ^{76/77}Kr parents.. 7

Figure 1.6: Depiction of the ^{76/77}Kr/^{76/77}Br generator system if a transfer of the krypton gas is made 6 hours post-irradiation that demonstrates isolation of ⁷⁶Br. 8

Figure 2.1: A cross-sectional view of the FRIB harvesting beam dump design featuring the double-walled interior chamber. The blue arrow in part a represents the direction of the cylinder rotation and the red arrow represents the incoming beam. The arrows in part b represent the flow of water into (blue) and out of (red) the chamber 19

Figure 2.2: A schematic drawing of the target housing, specifically featuring the polyethylene chamber where the water entered the inlet on the bottom near the window and exited the outlet on top. The brackets shown in green simply supported the target chamber. 22

Figure 2.3: A schematic demonstrating the placement of the target at the end of the beam line. The beam exited the beam line vacuum through a thin window shown in orange. 22

Figure 2.4: Optical image of the irradiated Ti64 disk. In this image, the top half of the disk was left as the rough 3D-printed material and the bottom half was milled smooth..... 23

Figure 2.5: A schematic diagram of the order of the components included in the water system. Components in green involved a loop of the water reservoir which led into and out of the target. Components in blue included those that measured the condition of the water. Components in yellow included anything that removed radionuclides from the aqueous and gas phases. Finally, components in red involved those that removed and measured the gases in the system. 24

Figure 2.6: Flow patterns in the membrane contactor. 26

Figure 2.7: A schematic representation of the boric acid (left) and soda lime (right) traps used in the experiment. The traps were made using polypropylene tubing and compression fittings and were filled with the chemicals as well as glass wool.....	27
Figure 2.8: Images taken before the irradiation experiment of the target within secondary containment at the end of the beam line (a) and the water reservoir with components in additional secondary containment (b).....	28
Figure 2.9: A schematic drawing including measurements of the 3D-printed Ti64 target. In this drawing, water enters the target through the blue inlet tube, flows across the front face, and exits the target through the red outlet tube. The entire inner volume is filled with water. The beam enters the target from the left side.....	31
Figure 2.10: CT scan results of one of the 3D-printed Ti64 targets. These images show that the 3D printing process was successful at producing the thin-walled target with double-walled interior chamber at the front face.....	32
Figure 2.11: Image of the titanium blocker positioned in the beam line end station for irradiation. The beam enters normal to the front face.....	33
Figure 2.12: A schematic representation of the second iteration of the water system and the order of water and gas flow through the components in the system. This system consisted of four independent loops: 1) the target loop (red), 2) the aqueous chemistry loop (purple), 3) the hydrogen peroxide degradation loop (green), and 4) the gas line (blue).....	34
Figure 2.13: A detailed schematic of the order of the components used in the gas line portion of the second iteration of the water system.	36
Figure 2.14: A schematic representation of the cold traps used in the online collection – the two stainless steel cold traps on the left and in the middle and the glass collection vessel filled with molecular sieves on the right.	37
Figure 3.1: Depiction of the changes in beam energy as it traveled through the different material layers included in the target design. The ⁴⁰ Ca beam is represented by the black arrow as it passed through six layers of varying materials and distances. The beam energy decreased from 5.6 GeV as it entered the first layer to 5.5 GeV before it entered the Ti window, and ended at 5.0 GeV as it entered the water and traveled 11.6 mm into the water chamber.	47
Figure 3.2: Experimental G-values from Meesungnoen and Jay-Gerin which were used to estimate the production of H ₂ during the present experiment. ^{9,11-13}	50
Figure 3.3: Measurements of the pH probe, dissolved oxygen probe, conductivity probe, and temperature during the irradiation. The blue vertical line represents the start of beam time at low intensity, the yellow line represents the start of beam time at higher intensity, and the orange line represents the end of irradiation.....	55

Figure 3.4: Graphical representation of the exponential radioactive decay fit to the gamma measurements taken of the soda lime trap over a period of 40 minutes to determine the decay constant of the radionuclide emitting 511 keV gamma rays. The decay constant was consistent with that of ^{11}C	57
Figure 3.5: Depiction of the hydrogen sensor reading during irradiation. The segment highlighted in orange at the beginning corresponds to the period of low intensity irradiation. Each decrease in the graph to zero is due to interception of the beam by the Faraday cup.....	58
Figure 3.6: Experimental G-values used to estimate the H_2 production with the irradiation of 140 MeV/nucleon ^{40}Ca beam of approximately 700 keV/ μm LET.....	59
Figure 3.7: Side-by-side comparison of the digital and scintillation images of the titanium window disk demonstrating the location of the beam spot. The luminescence scale is uncalibrated and serves to show the relative intensity of the radioactivity. 61	61
Figure 3.8: SEM images in SEI and BEC mode of the non-irradiated and irradiated disk.	62
Figure 3.9: EDS images and elemental composition maps of the three elements included in the Ti64 alloy on the non-irradiated and irradiated disks.	64
Figure 3.10: Example EDS images and elemental composition maps of an area of debris on the Ti64 disk including the elements of the alloy as well as carbon and oxygen as the main components in the make-up of the debris.	65
Figure 3.11: Depiction of the regions used for the semi-quantitative measurement of the elemental composition.	66
Figure A.1: Example of the variety of signals produced by the interaction of an electron beam with a sample surface. The depth of the beam interaction with the sample to produce each type of signal is also demonstrated.	72
Figure A.2: Simple schematic of an SEM microscope and the components involved for imaging in both SEI and BEC modes.	74
Figure A.3: Representation of X-ray production within an atomic nucleus.....	75
Figure A.4: Simple schematic of the additional hardware included with the SEM microscope for EDS spectra collection.....	76
Figure 4.1: The result of the linear relationship between the current measured on the unsuppressed target and that measured on the more accurate Faraday cup. This was used to scale the target current measurements.	82
Figure 4.2: The observed beam current time structure during the irradiation. The average beam current was 1.9 pA.	82

Figure 4.3: Example of the images collected with the NPI detector of the (a) experimental set up and a (b) heat map of the radiation produced and collected in the system. The ROIs selected to determine counts of activity in the headspace and the tank, the traps, and background measurements are depicted by the yellow boxes. 84

Figure 4.4: Box diagram representing the mass transport model of krypton gas as it travelled through the system and gas line. 86

Figure 4.5: 1) The initial trap is cold, and the receiving trap is warm. 2) Both traps are cold and the valves between them are opened to allow gas transfer. 3) The initial trap is warmed, forcing gas into the receiving trap. In this process, the daughter $^{76/77}\text{Br}$ isotopes would remain in the initial trap and the parent $^{76/77}\text{Kr}$ isotopes would transfer to the receiving trap..... 88

Figure 4.6: Schematic of the three transfers which were performed in order to generate and isolate ^{76}Br from ^{77}Br 90

Figure 4.7: Example of the elution wash process of attaching a syringe of water to each trap and passing varying amounts of water through to a collection vessel..... 91

Figure 4.8: The hydrogen measurements during ^{78}Kr irradiation (blue points) compared to the corrected beam current time structure (red histogram). 92

Figure 4.9: The mass transport of ^{77}Kr was predicted (blue line) for different locations within the harvesting system – (a) the water and the headspace in the tank and (b) the traps. Real time data of the ^{77}Kr activity calculated from the gamma spectra from the NPI detector are shown (orange points) for comparison to the predictions. 94

Figure 4.10: The predicted mass transport of ^{76}Kr for different locations within the harvesting system – (blue) the total ^{76}Kr , (orange) the ^{76}Kr in the tank and the headspace of the tank, (green) the ^{76}Kr in collected on the traps..... 95

Figure 4.11: Example gamma-ray spectra (count time = 300 s) of stainless-steel trap 2 before (a) and after (b) the transfer of krypton gas to stainless steel trap 3. The successful movement of krypton gas due to changes in temperature is demonstrated by the decrease in counts of activity of ^{76}Kr and ^{77}Kr 97

Figure 4.12: Example gamma-ray spectra (count time = 300 s) of stainless steel trap 3 before (a) and after (b) the transfer of ^{76}Kr gas to stainless steel trap 4. The successful movement of krypton gas due to changes in temperature is demonstrated by the lack of counts of activity of ^{76}Kr 98

Figure 4.13: Gamma-ray spectrum (count time = 300 s) of stainless steel trap 3 after the transfer of ^{76}Kr gas to stainless steel trap 4. The successful movement of krypton gas due to changes in temperature is demonstrated by the lack of counts of activity of ^{76}Kr . The isolation of ^{76}Br is demonstrated. 99

Figure 4.14: Example gamma-ray spectra (count time = 300 s) of trap 1 before elution (a), the eluent from rinse 1 (b), the eluent from rinse 2 (c), and the trap after washing (d)..... 100

Figure 5.1: The measured percentages of hydrogen and oxygen during a ^{48}Ca high-intensity irradiation with the time structure of the beam current shown. 109

Figure 5.2: A simple schematic diagram of the small-scale water system used for testing of the catalytic hydrogen recombiner. The purple loop represents the flow of water and the blue line represents the flow of gas. 112

Figure 5.3: Results of the hydrogen concentration in the gas phase before (blue) and after (red) the catalyst in comparison to the oxygen concentration that passed through the catalyst (green). 114

Figure 5.4: Results of the oxygen concentration before (green) and after (purple) the catalyst in comparison to the hydrogen concentration that passed through the catalyst (red). 115

Figure 5.5: Demonstration of the relationship between decreasing output H_2 with increasing input O_2 concentration. (A) includes the data resulting from the first injection of H_2O_2 and (B) includes data from the second injection..... 116

Figure 5.6: The prediction of hydrogen concentration during the ^{48}Ca high-intensity irradiation with the use of the catalyst for hydrogen recombination in comparison to the measured values. 118

I. Introduction

1.1 The Potential of Isotope Harvesting at FRIB

The nearly complete Facility for Rare Isotope Beams (FRIB) at Michigan State University will provide the scientific community with a vast array of exotic radionuclides that can be utilized for a variety of different basic and applied science experiments.¹ The FRIB facility will consist of a superconducting cyclotron resonance (SC-ECR) ion source operating at 28 GHz and a superconducting-RF driver linear accelerator (LINAC) operating at 400 kW that is folded into three segments.^{2,3} Interactions between the primary beam and a thin production target will generate the secondary beam. A depiction of the facility is shown in Figure 1.1 below.

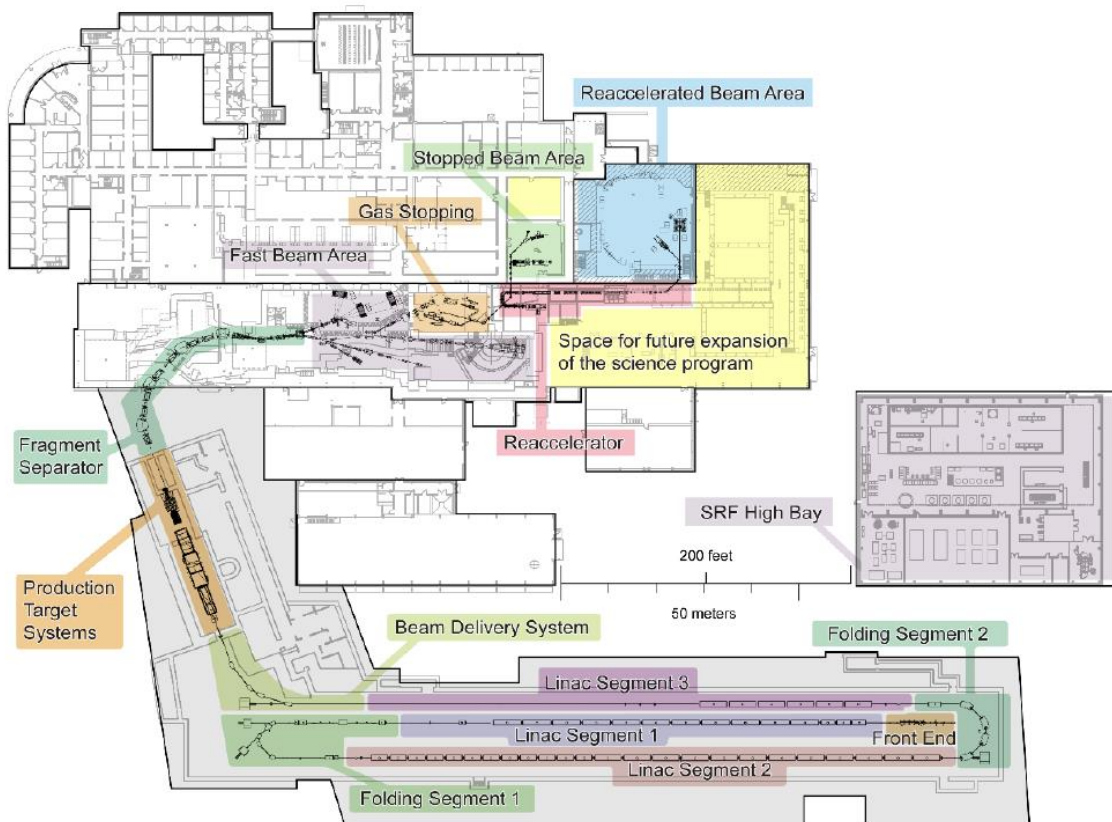


Figure 1.1: Schematic of the Facility for Rare Isotope Beams⁴

As FRIB fulfills its mission of providing rare isotope beams for fundamental nuclear science research, many useful by-product radionuclides will be formed by interactions of the primary beam with accelerator components and will be available as both gaseous and dissolved species at various locations throughout FRIB. Of particular interest are interactions between FRIB's primary heavy-ion beam and a water-filled beam dump right after the secondary beam production target that will produce a wide variety of radionuclides.⁵ When the beam dump water is recirculated through a chemical system, it is possible to collect the radionuclides through a process termed "isotope harvesting". Isotope harvesting has been identified as a source of otherwise-difficult-to-obtain radionuclides for use in basic and applied research.⁶

1.2 The Demonstration of Isotope Harvesting Capabilities at the NSCL

To test the proposed harvesting system to be used at FRIB, a similar system could be designed and implemented at the National Superconducting Cyclotron Laboratory (NSCL). Currently at the NSCL, reactions of heavy ion beams in beam stops produce radionuclides that would be valuable in research studies involving nuclear medicine amongst many other realms of science.⁵ These reactions include both fusion evaporation reactions, which occur at lower energy, and fragmentation reactions, which occur at higher energies. The NSCL facility contains two cyclotrons that are used to produce a primary beam of stable nuclei that are fragmented by sending the beam through a thin target of beryllium which produces a large variety of isotopes. These isotopes are filtered and collected using the A1900 Separator (Figure 1.2) and deliver a small percentage of them as the desired secondary beam of the exact isotope wanted for a research study. All other isotopes, along with the unused primary beam, are typically deposited into a solid beam blocker to decay away.⁷

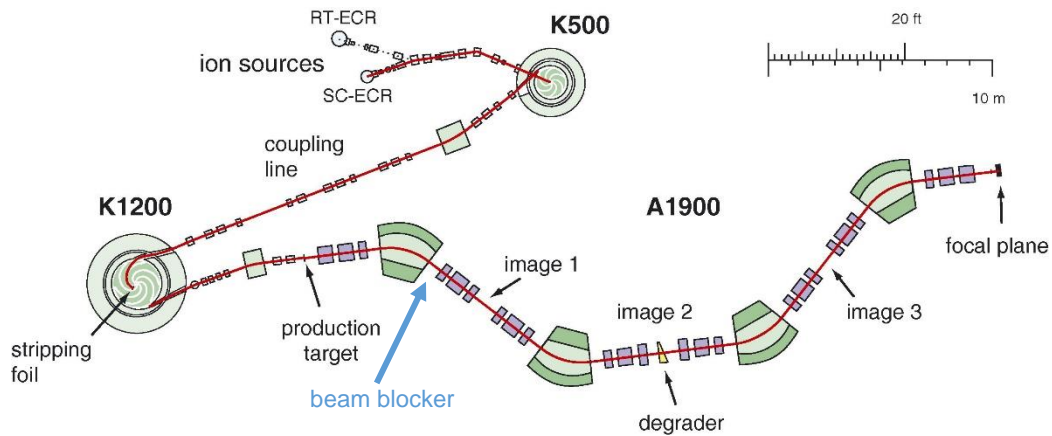


Figure 1.2: Illustration of the A1900 Fragment Separator at the current NSCL. The solid target is positioned after the first dipole magnet in the A1900 to be replaced by the water-filled target.⁸

By replacing the solid blocker with a newly developed water-filled beam blocker, it becomes possible to harvest radionuclides created by interactions with the mostly unused primary beam in a manner similar to the proposed FRIB beam dump. The use of a flowing-water target and water harvesting system makes the radionuclides mobile and remotely accessible in an aqueous state as well as creating the possibility for gas-phase extraction through sparging methods (Figure 1.3).⁹

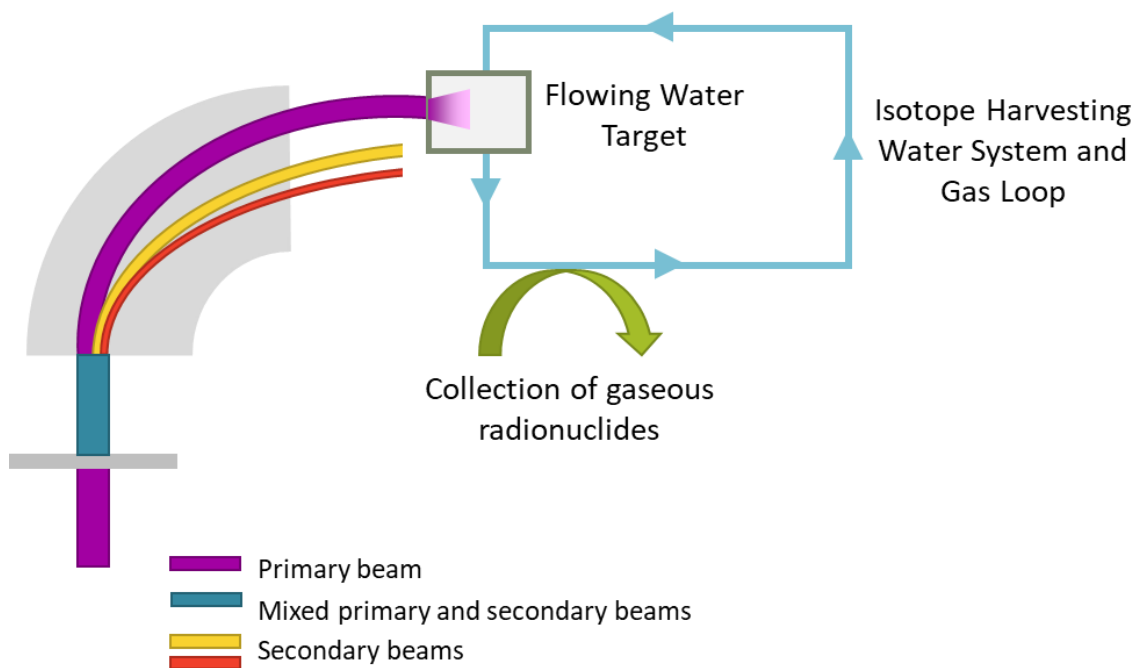


Figure 1.3: A schematic representation of isotope harvesting from the NSCL. As the stable primary beam interacts with a foil target secondary beams are produced. A large portion of the primary beam is left unreacted is separated from the secondary beams in the A1900. Using a flowing-water target, desired radioisotopes can be harvested from the aqueous and gaseous phases.

Several experiments have been performed in the past to demonstrate the feasibility of isotope harvesting in the aqueous phase from a nuclear physics accelerator facility that provides fast, heavy ion beams.¹⁰⁻¹⁵ The first proof-of-concept study that was performed at the NSCL involved a purified, fast ^{24}Na secondary beam collected in a small water volume. This experiment successfully demonstrated the ability to collect kBq quantities ^{24}Na .¹⁰ Other experiments demonstrated successful collection and purification of a ^{67}Cu secondary beam in the aqueous phase.¹² These experiments have demonstrated on a small scale the feasibility of using isotope harvesting from the aqueous phase as a production method for radionuclides with applications in nuclear medicine. However, in the past experiments performed at the NSCL, the primary focus has been on harvesting radioisotopes from the aqueous phase and not the gas

phase. With the novel beam blocker and water system design, simultaneous collection from both phases is possible.

1.3 Gas-Phase Harvesting of Krypton Isotopes to Generate Bromine Daughters

By instituting a gas processing line as a part of the water harvesting system, dissolved gases can be removed from the water through a carrier gas stream and collected in traps. Since this line is directly connected to the water system and aqueous harvesting loop, the simultaneous collection of by-product radioisotopes from the gas phase and aqueous phase can occur without interference. In order to prove the feasibility of gas-phase isotope harvesting using the water-filled target, a gas collection line was designed and tailored to harvest the noble gas, krypton. By utilizing a stable beam of ^{78}Kr , nuclear reactions between the beam and the water in the target will produce both ^{77}Kr and ^{76}Kr most abundantly.⁵ Henry's law (Equation 1.1),

$$c = k_H p \quad (\text{Equation 1.1})$$

states that the amount of dissolved gas in a liquid (c) is proportional to its partial pressure above the liquid (p) and its Henry's law coefficient (k_H). The produced $^{76/77}\text{Kr}$ gas can be easily sparged from the water as krypton is not highly soluble in water, i.e., k_H is small.¹⁶ The development of a gas processing line allows the produced activities of $^{76/77}\text{Kr}$ to be collected for use post-irradiation.

Potential trapping mechanisms for krypton gas include using stainless steel traps cooled with liquid nitrogen to trap gases with higher boiling points.¹⁷ Adding molecular sieves to the cold traps increase the trapping surface area and presumably increase the efficiency of collection. A more novel approach for noble gas collection and separation is the use of metal-organic frameworks (MOFs), which are a class of hybrid crystalline structures that consist of metal ions

coordinated to organic ligands.¹⁸ These structures can be tailor-made for particular uses and have demonstrated high trapping efficiencies without the assistance of cryogenic methods.¹⁹

Harvesting $^{76/77}\text{Kr}$ from the off-gas of the water-filled beam blocker and water system creates a pathway to producing other radioisotopes with important applications in nuclear medicine. Note that $^{76/77}\text{Kr}$ are the parent isotopes of $^{76/77}\text{Br}$, and through the use of a generator process, the harvesting system at the NSCL can provide a new method to produce these bromine radioisotopes (cf., Figure 1.4).

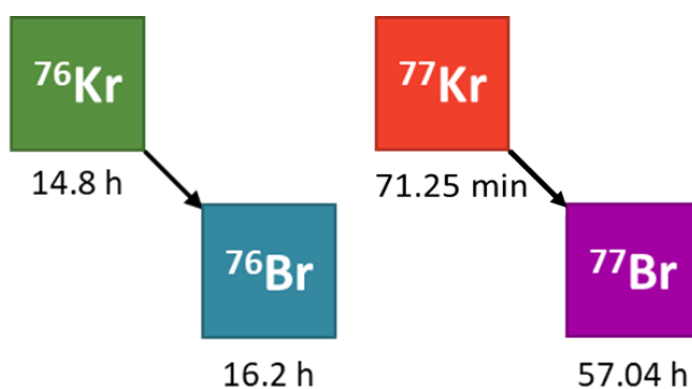


Figure 1.4: Representation of the decay schemes of $^{76/77}\text{Kr}$ to the $^{76/77}\text{Br}$ daughters including the half-lives of each radioisotope.^{20,21}

A $^{76/77}\text{Kr}/^{76/77}\text{Br}$ generator is a so-called “no-equilibrium generator” with ^{76}Kr having a slightly shorter half-life than the radioactive daughter, ^{76}Br . The general relationship of the activities can be seen in Figure 1.5.

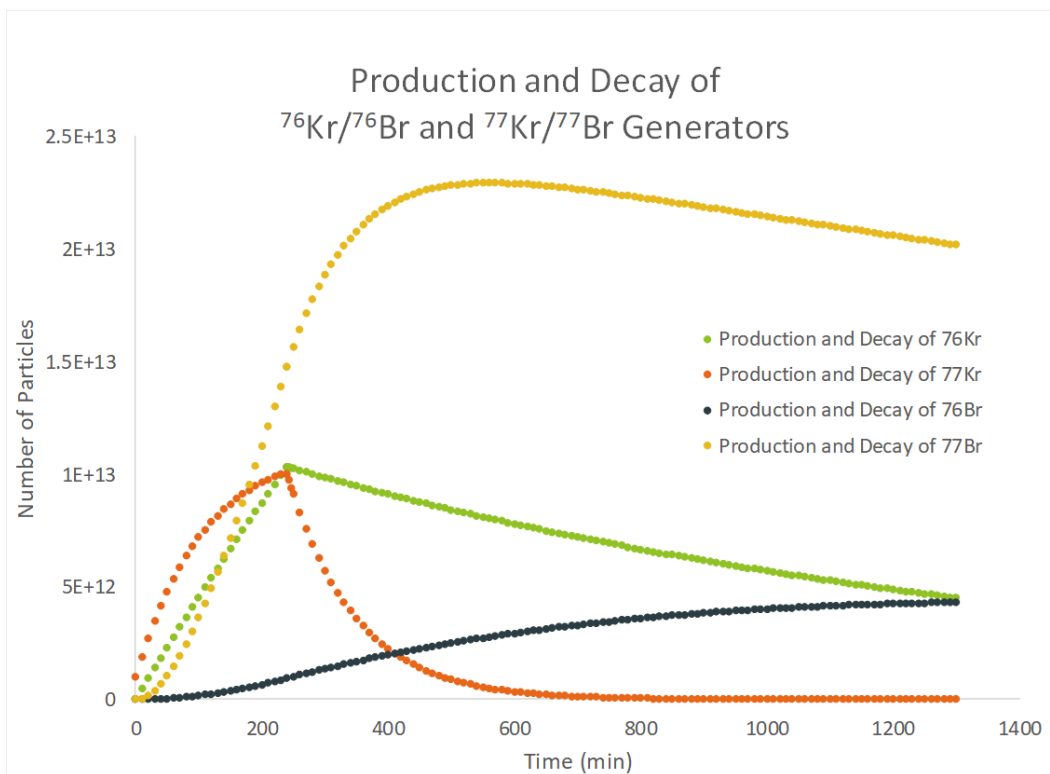


Figure 1.5: Predicted production of $^{76/77}\text{Kr}$ after 4 hours of irradiation at full beam power at the NSCL. This graph also shows the generation of $^{76/77}\text{Br}$ through the decay of the $^{76/77}\text{Kr}$ parents.

Both ^{76}Kr and ^{77}Kr will be produced simultaneously from the nuclear reactions in the water-filled target. As both daughters are medically relevant, contamination of either, which would reduce the radionuclidic purity of both $^{76/77}\text{Br}$, is unwanted. Contamination can be controlled by the differences in half-life of the two krypton radioisotopes – 14.8 h for ^{76}Kr and 71.25 min for ^{77}Kr .^{20,21} The ^{77}Kr will decay into ^{77}Br at a much faster rate than the $^{76}\text{Kr}/^{76}\text{Br}$ generator will be produced; therefore, allowing isolation of ^{76}Br . By trapping both ^{76}Kr and ^{77}Kr and making multiple transfers from the trap – the main transfer after the ^{77}Kr has decayed away (Figure 1.6) and one during the decay of ^{76}Kr , this generator system would lead to the purification of both isotopes. By producing ^{76}Br and ^{77}Br with high radionuclidic purity, this pair of isotopes can be utilized for important nuclear medicine research and applications.

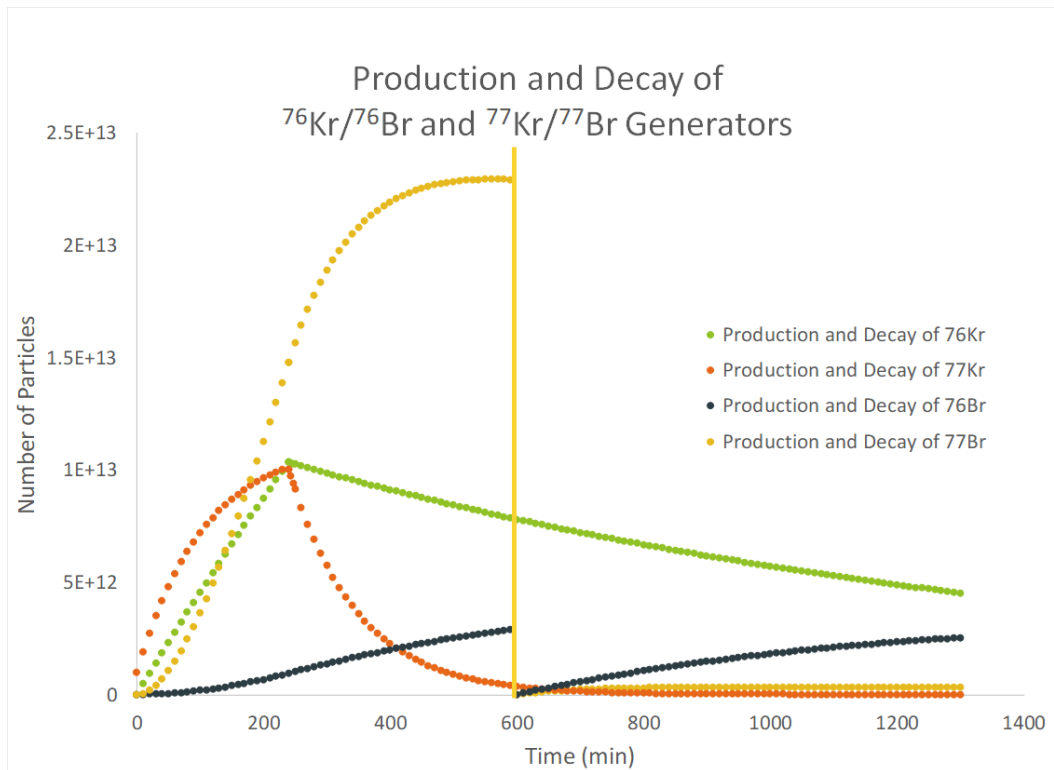


Figure 1.6: Depiction of the $^{76/77}\text{Kr}/^{76/77}\text{Br}$ generator system if a transfer of the krypton gas is made 6 hours post-irradiation that demonstrates isolation of ^{76}Br .

1.3.1 Theranostic Applications of ^{76}Br and ^{77}Br in Nuclear Medicine

Cancer is a major public health concern both at the national and international level due to its rank as a leading cause of death in every country in the world. Worldwide, there were approximately 19.3 million new cases of cancer in 2020, with an estimated 1.8 million new cases occurring in the United States. Cancer mortality in 2020 reached 10 million deaths worldwide and over 600,000 in the U.S.²²

Through the use of molecular imaging techniques, such as positron emission tomography (PET) imaging, the death rates of cancer have been dropping since the early 1990s.²³ In addition, the five-year survival rates have been increasing due to these advancements. These statistics

represent the positive impact that PET imaging has had on the early detection of cancer and the role targeted radiotherapy has played in successful treatment.

An important novel advancement in nuclear medicine includes theranostic techniques, which utilize different isotopes of the same element for therapy and diagnosis. These ideal theranostic pairs have the same chemistry for radiolabeling imaging agents as well as radiopharmaceuticals and will interact similarly within the body.²⁴ During the diagnostic imaging step, which typically uses low doses, the biodistribution and dosimetry of the radionuclide in a specific patient can be determined before increasing the dose for radiotherapy using an identical imaging agent in the body.²⁵ Because of this behavior, theranostics make the procedures safer by reducing the potential of unwanted biological effects when diagnosing and treating cancer with different imaging agents which may interact differently. One such theranostic pair is $^{76/77}\text{Br}$ and both isotopes can be generated from the harvested $^{76/77}\text{Kr}$ radioisotopes from the NSCL and later at FRIB. Bromine-76 produces positrons as it decays and is useful as a PET imaging tracer, whereas, ^{77}Br is an Auger electron emitter which has promise for therapy in small disseminated tumors.²⁶⁻²⁸

These isotopes of bromine possess many advantageous properties in imaging and therapy, especially in comparison to other medically relevant radiohalogens like ^{18}F and ^{124}I .²⁶ The longer half-lives of ^{76}Br and ^{77}Br make the delivery of the isotopes from one facility to another more feasible and broadens the scope of applications to those that require more time. For radiolabeling purposes, bromine creates a stronger bond than other radiohalogens with carbon present in organic molecules typical of pharmaceuticals and chelators.²⁹ Bromine does not accumulate in the thyroid or the gastrointestinal tract, like ^{124}I , but is instead freely distributed in the extracellular space.³⁰ And while most of the positrons that are emitted from ^{76}Br have high

energy ($E_{\max} = 3.98 \text{ MeV}$) which is disadvantageous for resolution in PET imaging as well as dosimetry, around 57% of the decay is positron emission, higher than the comparable ^{124}I halogen.³¹ Due to these properties, ^{76}Br and ^{77}Br have been used to radiolabel many types of molecules including proteins that have longer biological half-lives, antibodies to visualize tumors with PET, and radiopharmaceuticals for targeted treatment.²⁶⁻²⁸

In addition to the multitude of properties that make this theranostic pair useful for imaging and therapy, the isotopes of bromine contain chemical and physical properties that simplify the radiolabeling process. Radiolabeling with this halogen can be done in several ways, but the most common is the Chloramine-T (*N*-chlorotoluenesulfonamide) method.³² Chloramine-T is a strong oxidizing agent that allows for the formation of an electrophilic halogen species that results in the incorporation of the radioactive bromine into the molecule of interest.³²

Since there is an established need for the theranostic pair of ^{76}Br and ^{77}Br , it is important to find a way to produce them. There are many different possible methods of ^{76}Br and ^{77}Br that have been used in the past. Some methods produce the isotopes of interest directly, including from enriched selenium targets ($^{76}\text{Se}(p, n)^{76}\text{Br}$ or $^{77}\text{Se}(p, n)^{77}\text{Br}$).³³ These methods require the distillation of Br from the solid target through either acidic or thermal conditions, which have not been widely adopted for clinical radiopharmaceutical use.³⁴ An alternative method involves indirect production through the decay of krypton parents. One such approach was pursued in the 1970's by Tomechev and coworkers, which was based upon high-energy irradiation of bromide salts to create radiokryptons which could then be used as generators.³⁵ Importantly, they found that the formation of generators from the shorter lived ^{76}Kr and ^{77}Kr parents (14.8 h, and 1.24 h respectively) made it possible to isolate and use the radioactive daughters for different applications, including radiolabeling peptides and antibodies.

Because of the important diagnostic capabilities of ^{76}Br and the therapeutic potential of ^{77}Br , along with the lack of an efficient production method, the development of a novel technique to harvest and generate the isotopes has potential to lead to research opportunities in many areas of science, clinical studies, and applications in human nuclear medicine.

1.4 Research Objectives

The purpose of this research was to develop an experimental system that could be implemented at the NSCL to harvest radioisotopes of krypton in order to demonstrate the gas-phase harvesting capabilities at the future FRIB facility utilizing a similar system. In order to create a successful harvesting system, the chemical environment of the aqueous phase and the chemical and physical behavior of the gas phase were determined through a series of irradiation experiments with increasing beam intensity. Corrosion resistant materials were used in the design of the beam blocker in order to withstand the irradiation conditions and the materials were tested to establish chemical resistance and durability against degradation. The harvesting system was designed to include probes for measurements of the conductivity, dissolved oxygen, and hydrogen concentration. And a gas processing line was developed, which included a series of cold traps, and methods for controlling the gas stream to increase collection efficiency of the desired isotopes were investigated.

After a successful harvesting system was developed and tested, an irradiation experiment to test this production method of $^{76/77}\text{Kr}$ was performed. The production rates of $^{76/77}\text{Kr}$ per incident particle were calculated and a model to predict the movement of the krypton gas through the system was developed. Post-irradiation, a successful method to generate and cryogenically isolate ^{76}Br from ^{77}Br was developed. Following the testing of the gas harvesting line, improvements to the system were determined and initial testing was performed. The techniques

and knowledge gained through these experiments successfully demonstrated gas-phase harvesting capabilities at the NSCL and showed the potential of harvesting other noble gases on a larger scale at FRIB in the future.

REFERENCES

REFERENCES

- 1) Gade, A.; Sherrill, B. M. NSCL and FRIB at Michigan State University: Nuclear Science at the Limits of Stability. *Phys. Scr.* **2016**, *91* (5), 053003
- 2) Machicoane, G.; Felice, H.; Fogfeman, J.; Hafalia, R.; Morgan, G.; Pan, H.; Prestemon, S.; Pyzdeyev, E.; Rao, X.; Ren, H.; Tobos, L. Status of ECR Ion Sources for the Facility for Rare Isotope Beams (FRIB). *Review of Scientific Instruments*, **2016**, *87*, 02A743.
- 3) Wrede, C. The Facility for Rare Isotope Beams. *EPJ Web of Conferences*, **2015**, *93*, 07001.
- 4) Facility for Rare Isotope Beams [Online]. Available: www.frib.msu.edu/about (Accessed 2021)
- 5) Avilov, M.; Aaron, A.; Amroussia, A.; Bergez, W.; Boehlert, C.; Burgess, T.; Carroll, A.; Colin, C.; Durantel, F.; Ferrante, P.; Fourmeau T.; Graves, V.; Grygiel, C.; Kramer, J.; Mittig, W.; Monnet, I.; Patel, H.; Pellemoine F.; Ronningen R.; Schein, M. Thermal, Mechanical, and Fluid Flow Aspects of the High Power Beam Dump for FRIB. *Nuclear Instruments and Methods in Physics Research Section B. Interactions with Materials and Atoms*. 2016, *376*, 24-27.
- 6) Abel, E. P.; Avilov, M.; Ayres, V.; Birnbaum, E.; Bollen, G.; Bonito, G.; Bredeweg, T.; Clause, H.; Couture, A.; DeVore, J.; Dietrich, M.; Ellison, P.; Engle, J.; Ferrieri, R.; Fitzsimmons, J.; Friedman, M.; Georgobiani, D.; Graves, S.; Greene, J.; Lapi, S.; Loveless, C. S.; Mastren, T.; Martinez-Gomez, C.; McGuinness, S.; Mittig, W.; Morrissey, D.; Peaslee, G.; Pellemoine, F.; Robertson, J. D.; Scielzo, N.; Scott, M.; Severin, G.; Shaughnessy, D.; Shusterman, J.; Singh, J.; Stoyer, M.; Sutherlin, L.; Visser, A.; Wilkinson, J. Isotope Harvesting at FRIB: Additional Opportunities for Scientific Discovery. *J. Phys. G Nucl. Part. Phys.* **2019**, *46* (10), 100501
- 7) National Superconducting Cyclotron Laboratory [Online]. <https://www.nsl.msu.edu> (Accessed 2021)
- 8) Morrissey, D. J.; Sherrill, B. M. *Philos. Trans. R. Soc. Lond. Ser. A. Math. Phys. Eng. Sci.*, **1998**, *356*, 1985.
- 9) Domnanich, K. A.; Abel, E. P.; Clause, H. K.; Kalman, C.; Walker, W.; Severin, G. W. An Isotope Harvesting Beam Blocker for the National Superconducting Cyclotron Laboratory. *Nucl. Instruments Methods Phys. Res. Sect. A Accel. Spectrometers, Detect. Assoc. Equip.* **2020**, *959* (November 2019), 163526.

- 10) Pen, A.; Mastre, T.; Peaslee, G. F.; Petrasky, K.; Deyong, P. A.; Morrissey, D. J.; Lapi, S. E. Design and construction of a water target system for harvesting radioisotopes at the National Superconducting Cyclotron Laboratory. *Nucl. Instruments Methods Phys. Res. Section A. Accelerators and Spectrometers*. **2014**, *747*, 62-68.
- 11) Mastren, T.; Pen, A.; Peaslee, G. F.; Wozniak, N.; Loveless, S.; Essenmacher, S.; Sobotka, L. G.; Morrissey, D. J.; Lapi, S. E. Feasibility of isotope harvesting at a projectile fragmentation facility: ^{67}Cu . *Scientific Reports*, **2014**, *4*, 1-6.
- 12) Mastren, T.; Pen, A.; Loveless, S.; Marquez, B. V.; Bollinger E.; Marois, B.; Hubley, N.; Brown, K.; Morrissey, D. J.; Peaslee, G. F.; Lapi, S. E. Harvesting ^{67}Cu from the Collection of a Secondary Beam Cocktail at the National Superconducting Cyclotron Laboratory. *Analytical Chemistry*, **2015**, *87*, 10323-10329.
- 13) Loveless, C. S.; Marois, B. E.; Ferran, S. J.; Wilkinson, J. T.; Sutherlin, L.; Severin, G.; Shusterman, J. A.; Scielzo, N. D.; Stoyer, M. A.; Morrissey, D. J.; Robertson, J. D.; Peaslee, G. F.; Lapi, S. E. Harvesting ^{48}V at the National Superconducting Cyclotron Laboratory. *Applied Radiation and Isotopes*, **2020**, *157*, 109023.
- 14) Abel, E. P.; Clause, H. K.; Severin, G. W. Radiolysis and Radionuclide Production in a Flowing-Water Target during Fast $^{40}\text{Ca}^{20+}$ Irradiation. *Appl. Radiat. Isot.* **2020**, *158* (January), 109049.
- 15) Domnanich, K. A.; Vyas, C. K.; Abel, E. P.; Kalman, C.; Walker, W.; Severin, G. W. Harvesting ^{62}Zn from an Aqueous Cocktail at the NSCL. *New J. Chem.* **2020**, *44*, 20861 – 20870.
- 16) Sander, R. Compilation of Henry's law constants (version 4.0) for water as solvent. *Atmospheric Chemistry and Physics*, **2015**, *15*, 4399-4981.
- 17) Visser, A.; Scielzo, N.; Sangiorgio, S.; Severin, G. In *Feasibility of Harvesting Radon and Noble Gas Isotopes from the FRIB Beam Dump*; Proceedings of the Spring 2018 ACS Meeting; New Orleans, **2018**.
- 18) Banerjee, D.; Thallapally, P. K.; et al. Potential of Metal Organic Frameworks for Separation of Xenon and Krypton. *Accounts of Chemical Resesarch*. **2014**, *48* (2), 211-219.
- 19) Parkes, M. V.; Staiger, C. L.; Perry IV, J. J.; Allendorf, M. D.; Greathouse, J. A. Screening metal-organic frameworks for selective noble gas adsorption in air: effect of pore size and framework topology. *Phys. Chem. Chem. Phys.* **2013**, *15*, 9093 – 9106.
- 20) Singh, B. Nuclear Data Sheets Update for A=76. *Nuclear Data Sheets*. **1995**, *74*, 63.
- 21) Singh, B.; Nica, N. Nuclear Data Sheets for A=77. *Nuclear Data Sheets*. **2012**, *113*, 1115-1314.

- 22) National Cancer Institute: Understanding Cancer and Cancer Statistics Page. <https://www.cancer.gov/about-cancer/understanding/statistics>. (accessed 2021).
- 23) Society of Nuclear Medicine and Molecular Imaging: Molecular Imaging and Cancer Page. <http://www.snmmi.org/AboutSNMMI/>. (accessed 2021).
- 24) Fani, M.; Del Pozzo, L.; Abiraj, K.; Mansi, R.; Tamma, M. L.; Cescato, R.; Waser, B.; Webe, W. A.; Reubi, J. C.; Maecke H. R. PET of somatostatin receptor-positive tumors using ^{64}Cu - and ^{68}Ga -somatostatin antagonists: the chelate makes the difference. *Journal of Nuclear Medicine*, **2011**, 52 (7), 1110-1118.
- 25) Srivastava, S. C. Paving the way to personalized medicine: production of some promising theragnostic radionuclides at Brookhaven National Laboratory. *Seminars in Nuclear Medicine*, **2012**, 42 (3), 151-163.
- 26) Mason, N. S.; Mathis, C. A. Radiohalogens for PET Imaging. In *Positron Emission Tomography: Basic Science and Clinical Practice*; Valk, P. E.; Bailey, D. L.; Townsend, D. W.; Maisy, M. N. Springer-Verlag: London 2003; 217-236.
- 27) Glaser, M.; Luthra, S. K.; Brady, F. Applications of positron-emitting halogens in PET oncology (Review). *Int. J. Oncol.* **2003**, 22, 253 – 267.
- 28) Stepanek, J.; Larsson, B.; Weinreich, R. Auger-Electron Spectra of Radionuclides for Therapy and Diagnostics. *Acta Oncologica*. **1996**, 35 (7), 863 – 868.
- 29) Scott-Robson, S.; Capala, J.; Carlsson, J.; Malmberg, P.; Lundqvist, H. Distribution and Stability in the Rat of a $^{76}\text{Br}/^{125}\text{I}$ -labelled Polypeptide, Epidermal Growth Factor. *Nuclear Medicine and Biology*, **1991**, 18 (2), 241 – 246.
- 30) Hanaoka, H.; et al. Development of a Widely Usable Amino Acid Tracer: ^{76}Br - α -Methyl-Phenylalanine for Tumor PET Imaging. *Journal of Nuclear Medicine*, **2015**, 56 (5), 791 – 797.
- 31) Lovqvist, A.; Sundin, A.; Ahlstrom, H.; Carlsson, J.; Lundqvist, H. Pharmacokinetics and Experimental PET Imaging of a Bromine-76-Labeled Monoclonal Anti-CEA Antibody. *Journal of Nuclear Medicine*, **1997**, 38, 395 – 401.
- 32) Hussain, A. A.; Awad, R.; Crooks, P. A.; Dittert, L. W. Chloramine-T in Radiolabeling Techniques. *Analytical Biochemistry*. **1993**, 214, 495 – 499.
- 33) Hassan, H. E.; El-Azony, K. M.; Azzam, A.; Qaim, S. M. Investigation of Selenium Compounds as Targets for $^{76,77}\text{Br}$ Production Using Protons of Energies up to 34 MeV. *Radiochim. Acta*. **2017**, 105 (10), 841 – 850.

- 34) Ellison, P. A.; Olson, A. P.; Barnhart, T. E.; Hoffman, S. L. V.; Reilly, S. W.; Makvandi, M.; Bartels, J. L.; Murali, D.; DeJesus, O. T.; Lapi, S. E.; Nickles, R. J.; Mach, R. H.; Engle, J. W. Improved Production of ^{76}Br , ^{77}Br , and $^{80\text{m}}\text{Br}$ via CoSe Cyclotron Targets and Vertical Dry Distillation. *Nuc. Med. Biol.* **2020**, *80*, 32 – 36.
- 35) Tolmachev, V.; Lovqvist, A.; Einarsson, L.; Schultz, J.; Lundqvist, H. Production of ^{76}Br by a Low-Energy Cyclotron. *Appl. Rad. Isotopes.* **1998**, *49*, 1537 – 1540.

II. The Development and Evolution of the Isotope Harvesting System

In order to absorb the intense beam power that will also allow access co-produced radionuclides at the Facility for Rare Isotope Beams (FRIB), a water-filled beam dump has been designed to recirculate the water after irradiation with a high-power primary beam and collect the desired radionuclides through a process termed “isotope harvesting.”¹⁻³ This beam dump has been described by Avilov, *et al.* and consists of a rotating cylinder (Figure 2.1) made of Ti64 alloy (grade 5 alloy: 6% Al, 4% V, mass balanced with Ti) with a flowing-water interior.³ The material of the beam dump was chosen as the Ti64 alloy because it is known to be resistant to corrosion and a durable material. The material is also readily available as an additive manufacturing technique material used in 3D printing, which means the beam dump can be tailored to a specific design.

The cylinder of the beam dump target is 70 cm in diameter. A main concern of the design is that the heat produced by the beam entering the target must be effectively dissipated. As the beam enters the target at high energies, this energy is transferred into the target material as kinetic energy. The heat produced by this transfer must be transferred effectively into the water and carried away from the face in order to prevent nucleate boiling. If nucleate boiling conditions occur, the target face would reach extreme temperatures and even lead to melting of the Ti64 material. In order to ensure nucleate boiling cannot occur, the target cylinder will be rotated at a rate of 600 rpm and the water will flow across the face of the beam dump at a rate of 60 gallons per minute. In addition to the high flow rate, the chamber of the target includes a double wall that directs the flow through a narrow space across the front face of the target to increase the flow of water by the beam’s entrance.³

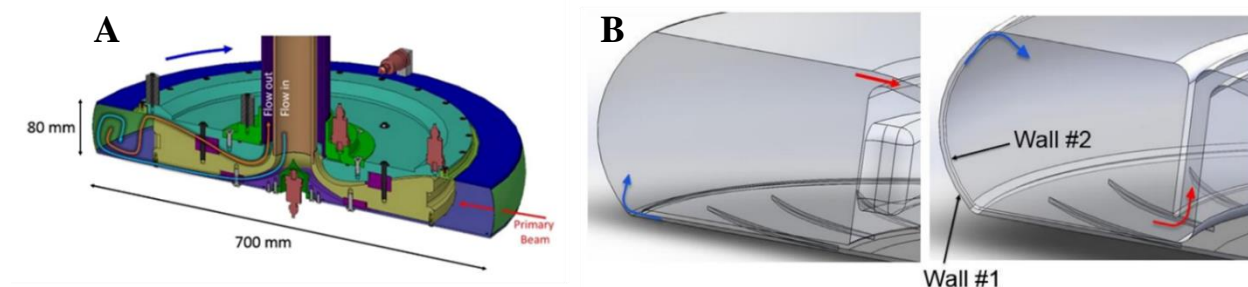


Figure 2.1: A cross-sectional view of the FRIB harvesting beam dump design featuring the double-walled interior chamber. The blue arrow in part a represents the direction of the cylinder rotation and the red arrow represents the incoming beam. The arrows in part b represent the flow of water into (blue) and out of (red) the chamber^a

As the primary beam interacts with the target and water inside of the beam dump, both nuclear interactions and electronic interactions occur. Nuclear interactions between the beam particles and the water are responsible for the production of radionuclides in the water and consist of fragmentation reactions (FR) and fusion-evaporation reactions (FE).^{4,5} FR reactions result when beam particles collide with atoms of the target at high energies and form fragments of the original nucleus. As the beam slows down and reaches lower energies, FE reactions occur. Tools such as LISE++ can be used to predict the activities of desired radionuclides in the water-filled targets resulting from a specific beam at a specific energy.^{6,7} Electronic interactions also occur between the beam particles and the water which leads to radiolysis, or the break-up of water molecules. When water is irradiated, the energy is deposited along particle tracks and results in the formation of free radicals as well as many molecular species including $\cdot\text{OH}$, $\cdot\text{H}$, H^+ , OH^- , H_2 , and H_2O_2 .⁸ The production rates of these species is dependent on the linear energy transfer (LET) of the beam particles. As the irradiation intensity increases, the LET increases and

^a Reprinted from Avilov, M.; Aaron, A.; Amroussia, A.; Bergez, W.; Boehlert, C.; Burgess, T.; Carroll, A.; Colin, C.; Durantel, F.; Ferrante, P.; Fourmeau T.; Graves, V.; Grygiel, C.; Kramer, J.; Mittig, W.; Monnet, I.; Patel, H.; Pellemoine F.; Ronningen R.; Schein, M. Thermal, Mechanical, and Fluid Flow Aspects of the High Power Beam Dump for FRIB. Nuclear Instruments and Methods in Physics Research Section B. Interactions with Materials and Atoms. 2016, 376, 24-27, with permission from Elsevier.

radiolysis tracks form closer together which allows for the recombination of some of these products. However, some species such as H_2 and H_2O_2 do not recombine and are instead distributed throughout the system.⁹ The hydrogen peroxide changes the chemical state of the water and can become damaging to the components of the system. The production of hydrogen gas dissolved in the water can lead to a buildup of pressure and potentially lead to the danger of explosion.

In addition to the target design ensuring resistance to corrosion and prevention of nucleate boiling, an attached water system is necessary to both measure and mitigate the effects of radiolysis products in the target. Included in such a system should be separate aqueous and gaseous chemistry lines that include sensors for analyzing the conditions of the water and headspace during irradiation, flow meters to analyze the flow rate of water and gas through and out of the system, methods of degassing and decomposition of harmful radiolysis products (H_2 and H_2O_2), and techniques for the collection of desired radionuclides.

In order to demonstrate the feasibility of radionuclide recovery from the water-filled beam dump under similar conditions to FRIB irradiations, different versions of smaller-scale targets and water systems have been developed for irradiation using lower intensity beams at the NSCL. A series of experiments have been performed utilizing the different iterations of the isotope harvesting system to observe the resulting conditions. For the purposes of this project, two main irradiation experiments were carried out: one with a low intensity ^{40}Ca beam and a second with a low intensity ^{78}Kr beam.^{10,11} Through these experiments, the proposed target material was tested and gas-phase isotope harvesting capabilities at the NSCL and future possibilities at FRIB were demonstrated. Data was collected to investigate both the nuclear and electronic interactions between the beam particles and the water during low intensity irradiations.

And finally, all of the information learned from each experiment was used to further optimize the system to increase harvesting yields and prepare for the higher beam power of FRIB.

2.1 First Iteration: Low Intensity ^{40}Ca Irradiation

An initial experiment was designed to test the stability and chemical resistance of the chosen titanium alloy (Ti64) under the conditions caused by irradiation. During this irradiation, the state of the water and the evolution of radiolytic gases under these conditions was also studied in order to optimize the water system and harvesting components. A target holder was designed with a Ti64 alloy disk for testing and the target was irradiated by a $^{40}\text{Ca}^{20+}$ beam at an energy of 140 MeV/nucleon.¹⁰

2.1.1 Target Design

The initial target design involved a housing made of high-density polyethylene to hold the target window material as well as form a water chamber behind the target disk (Figure 2.2). High-density polyethylene was chosen as a cheap material that is known to be resistant to hydrogen peroxide. The housing design allowed the flow of water through an inlet in the bottom of the chamber, to flow through the chamber, and exit through an outlet on the top. The internal chamber had a volume of approximately 120 mL. For this experiment, the target was placed in air at the exit of a beam line at the NSCL as depicted in Figure 2.3.

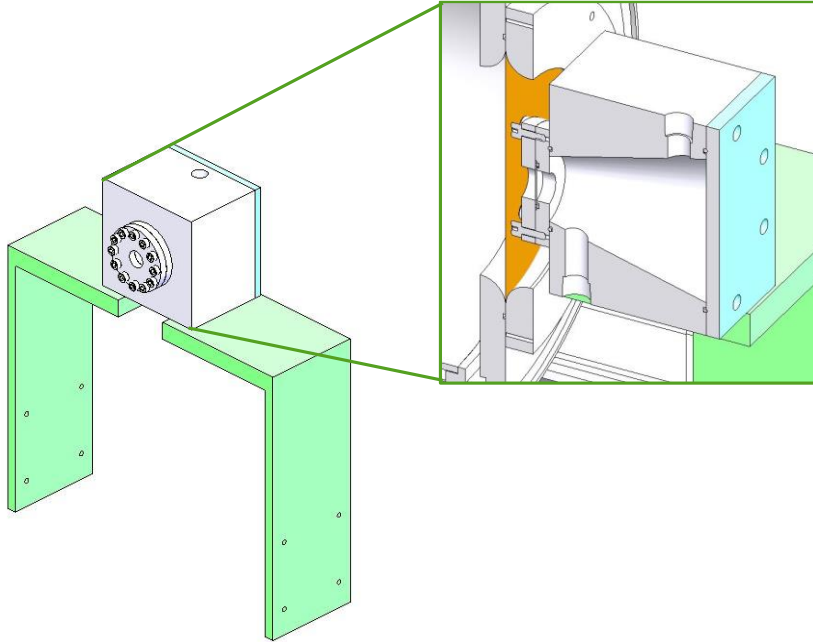


Figure 2.2: A schematic drawing of the target housing, specifically featuring the polyethylene chamber where the water entered the inlet on the bottom near the window and exited the outlet on top. The brackets shown in green simply supported the target chamber.

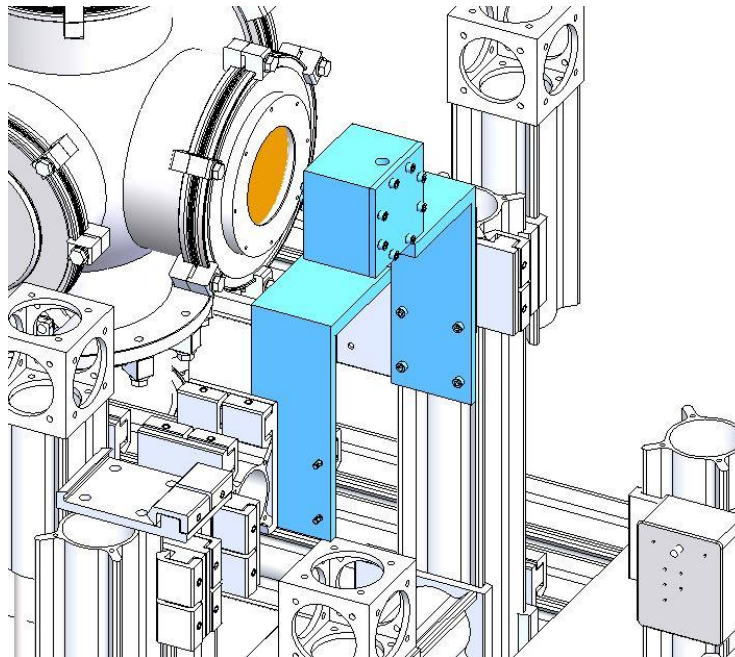


Figure 2.3: A schematic demonstrating the placement of the target at the end of the beam line. The beam exited the beam line vacuum through a thin window shown in orange.

The target window used as the beam's entrance into the water chamber was a disk made of a Ti64 alloy, 0.7 mm thick with a diameter of 15 mm in contact with the water on the downstream side. In order to replicate the manufacturing process of the future beam blocker, the window was fabricated in a 3D printing process by Stratasys. The front surface was divided into two halves – one which was milled smooth and the other which was left with a rough surface from the 3D printing process.



Figure 2.4: Optical image of the irradiated Ti64 disk. In this image, the top half of the disk was left as the rough 3D-printed material and the bottom half was milled smooth.

2.1.2 Water System

The initial water system which was developed consisted of a small water reservoir, pumps, sensors to measure the environment in the water, ion exchange resins to collect aqueous isotopes, membrane contactors to sparge gaseous isotopes from the water, and gas traps. Each component was connected into a system with polypropylene fittings holding high-density polyethylene tubing of ¼” outer diameter and 3/16” inner diameter. Approximately 6 L of ultra-

pure water was pumped from the reservoir to the target and through the water system by an air-operated diaphragm pump (Yamada NDP-5FVT) at a flow rate of 1 L/min.

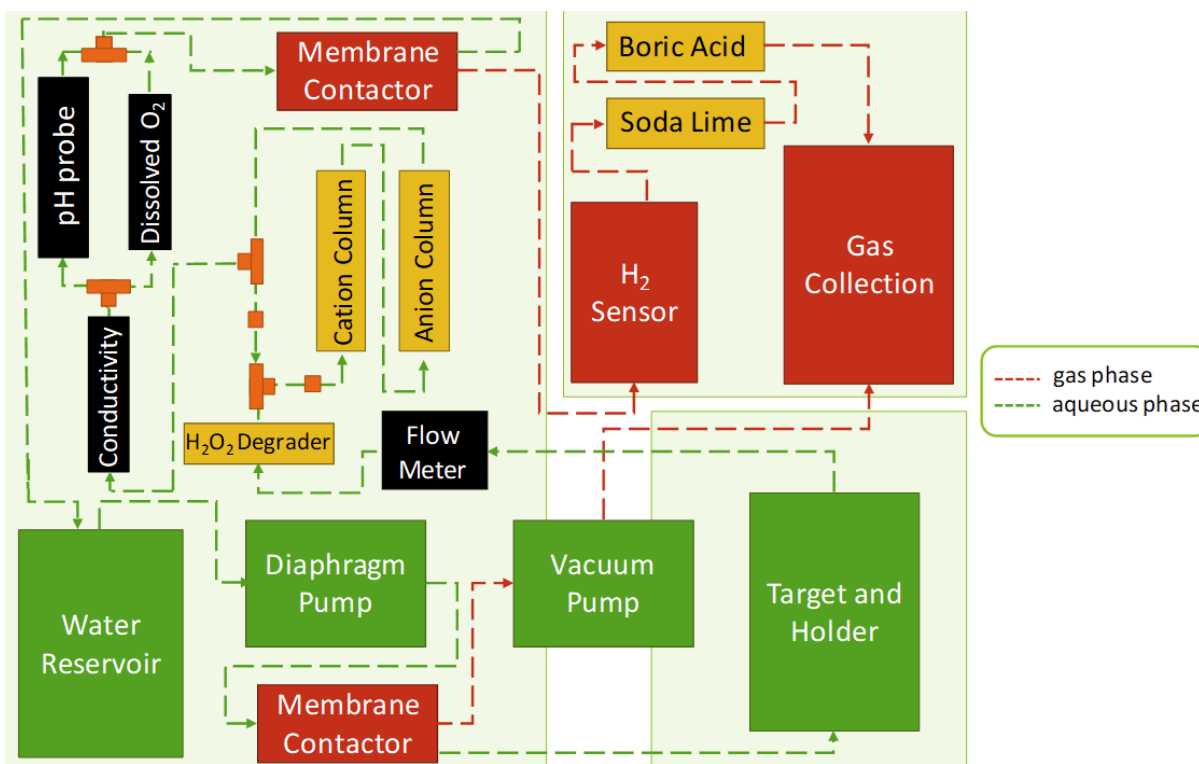


Figure 2.5: A schematic diagram of the order of the components included in the water system. Components in green involved a loop of the water reservoir which led into and out of the target. Components in blue included those that measured the condition of the water. Components in yellow included anything that removed radionuclides from the aqueous and gas phases. Finally, components in red involved those that removed and measured the gases in the system.

In order to measure the amounts of radiolytic species produced in the water, a Honeywell Midas Gas Detector was used to detect radiolytically produced hydrogen gas (MIDAS-E-H2X), a Mettler-Toledo Thornton High Performance Dissolved Oxygen Sensor (InPro6050 polarographic oxygen sensor) detected radiolytically produced oxygen gas, a Mettler-Toledo Thornton pHure Sensor (2003i-UPW/120) detected changes in pH. A Mettler-Toledo Thornton UniCond Conductivity Sensor (1/2" NPTM titanium 0.1 cm⁻¹ sensor, part number 58 031 406) was used to detect any ions (radioactive or not) dissolved in the water. The presence of non-

radioactive ions could potentially indicate corrosion of the titanium window surface due to irradiation. And finally, an Omega Micro-Flo paddle-wheel flow meter (part number FTB323D) was used to continuously measure the flow rate of the water throughout the system. In order to read and record the outputs from the dissolved oxygen sensor, the pH sensor, the conductivity sensor, and the flow meter were connected to a Mettler-Toledo M800 multi-parameter transmitter. The outputs were recorded every 5 seconds. The data from the Midas Gas Detector was manually recorded every 2 minutes.

As an aqueous harvesting proof-of-concept method, cation and anion exchange columns (AG 50W-X8 and AG 1X8; 20-50 mesh size; BioRad) were included in the water system. The columns were made from ¾" outer diameter polyethylene tubing connected with polypropylene compression fittings. After the ⁴⁰Ca irradiation, radionuclides that were collected on each column were assayed.

The system included a column filled with small pieces of platinized titanium mesh used as a catalyst to degrade radiolytically produced hydrogen peroxide. Hydrogen peroxide would be a major corrosive agent if not removed from the system. The degradation of hydrogen peroxide is as follows in Equation 2.1:



where hydrogen peroxide is broken down into water and molecular oxygen as a dissolved gas.

Two 3M Liqui-Cel membrane contactors (2.5 x 8 EXF, Membrane X40) were used to sparge dissolved gas from the water. These membrane contactors were made out of hydrophobic hollow-fiber microporous membranes which allow removal of dissolved gases from the water through mass transfer. The driving force behind this mass transfer that follows Henry's law which states that the likelihood of a gas to dissolve in water is proportional to its partial pressure

in the gas phase as in Equation 1.1. If the partial pressure of the gas in contact with the water is reduced, the gas will be sparged. The first membrane contactor was used to degas the water before it entered the target chamber. In order to do this, the membrane contactor was connected to a Marathon electric vacuum pump (M100GX, 1/6 HP) on the lumen side. Degassing the water prior to its entrance into the target chamber reduced air bubbles in the target which maximized heat transfer between the front titanium window and the water. The second membrane contactor was used to sparge the radiolytically produced gaseous species as well as gaseous isotopes produced through beam interactions with the water in the target chamber. In order to sparge these gases, the membrane contactor was connected to the Midas hydrogen sensor on the lumen side. Air from the laboratory environment was pulled through at a flow rate of 500 mL/min in accordance with the operating procedure of the sensor, which also meant the water system was not a closed system and allowed for the re-equilibration of the water with atmospheric pressure air.

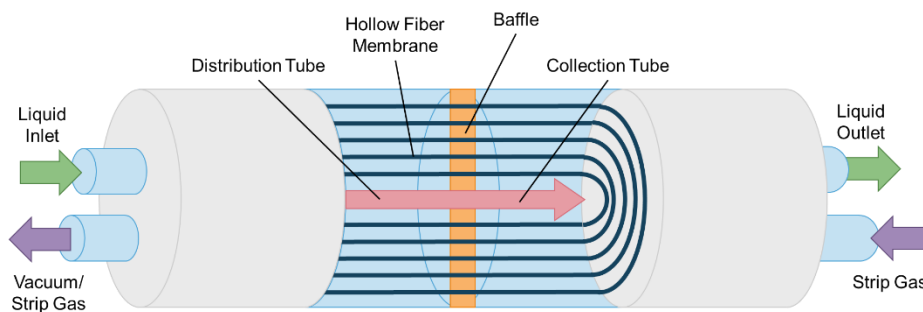


Figure 2.6 Flow patterns in the membrane contactor.

The final components of the system included gas traps used to remove unwanted gases and separate gaseous isotopes of interest. The traps used in the first iteration of the water system included soda lime (Sigma Aldrich granular, ACS reagent, +100 mesh) and boric acid (Fisher Chemical, crystalline, certified ACS). Both traps were made from 14 cm long polypropylene

tubing ($\frac{3}{4}$ " outer diameter) with glass wool packing on both ends to contain the chemicals as shown in Figure 2.7.

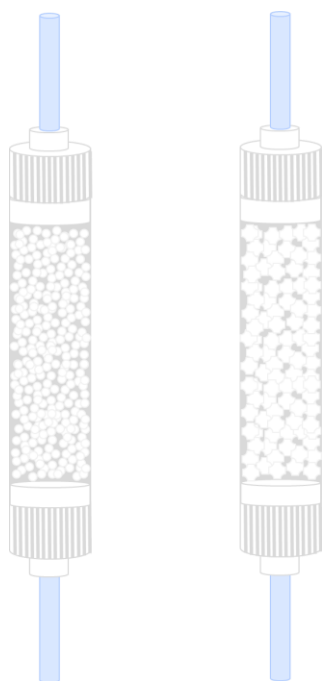
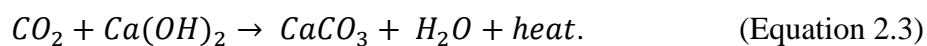
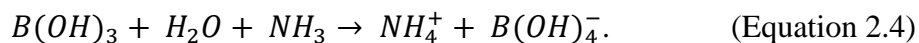


Figure 2.7: A schematic representation of the boric acid (left) and soda lime (right) traps used in the experiment. The traps were made using polypropylene tubing and compression fittings and were filled with the chemicals as well as glass wool.

Soda lime, which mostly consists of calcium hydroxide, water, and sodium hydroxide, is a highly efficient carbon dioxide absorber. For the purposes of this system, soda lime would effectively remove ^{11}C in the form of $[^{11}\text{C}]\text{O}_2$ through the following mechanism shown by Equation 2.3:¹²



Boric acid crystals are known to capture ammonia and would effectively remove ^{13}N from the air in the system through the mechanism shown in Equation 2.4:¹³



The components were connected in the system to optimize the data collected from each sensor and to ensure that an accurate representation of the condition of the water was attainable. For example, as previously discussed, the membrane contactors were placed in specific areas to serve the sparging gas from the system in two areas. The first was placed before the target to remove unwanted air bubbles present from the re-equilibration with the atmosphere at the second membrane contactor as well as in the headspace of the water reservoir. The second membrane contactor was placed after all other components in the system to remove gases to be sent through the gas line. The catalyst used to degrade hydrogen peroxide was placed after the target as that was the area with the highest concentration of H_2O_2 and before the rest of the components that would be negatively affected by the potential corrosion the peroxide would cause. Figure 2.8 shows images of the entire water system set-up as well as the target at the end of the beam line.

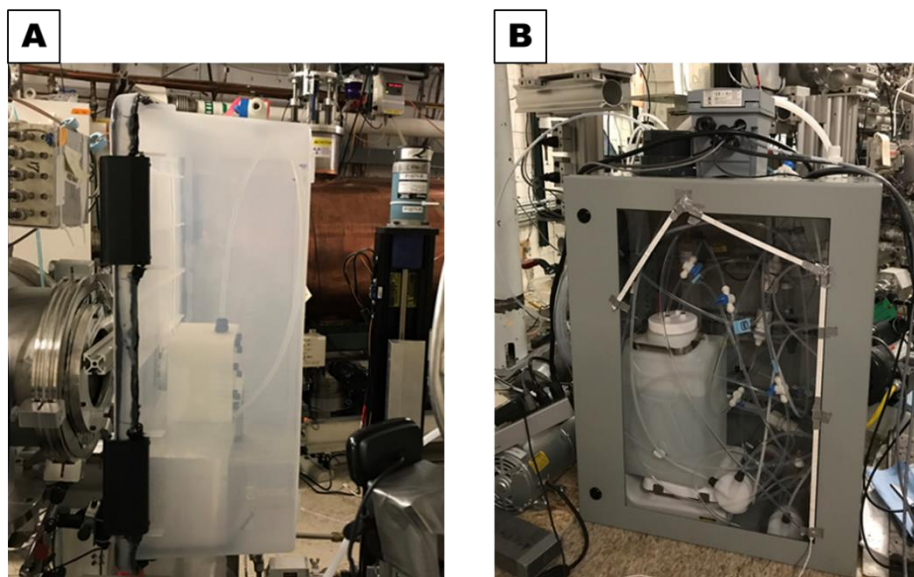


Figure 2.8: Images taken before the irradiation experiment of the target within secondary containment at the end of the beam line (a) and the water reservoir with components in additional secondary containment (b).

2.1.3 First Iteration of Water System Conclusions

The first iteration of the target design was used solely to test the proposed material to be used in the development of the future NSCL targets as well as the FRIB beam dump. During the ^{40}Ca irradiation, a leak developed between the target water chamber and the back plate of the target housing due to the periodic pressure from the diaphragm pump used to flow water through the target chamber. This target design was not used in any future experiments, but was still successful in allowing for the study of the stability of the target window during irradiation as well as its resistance to corrosion under irradiation conditions. Following the irradiation, scanning-electron microscopy (SEM) and energy-dispersive x-ray spectroscopy (EDS) was performed on the irradiated disk sample to observe any differences pre- and post-irradiation. Results from these studies are described in detail in Chapter 3.

The first iteration of the water system demonstrated several potential areas of improvement for future experiments. The first area of interest were the membrane contactors used in the system which were partially decomposed after contact with hydrogen peroxide. Therefore, water was able to cross between the lumen and shell sides of the membrane contactors and water was found in the gas line. In order to resolve this issue, in future iterations of the water system, other methods of degassing had to be used. Additionally, the platinized titanium mesh proved insufficient for the decomposition of hydrogen peroxide in the system and an alternative method needed to be explored. A second area of interest involved two of the sensors used in the system – the pH sensor and the hydrogen gas detector. Elemental analysis of the water demonstrated high levels of potassium ions which originated from the electrolyte solution in the pH probe and interfered with the other ion measurements. In order to measure the hydrogen gas in the system, one side of the membrane contactor attached to the hydrogen sensor was open to

air which meant the water system was not a closed system. This led to the re-equilibration of the previously degassed water with atmospheric O₂ and CO₂, which interfered with the dissolved O₂ probe measurements, the conductivity probe measurements, and the pH level. In future iterations of the water system, no sensors should be used that require atmospheric air or have any other components that effect the chemistry of the system.

2.2 Second Iteration of Water System: ⁷⁸Kr Irradiation

A second irradiation experiment was performed using a target design that more closely resembled the future water-filled beam dump at FRIB. The target was once again made with the Ti64 alloy, as that material demonstrated the desired properties needed for irradiation and isotope collection. The stable beam selected for this experiment was ⁷⁸Kr at an energy of 150 MeV/nucleon. The main purpose of this experiment was to test the gas-phase harvesting capabilities of the harvesting system and to work on the optimization of the gas collection line while also collecting more information about the conditions of the system and production of radiolytic species. In order to test the gas-phase harvesting potential, an improved gas collection line was used to collect isotopes of krypton online to generate desired bromine isotopes (⁷⁶Br and ⁷⁷Br) offline that could be useful in other applications.

2.2.1 Target Design

The second iteration of the flowing-water target was designed to be similar to what will be used for the FRIB beam dump. After testing the Ti64 alloy material during a ⁴⁰Ca irradiation, the new target was designed with the same material using the same 3D printing manufacturing process from Stasys described in Section 2.1.1. The dimensions of the target body were 125 x 51 x 51 mm³ as shown in Figure 2.9. The outer body dimensions were designed to be similar to

the solid blocker typically used in that location. Internally, the target was designed with a water chamber and incorporated channels for water flow into and out of the chamber. The front face of the target (beam entrance side) was designed to be only 590 μm thick with a second 590 μm thick wall reaching approximately $\frac{3}{4}$ of the height of the chamber behind it to form a 2 mm thick water channel in between. The front face was designed in such a way to maximize cooling: water flows vertically from the inlet channel, quickly across the front face of the target and over the second thin wall and into the water chamber where it fills up before traveling out the outlet channel. The interior water chamber can hold about 86 mL of water. By maximizing the water flow rate across the front face of the target (irradiated surface), this design ensures that the temperature at the interface between Ti64 and water is low enough to prevent nucleate boiling from occurring. The large volume of water downstream from the thin channel was to completely stop various primary beams.

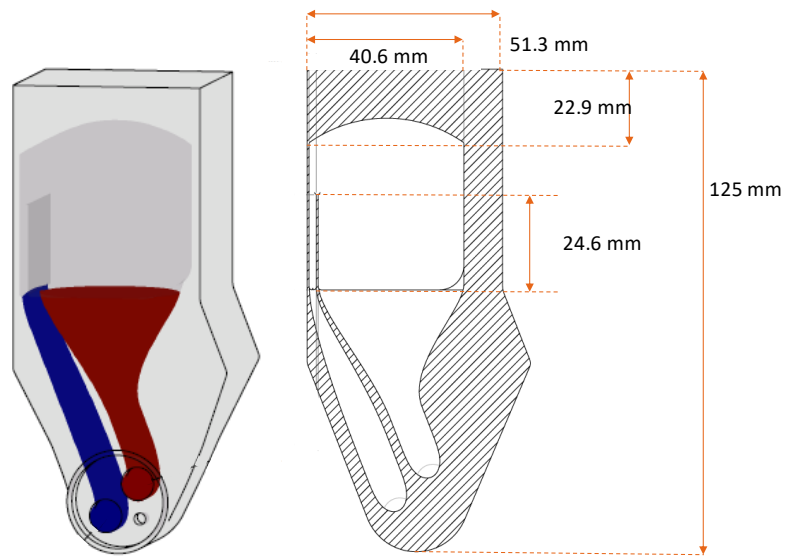


Figure 2.9: A schematic drawing including measurements of the 3D-printed Ti64 target. In this drawing, water enters the target through the blue inlet tube, flows across the front face, and exits the target through the red outlet tube. The entire inner volume is filled with water. The beam enters the target from the left side.

In order to visualize the inside of the beam blocker and ensure it was 3D printed properly, the target was imaged using a micro CT scanner (Perkin Elmer, Quantum GX μ CT). The results of the CT scan can be seen in Figure 2.10, where a uniform wall thickness of 540 – 590 μ m was observed for both the outer front face and the inner chamber wall. The scan confirmed that this 3D printed target was suitable for irradiation.

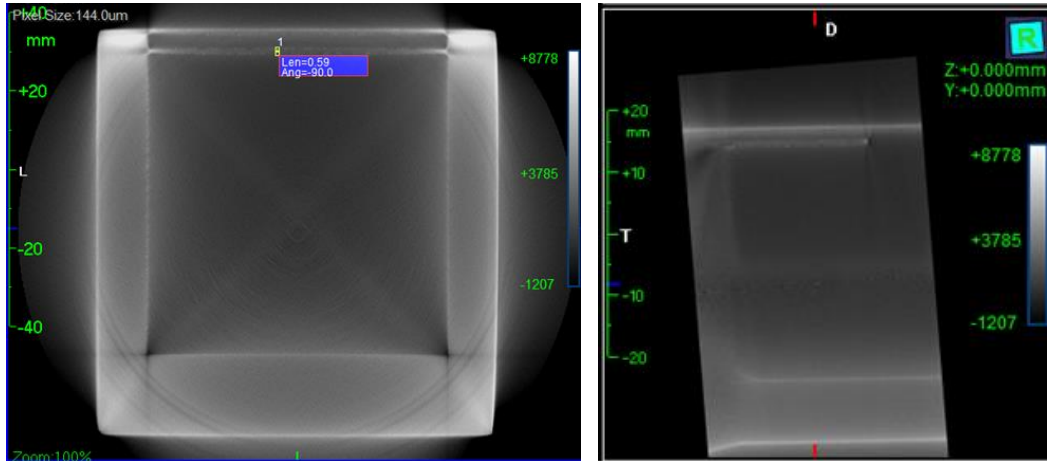


Figure 2.10: CT scan results of one of the 3D-printed Ti64 targets. These images show that the 3D printing process was successful at producing the thin-walled target with double-walled interior chamber at the front face.

The water-filled target was also placed at the end station of the beam line during the ^{78}Kr irradiation in a similar location to that depicted in Figure 2.3, however it was placed inside the beam line vacuum. An image of the target inside the beam vacuum chamber is shown in Figure 2.11.



Figure 2.11: Image of the titanium blocker positioned in the beam line end station for irradiation. The beam enters normal to the front face.

2.2.2 Water System

While the overall design and general purpose of the second iteration of the water system was similar to the first iteration, there were also many differences and improvements. The system still included a water reservoir, pumps, sensors to measure the chemical environment in the water, ion exchange resins to collect aqueous isotopes, and gas traps. However, the new system was much larger than the first iteration. The water reservoir (McMaster Carr, portable stainless steel dispensing tank) held approximately 36 L of water which was pumped at varying flow rates through several feet of tubing. The water was pumped through the system using a centrifugal pump (Grundfos CRNE 3-6) in constant pressure mode. An important difference was that instead of having the water flow in one large loop, in the new system, the water was directed through several loops with varying flow rates to attain specific purposes. Each specialized loop contained precision flow valves (Ham-let, 316 stainless steel) that could be used to adjust the flow rate to

each loop from the main target loop. These specialized loops are denoted by different colors in Figure 2.12.

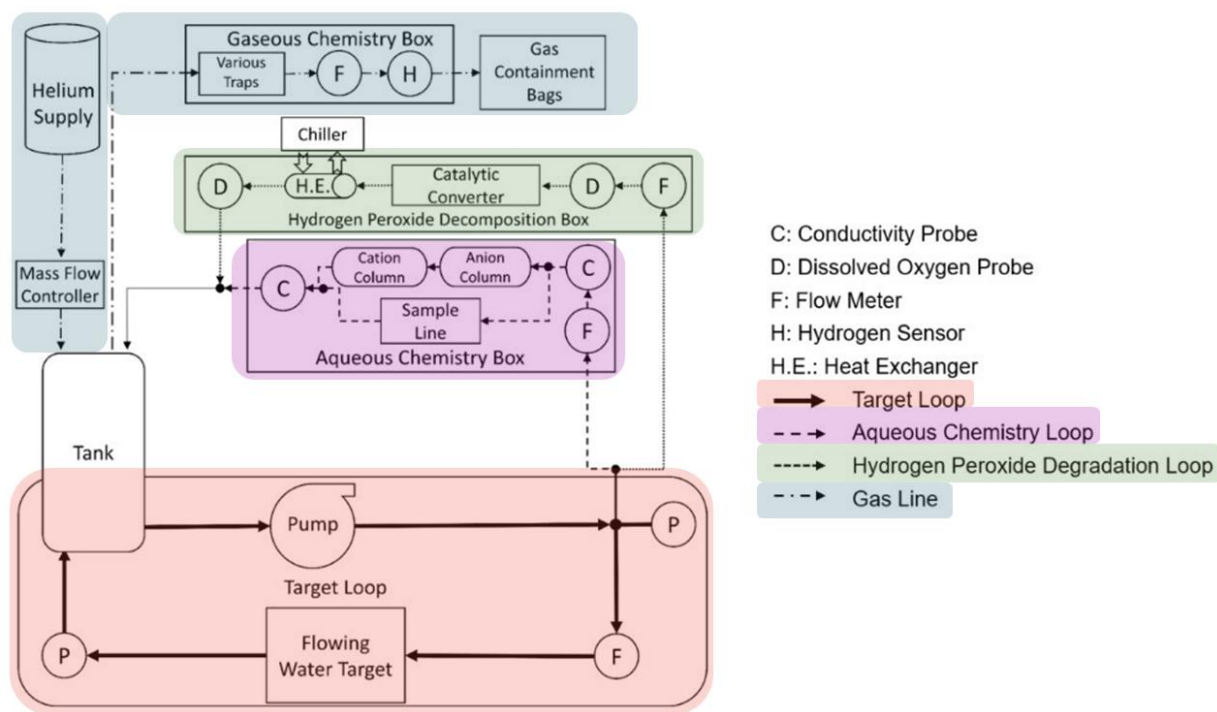


Figure 2.12: A schematic representation of the second iteration of the water system and the order of water and gas flow through the components in the system. This system consisted of four independent loops: 1) the target loop (red), 2) the aqueous chemistry loop (purple), 3) the hydrogen peroxide degradation loop (green), and 4) the gas line (blue).

The main target loop (highlighted in red in Figure 2.12) included the new water reservoir, the new pump, and the new water-flowing target. The components of this loop were connected using nylon-reinforced polypropylene tubing (ID 19 mm). The water flowed through this loop at 10 L/min using the centrifugal pump at 25 psig. The flow rate was measured using a flowmeter (McMaster Carr, Flowmeter for chemicals, 3/4" NPT female, 2 to 20 gpm) and controlled by changing the pressure of the pump if necessary.

One of the specialized loops consisted of a hydrogen peroxide decomposition box (highlighted in green in Figure 2.12). The water flowed through this loop at a rate of 300 mL/min

through ¼” polypropylene tubing. Instead of using platinized titanium mesh for the degradation of hydrogen peroxide, a catalytic converter (Yonaka 2.5” ID Ultra High Flow Metal Core Race Universal Cat Catalytic Converter) was used. Using this unit, hydrogen peroxide was decomposed through the use of palladium and platinum coated on the surface of a metallic honeycomb support. In order to remove the heat deposited in the water from the catalytic converter, a heat exchanger (Brent Industries Titanium Pool Heat Exchanger SP-55Kti-S) and chiller (Thermo Scientific, Thermoflex 1400 W) were also included in this loop to keep the temperature of the water around 25°C.

The final two loops included an aqueous chemistry section (highlighted in purple in Figure 2.12) and a gaseous chemistry section (highlighted in blue in figure 2.12), which were used to harvest desired radioactive products from the water system during irradiation. The components of both loops were connected to the system using ¼” polypropylene tubing. The purpose of the aqueous chemistry loop was to remove any ionic species from the water in the system, including stable and radioactive products. This was accomplished by flowing the water at a rate of 300 mL/min across both cation and anion exchange resins.

The gaseous chemistry line (shown in detail in Figure 2.13) included many of the same components as the first iteration; however, in this design, the purpose of the gas line was to collect and separate a specific gaseous isotope. Therefore; many additional components were included. Instead of using membrane contactors to sparge the dissolved gases from the water, the dissolved gases were sparged using a stream of helium purge gas at a flow rate of 135 mL/min from the bottom of the reservoir to the headspace in the top. The purge gas then carried the gaseous species through to the gas line section which consisted of a series of gas traps used to

purify the gas stream and remove water vapor from the gas mixture to optimize the collection of desired gaseous isotopes.

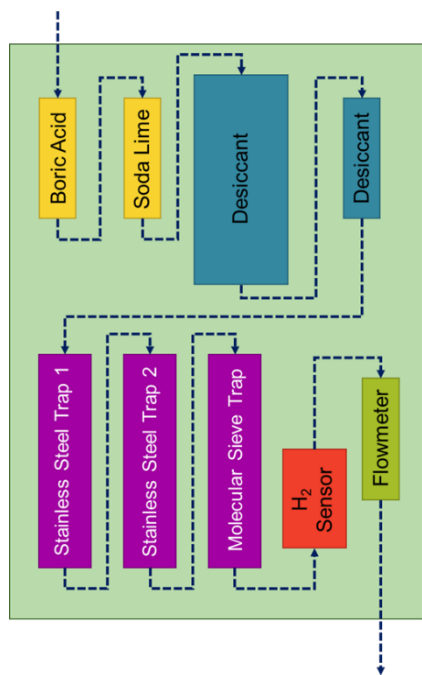


Figure 2.13: A detailed schematic of the order of the components used in the gas line portion of the second iteration of the water system.

The boric acid and soda lime traps were used once again in order to remove $[^{13}\text{N}]\text{NH}_3$ and $[^{11}\text{C}]\text{CO}_2$, respectively. They were assembled in the same manner as described in Section 2.1.2. Following the first two traps to remove unwanted gases, a large trap filled with desiccant was used to remove water vapor and any condensation in the gas stream. The final trapping section consisted of three cold traps to collect the desired gaseous isotopes. The first two cold traps were made with a fritted stainless steel filter featuring a large, porous surface (Swagelok, SS-6F-60, 316 stainless steel, 60 micron pore size) and stainless steel tubing (316 stainless steel, ¼" OD, McMaster-Carr). The third cold trap was a glass gas washing bottle filled with molecular sieves (Sigma Aldrich, pellets, 4 Å). In order to make cold traps, each gas trap was placed in a Dewar filled with liquid nitrogen during the irradiation (Figure 2.14).

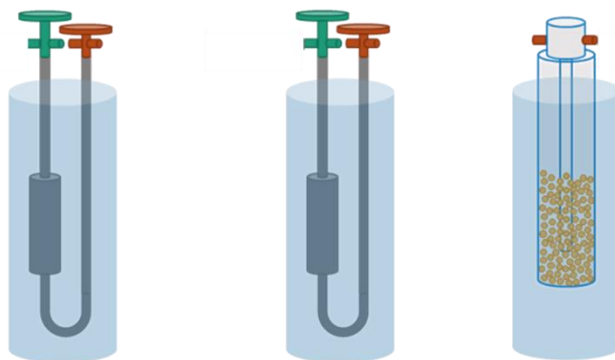


Figure 2.14: A schematic representation of the cold traps used in the online collection – the two stainless steel cold traps on the left and in the middle and the glass collection vessel filled with molecular sieves on the right.

Similar to the first iteration, a series of sensors was used to observe the condition of the water in the system, especially before and after each specialized loop. Three different flowmeters were used to monitor the flow in: (1) the target loop (McMaster Carr, Flowmeter for chemicals, $\frac{3}{4}$ " NPT female, 2 to 20 gmp), (2) the hydrogen peroxide decomposition loop (Brooks Instrument, 1250-55, and (3) the aqueous chemistry loop (Brooks Instrument Sho-Rate Model 1250A). Conductivity sensors (Mettler Toledo, UniCond Conductivity sensor) were placed before and after the ion exchange resins in the aqueous chemistry box to measure to conductivity in the system as well as test the efficiency of the columns. Dissolved oxygen probes (Mettler Toledo, polarographic dissolved oxygen sensor) were placed before and after the hydrogen peroxide decomposition loop to record the amount of oxygen being produced through the decomposition reaction, which could be used to predict the amount of hydrogen peroxide in the system. On the gas chemistry line, a hydrogen sensor (H2Scan, HY-OPTIMA 710B) measured the amount of molecular hydrogen which was radiolytically produced. In the second iteration of the water system, there was no pH probe to ensure there would be no outside influences on the conductivity in the system. The system was also a completely closed system so that no re-

equilibration with atmospheric air was possible. Each component in the system was controlled and recorded with a Programmable Logic Controller (PLC) unit (Automation Direct Productivity 2000 – Productivity Suite v3.0.17, Automation Direct).

2.2.3 Second Iteration of the Water System Conclusions

The second iteration of the target design more closely resembled the FRIB beam dump design and proved successful in withstanding ^{78}Kr irradiation for an 11-hour period. The target was developed using the same material as the first iteration design and again showed no concerning signs of corrosion at low beam intensity. CT scan results of the interior of the target chamber showed that the 3D printing process was a reliable technique for the development of these targets, and several identical targets were 3D printed for use in future experiments.

The second iteration of the water system consisted of many different components compared to the first iteration. The amount of water flowing through the system increased from approximately 6 L to 36 L and the flow rate changed from a constant rate of 1 L/min in the entire system to varied rates depending on the location in the system (300 mL/min to 10 L/min). More sensors were used throughout the system to collect more data – each aqueous phase loop consisted of its own flow meters and dissolved oxygen and conductivity probes were located before and after specific components to measure the changes. A new hydrogen sensor was used that did not require atmospheric gases for measurement in order to ensure a closed system and no re-equilibration of O_2 and CO_2 in the system. An improved method for the degradation of hydrogen peroxide was utilized and the concentration of peroxide in the system was indirectly measured. Finally, the gas line consisted of more traps which were specific in purpose – the removal of unwanted gases, the removal of unwanted water vapor, and cold traps for the collection of desired gases. The updates to the water system allowed for the observation of more

aspects of the system and a better understanding of the conditions due to irradiation. The detailed results of this irradiation are described in Chapter 4. The main issue to arise with this system was the amount of H₂ production as the beam intensity was increased. In the current system, there is no method of hydrogen and oxygen gas recombination, and in order to decrease the percentages of each gas to be well-within the limit at which explosive recombination was possible, the flow rate of gas must be increased to a rate unsuitable for total gas collection and retention. A potential method to resolve this danger is described in detail in Chapter 5.

2.3 Overall Conclusions

In order to prepare for irradiations experiments at FRIB utilizing the proposed design for isotope harvesting, a smaller scale water-filled target and water harvesting system was developed and tested under irradiation conditions. Multiple experiments have been performed to observe the water and gas chemistry during and after irradiation, test the stability and durability of the target material, and prove that desirable radionuclides can be harvested from both the aqueous and gas phases. These experiments have allowed further optimization of the water system based on the new data that was collected during this experiment. New methods were then used in a second system to increase the effectiveness of hydrogen peroxide decomposition, decrease the amount of hydrogen gas in the system to ensure safety, increase the efficiency of radionuclide collection in both the aqueous and gaseous phases, and increase the quality of the sensor components used in the system for the most accurate data collection.

The two iterations of the target and water system were used in separate experiments where the detailed results are described in detail in Chapters 3 and 4, respectively. The data collected and information obtained from these irradiations allowed for two subsequent full-power irradiations of the second iteration of the water-filled target. In these irradiations, a beam

of 0.5 kW power with 80 pnA 140 Mev/nucleon ^{48}Ca at the NSCL used the second iteration of the water system as well as a fourth iteration described by Abel, *et al.* The results described here provided the necessary information to safely increase the beam power in future experiments and has also led to the development of a system that can be used for isotope harvesting under the conditions supplied by FRIB.

REFERENCES

REFERENCES

- 1) Gade, A.; Sherrill, B. M. NSCL and FRIB at Michigan State University: Nuclear Science at the Limits of Stability. *Phys. Scr.* **2016**, *91* (5), 053003
- 2) Abel, E. P.; Avilov, M.; Ayres, V.; Birnbaum, E.; Bollen, G.; Bonito, G.; Bredeweg, T.; Clause, H.; Couture, A.; DeVore, J.; Dietrich, M.; Ellison, P.; Engle, J.; Ferrieri, R.; Fitzsimmons, J.; Friedman, M.; Georgobiani, D.; Graves, S.; Greene, J.; Lapi, S.; Loveless, C. S.; Mastren, T.; Martinez-Gomez, C.; McGuinness, S.; Mittig, W.; Morrissey, D.; Peaslee, G.; Pellemoine, F.; Robertson, J. D.; Scielzo, N.; Scott, M.; Severin, G.; Shaughnessy, D.; Shusterman, J.; Singh, J.; Stoyer, M.; Sutherlin, L.; Visser, A.; Wilkinson, J. Isotope Harvesting at FRIB: Additional Opportunities for Scientific Discovery. *J. Phys. G Nucl. Part. Phys.* **2019**, *46* (10), 100501
- 3) Avilov, M.; Aaron, A.; Amroussia, A.; Bergez, W.; Boehlert, C.; Burgess, T.; Carroll, A.; Colin, C.; Durantel, F.; Ferrante, P.; Fourmeau T.; Graves, V.; Grygiel, C.; Kramer, J.; Mittig, W.; Monnet, I.; Patel, H.; Pellemoine F.; Ronningen R.; Schein, M. Thermal, Mechanical, and Fluid Flow Aspects of the High Power Beam Dump for FRIB. *Nuclear Instruments and Methods in Physics Research Section B. Interactions with Materials and Atoms.* 2016, *376*, 24-27.
- 4) Campi, X.; Hüfner. Nuclear Spallation-Fragmentation Reactions Induced by High-Energy Projectiles. *Physical Review C.* **1981**, *24* (5), 2199-2209.
- 5) Gavron, A. Statistical Model Calculations in Heavy Ion Reactions. *Physical Review C.* **1979**, *21* (1), 230-236.
- 6) Tarasov, O. B.; Bazin, D. Development of the program LISE: application to fusion-evaporation. *Nuclear Instruments and Methods in Physics Research Section B.* **2003**, *204*, 174-178.
- 7) Tarasov, O.B.; Bazin, D. LISE++: Radioactive Beam Production with In-Flight Separators. *Nuclear Instruments and Methods in Physics Research Section B.* **2008**, *266*, 4657-4664.
- 8) LaVerne, J. A. Detection of gaseous products in the radiolysis of aqueous solutions. *Journal of Physical Chemistry.* **1988**, *92*, 2808-2809.
- 9) LaVerne, J.A. Chapter 14: Radiation Chemical Effects of Heavy Ions In: Charged Particle and Photon Interactions with Matter: Chemical, Physiochemical, and Biological Consequences with Applications, **2003**, 403-430.

- 10) Abel, E. P.; Clause, H. K.; Severin, G. W. Radiolysis and radionuclide production in a flowing-water target during fast $^{40}\text{Ca}^{20+}$ irradiation. *Applied Radiation and Isotopes*, **2020**, *158*, 109049.
- 11) Domnanich, K. A.; Vyas, C. K.; Abel, E. P.; Kalman, C.; Walker, W.; Severin, G. W. Harvesting ^{62}Zn from an aqueous cocktail at the NSCL. *New Journal of Chemistry*, **2020**, *47*, 20861-20870
- 12) Freeman, B. S.; Chapter 17: Absorption of Carbon Dioxide. In *Anesthesiology Core Review*; McGraw-Hill Global Edu Holdings, LLC.: USA 2014
- 13) Cruz, G. Boric Acid in Kjeldahl Analysis. *J. Chem. Educ.* **2013**, *90* (12), 1645 – 1648.

III. The Analysis of the Ti64 Target Material and Rate of Radiolysis Production during a ^{40}Ca Irradiation^b

3.1 Introduction

There have been previous experiments at the National Superconducting Cyclotron Laboratory (NSCL) that utilized a beam blocker involving a water-filled target in order to harvest isotopes.¹⁻⁴ In these experiments, a secondary radioactive beam with intensities on the order of particle picoAmperes (ppA) was used for the collection and extraction of specific radionuclides from the water. The target consisted of a chamber made of polytetrafluoroethylene (PTFE) which held 100 mL of static water. These experiments demonstrated the ability to harvest radionuclides from water and use them in other applications. Following these experiments, a novel flowing-water target and water system was developed to more closely resemble the harvesting infrastructure at the Facility for Rare Isotope Beams (FRIB).^{5,6} In order to test the proposed design and material for the novel target and water system at FRIB, a version of the target which consisted of a polyethylene chamber and beam window made of the selected Ti64 (grade 5 alloy: 6% Al, 4% V, mass balanced with Ti) alloy was developed to be irradiated with a low intensity beam at the NSCL. A water system was connected to this target to observe the conditions of the irradiated water and better understand the nuclear and electronic interactions occurring between the beam particles and water.

The production of radionuclides of interest in the water of the target system itself is possible because nuclear reactions will occur due to interactions between the beam particles and

^b The material presented in this chapter draws heavily from the published paper E. Paige Abel, Hannah Clause, and Greg Severin, Radiolysis and radionuclide production in a flowing-water target during a fast $^{40}\text{Ca}^{20+}$ irradiation, *Appl. Radiat. Isotopes*. **2020**, 158, 109049.

the entrance window and water molecules.⁷ In some cases, the radionuclides have low solubility in water according to Henry's law and can be easily sparged from the aqueous phase and into the headspace of the water reservoir.⁸ This experiment was designed to remove gaseous isotopes from the headspace for both collection and analysis. The ability to collect gaseous isotopes using gas traps was tested and the resulting data was used to design future gas collection experiments.

In addition to nuclear reactions, electronic interactions also occur as the beam particles pass through the target materials and water. A process referred to as radiolysis occurs and results in the formation of free radicals, ions, and other molecular species including OH, ·H, H⁺, OH⁻, H₂, and H₂O₂.⁹ These species are formed along radiolysis tracks and, over time, many of them undergo recombination to reform into water molecules. However, some stable chemical species, such as H₂ gas and H₂O₂ are also produced.⁹ These species have the potential to create a corrosive environment within the target and water system; therefore, the system must be designed to withstand these conditions.

An experiment was performed to test the overall stability and chemical resistance of the target material and water system to the radiolysis conditions. The activity collected on the gas traps in the water system was measured to understand the sparging efficiency as well as the ability to collect gases in the system. Hydrogen gas was also sparged from the system and measured to indicate the rate of production of this radiolysis product and compare the experimental value to a predicted value according to the literature. The surface of the titanium window was analyzed using a series of imaging, microscopy, and spectroscopy methods to determine the effects on the target material from the beam. This experiment provided the information necessary to scale-up future experiments at the NSCL with the purpose of harvesting isotopes and eventually prepare for experiments at the irradiation levels that FRIB offers.

3.2 Materials and Methods

3.2.1 $^{40}\text{Ca}^{+20}$ Irradiation

The first iteration of the target (Section 2.1.1) was irradiated at the NSCL facility with up to ~ 0.4 pA of 140 MeV/nucleon $^{40}\text{Ca}^{+20}$ beam. The current intensity ranged from 0.11(1) pA to 0.42(4) pA during the 3.5 h irradiation. The beam current was recorded using an unsuppressed target, that is some electrons could escape from the target and produce a false positive current, and the values were calibrated against a Faraday cup which was inserted to intercept the beam periodically throughout the irradiation. The regularly recorded values from the unsuppressed target were corrected using a linear relationship that was determined between the accurate values measured with the Faraday cup and the relative measurements from the target.

Due to the secondary containment surrounding the target (implemented to comply with the safety standards at the NSCL), the beam travelled through several layers of varying materials before entering the water chamber. These layers (shown in Figure 3.1) included 75 μm of a thin zirconium foil (Goodfellow) which acted as an end cap for the beam line vacuum, a 5 cm gap of air, 12.5 μm of another thin zirconium foil (Goodfellow), a 2.5 cm gap of air, the 700 μm target window made of grade-5 titanium alloy (Ti64, 6% aluminum and 4% vanadium by mass, balance titanium), and finally the water chamber. Calculations of the stopping power through the target were performed using the stopping and range of ions in matter (SRIM) software and the results are also shown in Figure 3.1.¹⁰ Parameters such as the beam ion, the energy of that ion, and the target material are inputs into the calculation and outputs include the depth of penetration and the change in energy of the ion as it passes through the materials. Based upon the SRIM calculations, the ^{40}Ca beam entered the water with an energy of 5.0 GeV and travelled 11.6 mm into the water.

The target housing was made of high-density polyethylene as described in Section 2.1.1 and held the titanium alloy disk in place. An approximately 15 cm diameter circle of the titanium disk was exposed to the water in the chamber. And as discussed in Section 2.1.1, the disk was divided into two halves – one half milled smooth and the other surface rough from the 3D printing process. For the purposes of this experiment, the beam only interacted with the rough side of the disk.

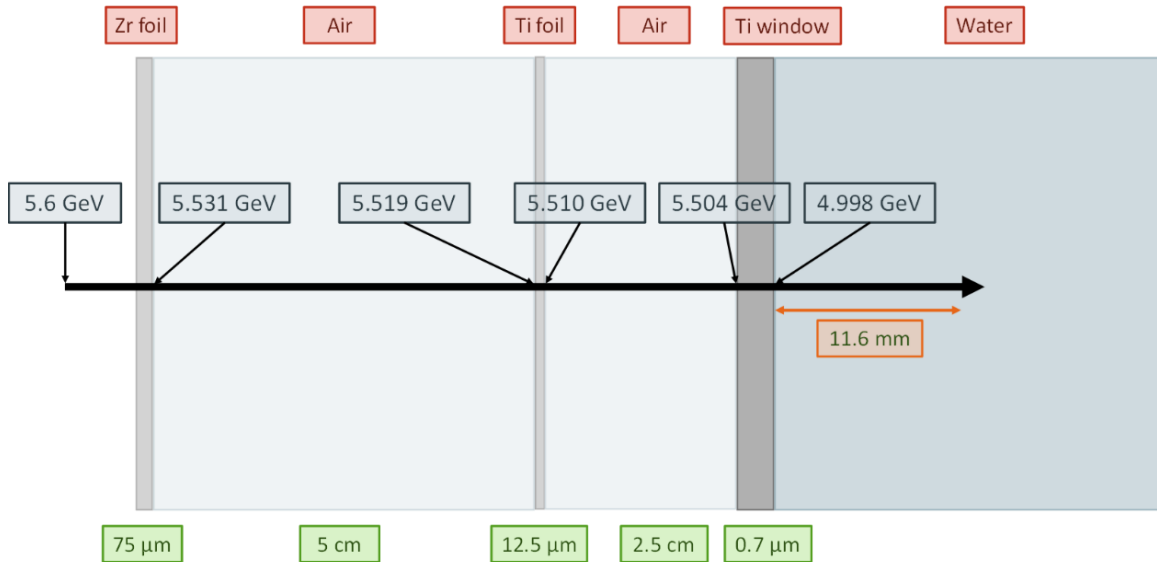


Figure 3.1: Depiction of the changes in beam energy as it traveled through the different material layers included in the target design. The ^{40}Ca beam is represented by the black arrow as it passed through six layers of varying materials and distances. The beam energy decreased from 5.6 GeV as it entered the first layer to 5.5 GeV before it entered the Ti window, and ended at 5.0 GeV GeV as it entered the water and traveled 11.6 mm into the water chamber.

During this irradiation, the first iteration of the water system (Section 2.1.2) was connected to the target window. The water system consisted of the components described in the previous chapter and depicted in Figure 2.5. Approximately 6 L of water was continuously pumped through the target and through the water system for the duration of the experiment. Data from the pH probe, dissolved oxygen probe, conductivity probe, and temperature probe (included

in the conductivity probe) were recorded using a Mettler-Toledo M800 multi-parameter transmitter.

3.2.2 Gaseous Isotope Collection

Part of the water system included a gas line which contained two gas traps for the potential collection of CO₂ and NH₃, consisting of soda lime and boric acid, respectively.

Following the end of irradiation, gamma spectroscopy measurements were taken using a Canberra BEGe Gamma-ray Detector (BE2020) to detect the presence and activity of isotopes located on the gas traps. This spectroscopic technique allows the quantitative determination of radioactive material in a sample by detecting characteristic gamma rays that are produced by the radioactive sources in that sample. The gamma rays have various energies and intensities, which are characteristic of each isotope.

Measurements of the boric acid trap revealed no detectable levels of radioactivity; however, spectra of the soda lime trap resulted in the presence of a 511 keV peak due to positron annihilation. Further investigation was required to determine the radionuclide responsible for the peak at that energy, as many isotopes emit positrons and have gamma rays at 511 keV. In order to determine if the 511 keV peak was consistent with [¹¹C]O₂, four gamma spectroscopy measurements were taken of the soda lime trap over a period of approximately 41 minutes. The corrected peak area of the 511 keV peak was plotted as a function of the measurement start time and an exponential decay was fitted to the data in order to determine the decay constant of the radionuclide responsible for the peak. Radioactivity decays at an exponential rate following Equation 3.1:

$$\frac{dN}{dt} = -\lambda N \quad (\text{Equation 3.1})$$

where N is the quantity and λ is the decay constant. The differential equation can be solved as follows in Equation 3.2:

$$N(t) = N_0 e^{-\lambda t} \quad (\text{Equation 3.2})$$

where $N(t)$ is the quantity at a specific time, t , N_0 is the initial quantity at time=0, and λ is the decay constant.

3.2.3 Radiolysis Product Determination

Since hydrogen is known to be a major product of radiolysis, the production of hydrogen gas during the irradiation was measured using a Honeywell Midas Gas Detector (MIDAS-E-H2X). In order to achieve the specifications necessary for accurate readings on the sensor, an air flow of 500 mL/min through the lumen side of a membrane contactor was used. This met the flow rate requirement as well as diluting the amount of hydrogen gas in the stream for accurate measurement. Measurements from the hydrogen sensor were recorded every two minutes.

In order to predict the expected concentration of radiolytically produced hydrogen in the system during this irradiation, average linear energy transfer (LET) values were determined for $^{40}\text{Ca}^{20+}$ and compared to literature values.^{9,11-13} The LET values started at an energy of 4.998 GeV as the beam entered the water and were averaged over the energy range of the beam as it passed through the water until coming to a stop. Calculation of average LET for radiolysis calculations is based on Equation 3.3:

$$\frac{1}{E_0} \int_0^{E_0} \left(\frac{dE}{dx} \right) dE \quad (\text{Equation 3.3})$$

where E_0 is the initial energy and dE/dx is the stopping power of the beam. This equation was then used to predict a G-value (molecules of $\text{H}_2/100 \text{ eV}$) for hydrogen production based upon the literature values collected by Meesungnoen and Jay-Gerin shown in Figure 3.2 by plotting the

average LET value along the fitted line. It should be noted that the experiments used for comparison were performed under controlled conditions to measure the G-values as a function of LET, whereas the present experiment was not performed in a fully controlled environment with respect to LET. Therefore, the hydrogen production results from this experiment represent an *apparent* G-value based upon the conditions in which the experiment was performed under.

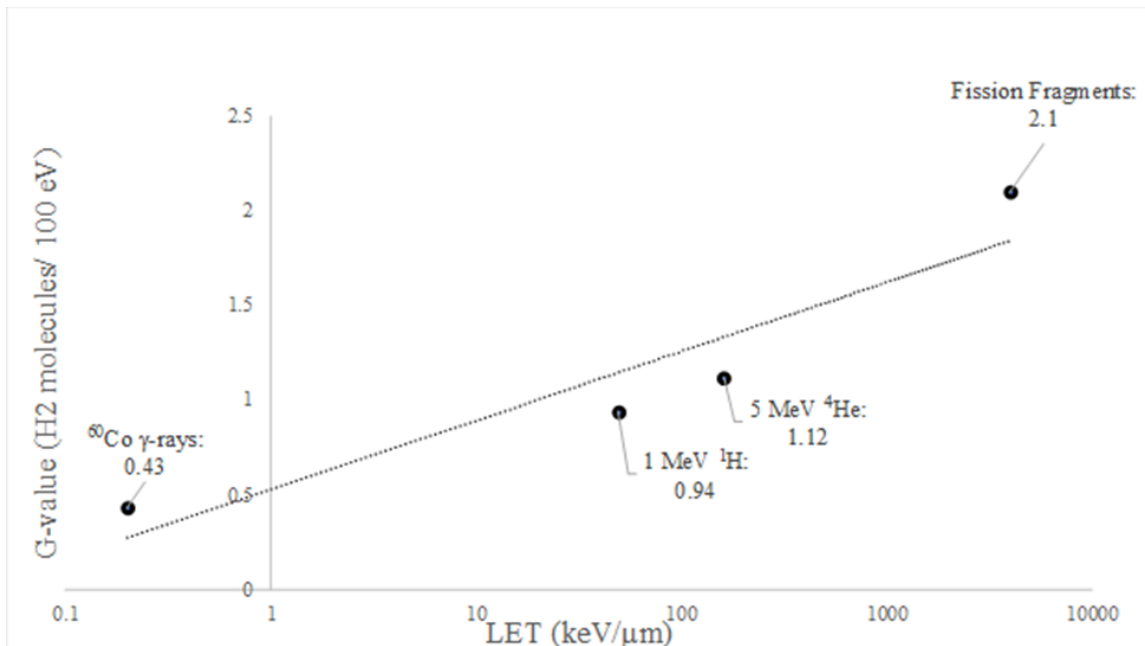


Figure 3.2: Experimental G-values from Meesungnoen and Jay-Gerin which were used to estimate the production of H₂ during the present experiment.^{9,11-13}

The average concentration of H₂ measured by the hydrogen sensor and the average beam current during the irradiation over the same time frame were parameters which were used to calculate the experimental *apparent* G-values. To convert the concentration of H₂ that was experimentally measured into the number of H₂ molecules per 100 eV, the air flow of 500 mL/min through the gas line and the ideal gas law were used. The total energy deposited from the beam into the water was calculated using SRIM and averaged over time. As stated previously, a Faraday cup was periodically inserted into the beamline ahead of the target in order

to get an accurate current measurement. When this measurement was taken, no hydrogen was produced inside the water chamber as radiolysis did not occur. As a result, during the total experiment, there are five separate sections of hydrogen production while beam was interacting with the target and the *apparent* G-value was calculated separately for each section.

3.2.4 Surface Analysis of the Titanium Window

In addition to observing the overall conditions of the system, production of radionuclides, and the presence of radiolysis productions, another purpose of this experiment was to determine the stability of the titanium window material. As part of this determination, analysis of the titanium window surface post-irradiation was performed using several techniques.

Through only visual observation of the titanium window disk, discoloration was seen from the beam spot. To prove that this discoloration was in fact in the same area as the irradiation took place, an optical image of the disk was produced. To further characterize the beam spot and determine whether the visual discoloration was due to oxidation of the surface of the window, scanning-electron microscopy (SEM) was used alongside energy-dispersive x-ray spectroscopy (EDS).

3.2.4.1 Digital and Scintillation Imaging Techniques

In order to understand more about the visual discoloration of the titanium window, both digital and scintillation images were taken of the disk. Digital optical images were collected of the titanium disk in order to capture the discoloration from the suspected beam spot area.¹⁴ These images were taken using a Keyence VHX-6000 Digital Microscope (DM).

The scintillation images were taken using a PerkinElmer IVIS Lumina LT In Vivo Imaging System (part number CLS36331) with and without a scintillating coversheet. Images taken without the scintillating material were simple digital images that could be used as overlay

comparisons to the images depicting areas of high radioactivity.¹⁵ The principles behind the instrumentation used to acquire these images can be found in Appendix A.

3.2.4.2 Scanning-Electron Microscopy

In addition to the optical and radiographic images taken of the irradiated disk, scanning-electron microscopy (SEM) was used alongside energy-dispersive x-ray spectroscopy (EDS) to further characterize the beam spot and to determine possible causes of discoloration. SEM was used to produce magnified images of the surface of the titanium disk and these magnified images were used to compare the differences between the beam spot and the rest of the disk. The titanium disk was imaged using a JEOL JSM 6610LV microscope. In order to produce quality images, SEM samples must be the proper size to fit on the stage, have sufficient conductivity characteristics, and be stable enough to withstand high vacuum. The titanium disk did not require any special sample preparation as it was small in diameter, thin, highly conductive, and made of solid material.

There are many different imaging modes in SEM, but the two used in this work were secondary electron image (SEI) mode and back-scattered electrons (BEC) mode. The SEI mode results in images with high resolution and magnification that produce information about the topography of the sample. The BEC mode results in images high in contrast, which can provide information about the composition of the sample.^{16,17}

The resolution of SEM images is mainly dependent upon the accelerating voltage of the incident beam. SEMs often get better resolution at lower acceleration voltages depending on the density of the sample; however, this parameter must be optimized. When utilizing the SEI mode, the accelerating voltage was set to 10 kV for optimal resolution at the magnification used. After switching to the BEC mode, the accelerating voltage was adjusted to 20 kV for better resolution

with more back-scattered electrons. The resolution of SEM images is also greatly affected by the spot size, which can range from 10-60. The spot size used for these images was 30..

In SEM, the depth-of-field is dependent on the aperture angle (α), which is determined by the aperture diameter and the working distance (the distance between the objective lens and the top of the sample). In order to optimize α , a combination method of increasing the working distance and decreasing the aperture diameter can be used. When utilizing both SEI and BEC modes, the working distance was 10 mm. More information behind the theory of SEM and SEI and BEC modes can be found in Appendix A.

3.2.4.3 Energy-Dispersive X-Ray Spectroscopy

In order to further characterize the Ti64 alloy disk further with chemical composition through elemental analysis, energy-dispersive x-ray spectroscopy (EDS) was used. When the beam of electrons from the SEM strike the sample, not only are secondary electrons and backscatter electrons emitted, but so are x-rays.¹⁷ A semi-quantitative measurement of the elemental composition of a sample is possible using EDS because after X-ray excitation, each element produces a unique fingerprint of peaks on an electromagnetic spectrum. In order to detect the X-rays, additional hardware is included in the SEM set up, but the same JEOL JSM 6610LV microscope was used.

Performing EDS on a sample also allows semi-quantitative analysis of the chemical composition of the sample. Using the Oxford AZtec quantitative program complex functions are performed on each peak within the spectrum to determine the net number of counts while subtracting background X-rays. The system also automatically performs matrix corrections to provide weight percentages in the range of $\pm 25\%$ accuracy; therefore, semi-quantitative. A more in-depth description of EDS theory can be found in Appendix A.

The same parameters that were used to image the sample in BEC mode were used for the EDS spectra collection and input into the Aztec program for composition calculations.

3.3 Results and Discussion

3.3.1 $^{40}\text{Ca}^{+20}$ Irradiation

During the irradiation, all of the probe measurements were recorded every 5 seconds. The results are represented in the graphs shown in Figure 3.3. Due to the use of membrane contactors and the Midas Hydrogen Gas Detector, the system was open to air for the dilution of the hydrogen gas through the analyzer. This allowed for the re-equilibration of both CO_2 and O_2 to occur in the system and the effect of equilibration can be seen in the results from the probes. Based upon the pH probe readings, the pH appeared to stay relatively constant over the course of the experiment with a slight increasing trend. The average pH during the experiment was 5.91. The expected pH of pure water with dissolved atmospheric CO_2 in an open system is 5.65, so this average reading suggests substantial re-equilibration of CO_2 between the atmosphere and the system.

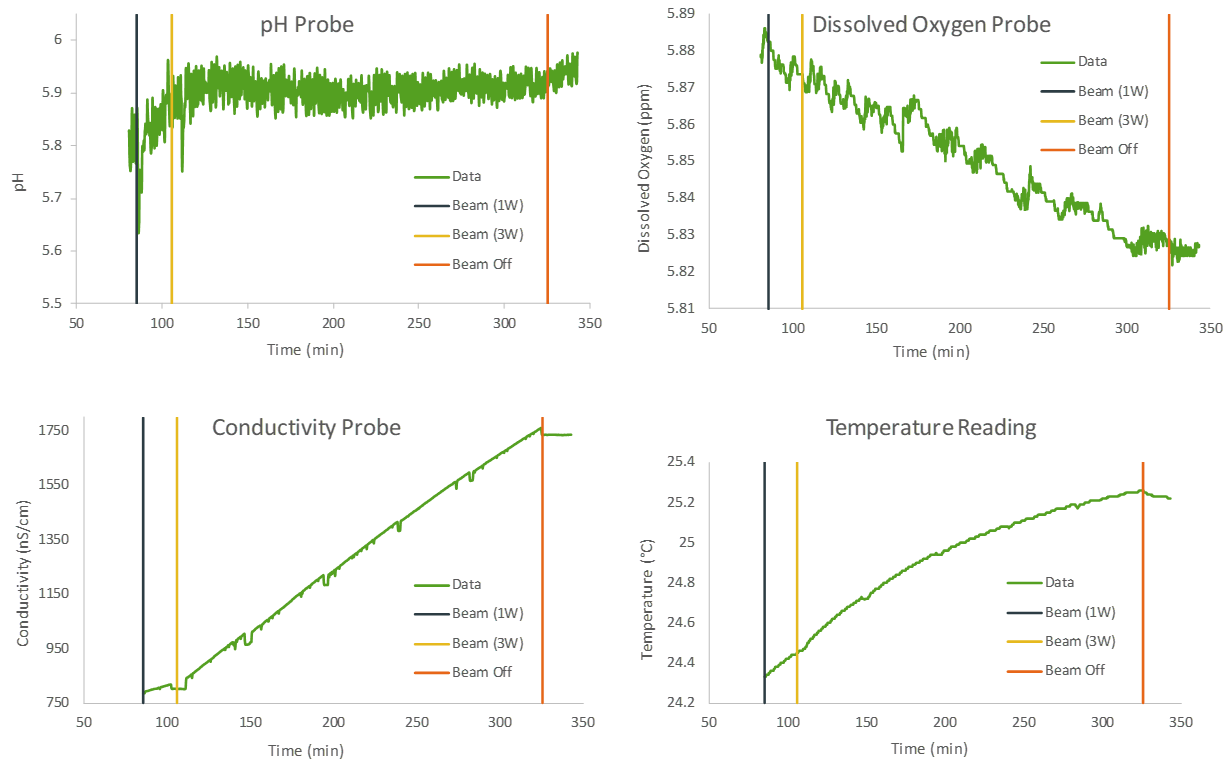


Figure 3.3: Measurements of the pH probe, dissolved oxygen probe, conductivity probe, and temperature during the irradiation. The blue vertical line represents the start of beam time at low intensity, the yellow line represents the start of beam time at higher intensity, and the orange line represents the end of irradiation.

During the experiment, there was radiolytic formation of H_2O_2 in addition to many other radicals, ions, and molecular species. Using platinized titanium mesh, some of the H_2O_2 was decomposed into H_2O and O_2 . This could have slightly increased the concentration of dissolved oxygen in the system. However, the membrane contactors were included in the system in order to sparge the water of dissolved gases including O_2 ; therefore, the possible increase in dissolved O_2 due to H_2O_2 degradation could not be observed. The dissolved oxygen reading decreased over time during the experiment, and as the equilibrium between the water and air was always being reestablished at one of the membrane contactors, this decrease was likely due to the increase of the water temperature over the course of the irradiation.

A steady climb in the conductivity is observed starting around 800 nS/cm and ending around 1800 nS/cm. This steady increase was believed to be due to a leeching of the potassium chloride electrolyte solution in the pH probe as well as from the re-equilibration with CO₂. Because of this leeching, the pH probe was not used in any future experiments as to not interfere with the conductivity readings. Finally, the temperature and the flow rate each stayed relatively constant throughout the experiment. The temperature climbed from 24.4°C at the beginning of irradiation to 25.2°C at the end of the irradiation. The flow rate began at around 1.01 L/min and ended around 1.02 L/min. Each of these trends were expected, as the flow of the water was typically constant during extended preliminary testing and the flow should have kept the temperature stable throughout the bulk solution, even during irradiation.

3.3.2 Gaseous Isotope Collection

Gamma spectroscopy measurements were taken of the two gas traps in the gas line of the system – the boric acid trap and the soda lime trap. Measurements of the boric acid trap resulted in no activity detected on the trap. Originally, this was thought to be due to complications during the experiment which caused a leak and delayed the measurements taken of the gas traps. [¹³N]H₃ was expected to collect on the boric acid trap and the half-life of ¹³N is only 9.965 minutes. There was; however, a 511 keV peak was present in the measurements of the soda lime trap. Many radionuclides produce gamma rays with an energy of 511 keV; therefore, in order to identify the radionuclide responsible for the activity present on the soda lime trap, the decay constant was calculated. A series of gamma measurements were taken of the trap with equal time duration and the results are listed in Table 3.1.

Table 3.1: Gamma spectroscopy data obtained from sequential measurements of the soda lime trap over a period of 40 minutes

Measurement	Start Time (s)	Peak Area
1	61446	534.4
2	61783	452.5
3	62118	378.7
4	63927	110.9

After plotting the corrected peak area versus the starting time of the measurement (Figure 3.4), Equation 3.2 was fitted to the data and the decay constant was found to be $5.95 \times 10^{-4} \text{ s}^{-1}$, which yielded a half-life measurement of 19.4 minutes. This value is very close to the true half-life of ^{11}C , 20.364 minutes. This result was expected as soda lime is known to trap CO_2 and as the system was exposed to atmospheric air and the CO_2 re-equilibrated over time.

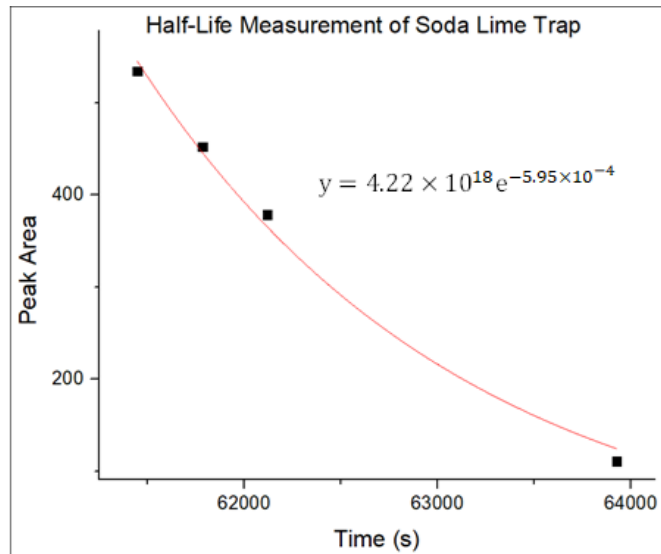


Figure 3.4: Graphical representation of the exponential radioactive decay fit to the gamma measurements taken of the soda lime trap over a period of 40 minutes to determine the decay constant of the radionuclide emitting 511 keV gamma rays. The decay constant was consistent with that of ^{11}C .

3.3.3 Radiolysis Product Determination

In order to model the production of hydrogen by radiolysis, the recorded measurements from the hydrogen sensor were observed and analyzed during the course of the experiment and post-irradiation. The observed production rate of hydrogen is shown in Figure 3.5. The separate segments of the irradiation can be seen in this graph (one during the low current highlighted in orange and four during the high current). During the time periods that the Faraday cup was inserted to intercept the beam, the hydrogen concentration decreased quickly as the hydrogen gas which was produced in the water chamber was removed through the membrane contactor, which can also be seen in the graph. In addition to the separate beam current segments which were observed in Figure X, a qualitative decreasing trend in the concentration of hydrogen was also observed over the entire irradiation period.

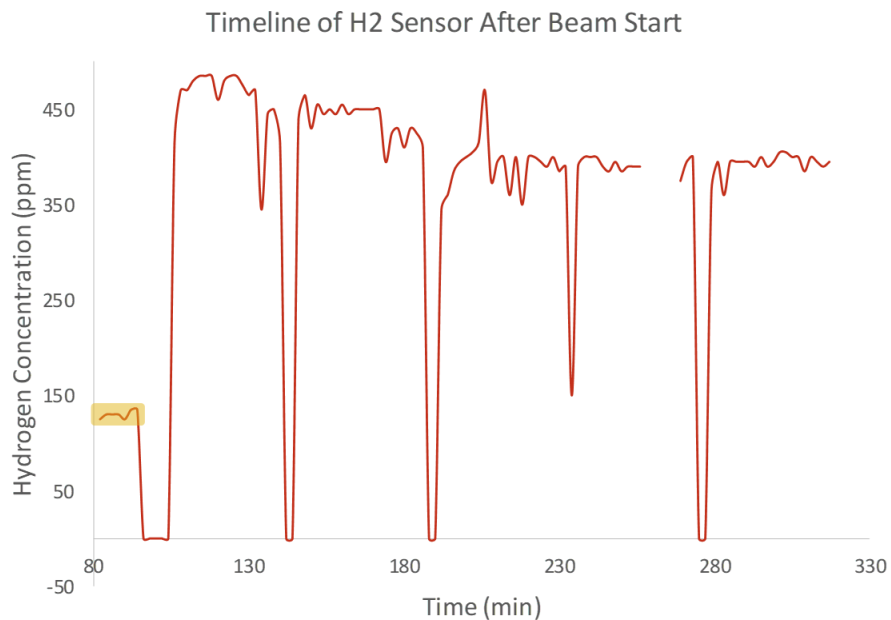


Figure 3.5: Depiction of the hydrogen sensor reading during irradiation. The segment highlighted in orange at the beginning corresponds to the period of low intensity irradiation. Each decrease in the graph to zero is due to interception of the beam by the Faraday cup.

An average *apparent* G-value was predicted for the entire irradiation using the stopping power calculated by SRIM. The average LET along the particle track in the water was approximately 700 keV/μm. After plotting this LET value along with the literature values (Figure 3.6) described in Section 3.2.3, the average predicted value for hydrogen production was calculated to be 1.57 molecules of H₂ per 100 eV.^{9,11-13}

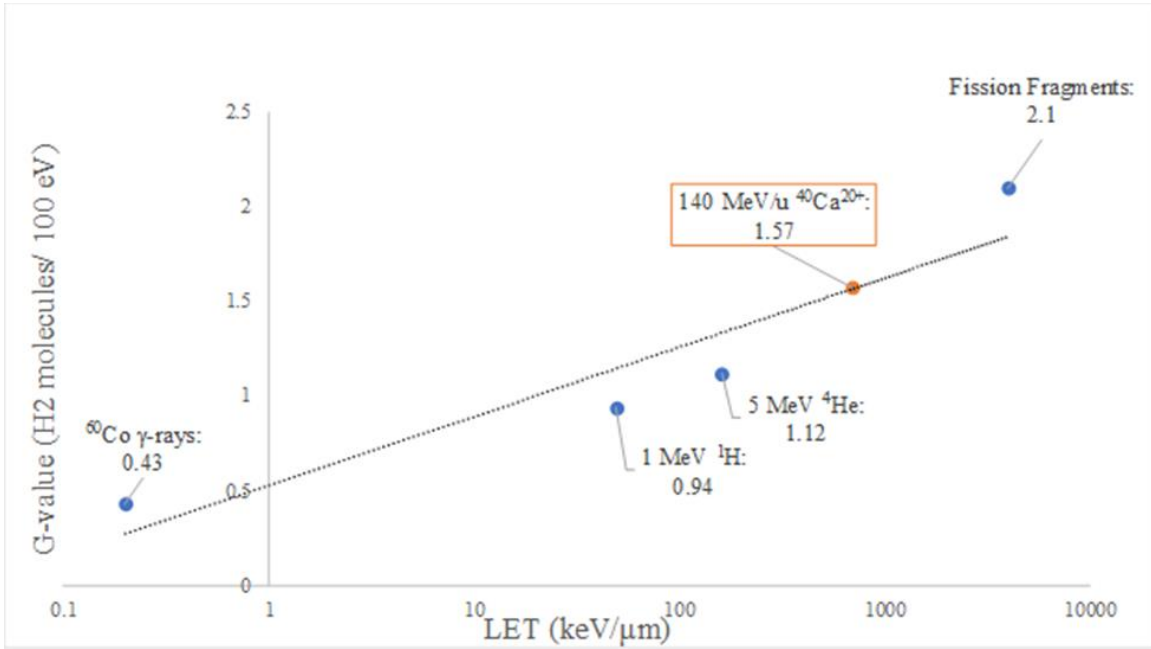


Figure 3.6: Experimental G-values used to estimate the H₂ production with the irradiation of 140 MeV/nucleon ⁴⁰Ca beam of approximately 700 keV/μm LET.

The experimental *apparent* G-values were calculated from the hydrogen measurements during the different segments of the experiment and all calculated values indicated a lower production rate of hydrogen than the predicted value. The results from each segment are shown in Table 3.2, with the lowest beam intensity segment resulting in the highest *apparent* G-value. The apparent values are on the order of one-half the predicted value.

Table 3.2: The average hydrogen gas production and *apparent* G-values during each segment of irradiation

Beam Intensity (enA)	Average Measured H₂ Concentration (ppm)	Average <i>Apparent</i> G-value (molecules H₂/100 eV)
2.1	130	0.91(9)
8.6	466	0.79(8)
8.5	438	0.75(8)
8.0	391	0.72(7)
8.2	393	0.70(7)

3.3.4 Surface Analysis

3.3.4.1 Digital and Optical Imaging Techniques

Visual observation of the titanium window post irradiation resulted in the realization that there was an area of discoloration on the rough side of the window in the vicinity of the expected beam spot area. The visual discoloration was lighter than the surrounding area of the window. In order to capture this discoloration, a digital image was taken of the window and the results are shown in Figure 3.7a. The area in the yellow circle shows the area of the discoloration to the naked eye.

In order to prove that this discoloration was in fact due to the irradiation and matched up with the beam spot, optical imaging of the disk was performed. The optical image that was captured is shown in Figure 3.7b. The highlighted area of the optical image represents the area with a large number of photons produced by the scintillating material, where red indicates highest luminescence and blue indicates lower. The number of photons correlates with the amount of radioactivity. Note that the area with a high number of photons (the area of irradiation) corresponds with the discoloration of the window material.

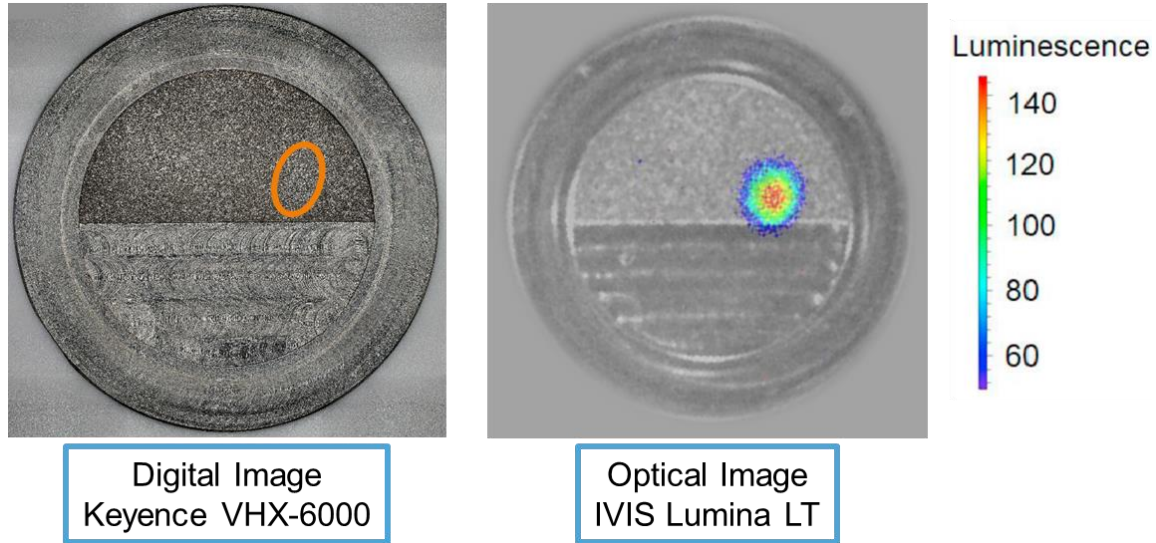


Figure 3.7: Side-by-side comparison of the digital and scintillation images of the titanium window disk demonstrating the location of the beam spot. The luminescence scale is uncalibrated and serves to show the relative intensity of the radioactivity.

3.3.4.2 Scanning-Electron Microscopy

After the images were taken of the discoloration and the area of activity on the window was measured, high-magnification microscopy images were captured to observe the surface of the disk. SEM images were collected in SEI mode from three sample areas – (1) a non-irradiated disk, (2) a non-irradiation site from the irradiated disk, and (3) an irradiation site from the irradiated disk. In SEI mode, topographical information was collected, and no differences were observed among the three samples. Each sample surface consisted of both rough areas that contained a variety of spherical particles as well as smooth areas, which can be seen in Figure 3.8. These spherical particles had diameters ranging from 5 μm to 75 μm . Even with the differences in texture within each sample, the overall textures were similar among the three sample areas as also seen in Figure 3.8.

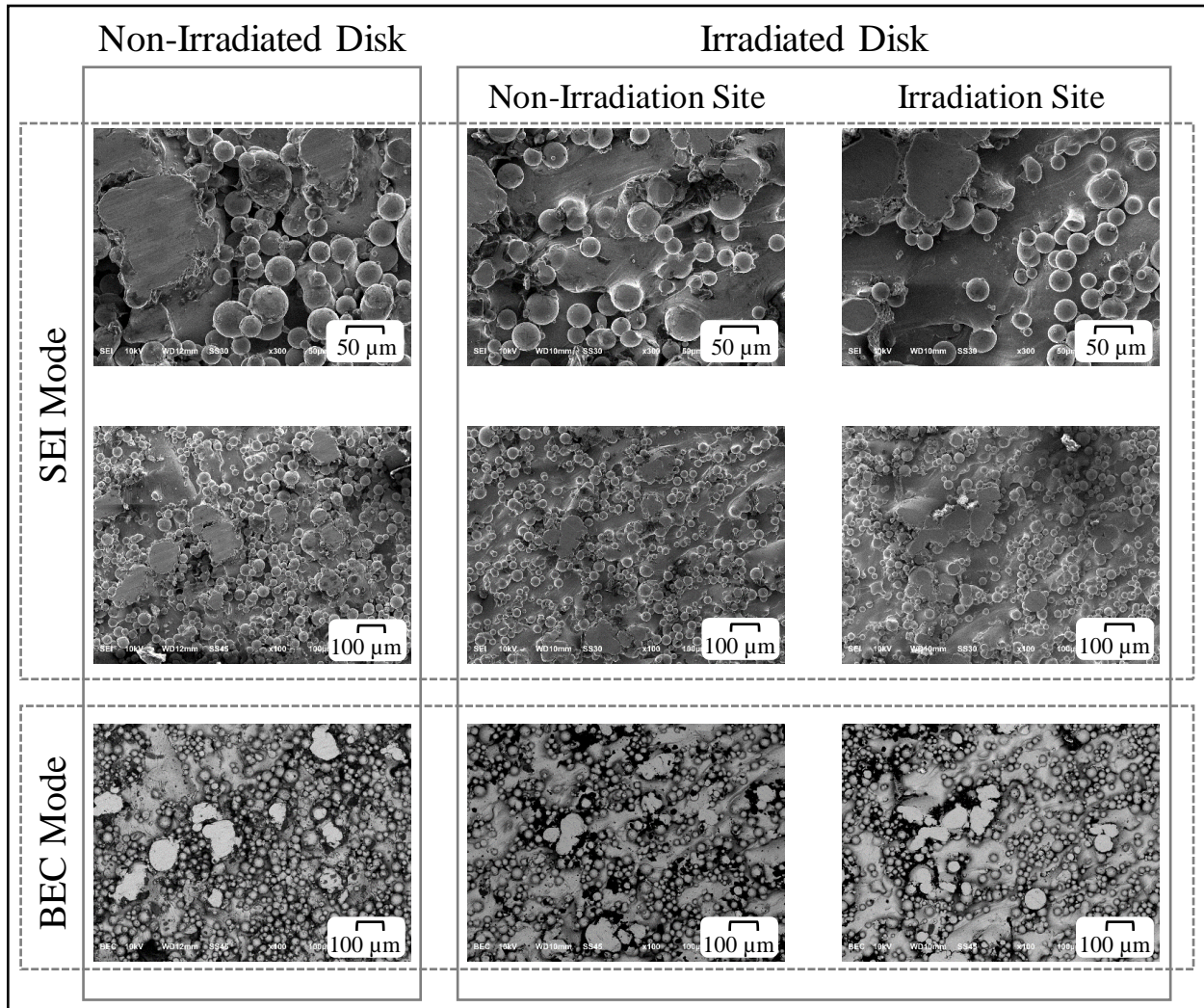


Figure 3.8: SEM images in SEI and BEC mode of the non-irradiated and irradiated disk.

The SEM results in BSE mode indicated differing contrast in certain areas of the sampled regions (Figure 3.8). While using BEC mode, the BEC coefficient of known elements or compounds can be determined and this number is related to the percent of beam electrons which are backscattered from those areas within the sample. Compounds or elements with higher atomic average atomic number will appear brighter in BSE mode than those with lower average atomic number. Therefore, these contrast differences could have been due to the different elements within the titanium alloy (Ti=22, Al=13, and V=23). These differences in contrast were

seen to be consistent across all three sample areas, so there were no observed differences between irradiated and non-irradiated disks.

3.3.4.3 Energy-Dispersive X-Ray Spectroscopy

Due to the differences in contrast seen in BEC mode, EDS maps were taken in order to semi-quantitatively determine the elemental compositions of each sampled region. The resulting elemental maps are demonstrated in Figure 3.9. In the Ti64 alloy, titanium, aluminum, and vanadium were relatively evenly distributed across the sampled areas according to the EDS maps.

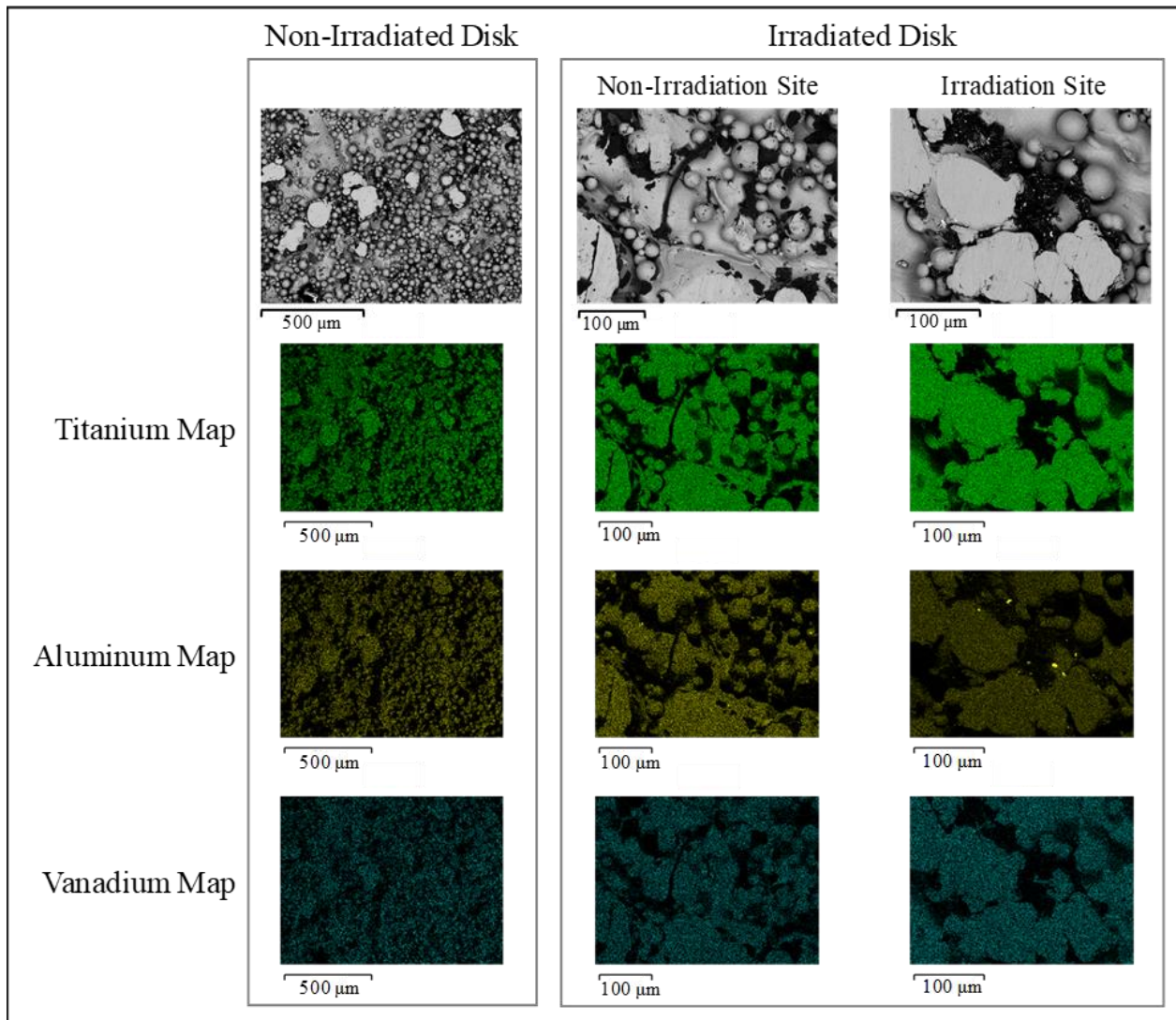


Figure 3.9: EDS images and elemental composition maps of the three elements included in the Ti64 alloy on the non-irradiated and irradiated disks.

The regions that appeared to have darker contrast in BEC mode appeared to be made up of mostly carbon and oxygen according to the EDS results depicted in Figure 3.10. Those regions were determined to be debris from handling. As the debris was seen across all the samples on both the non-irradiated maps as well as the irradiated maps, it was determined to be insignificant during comparison.

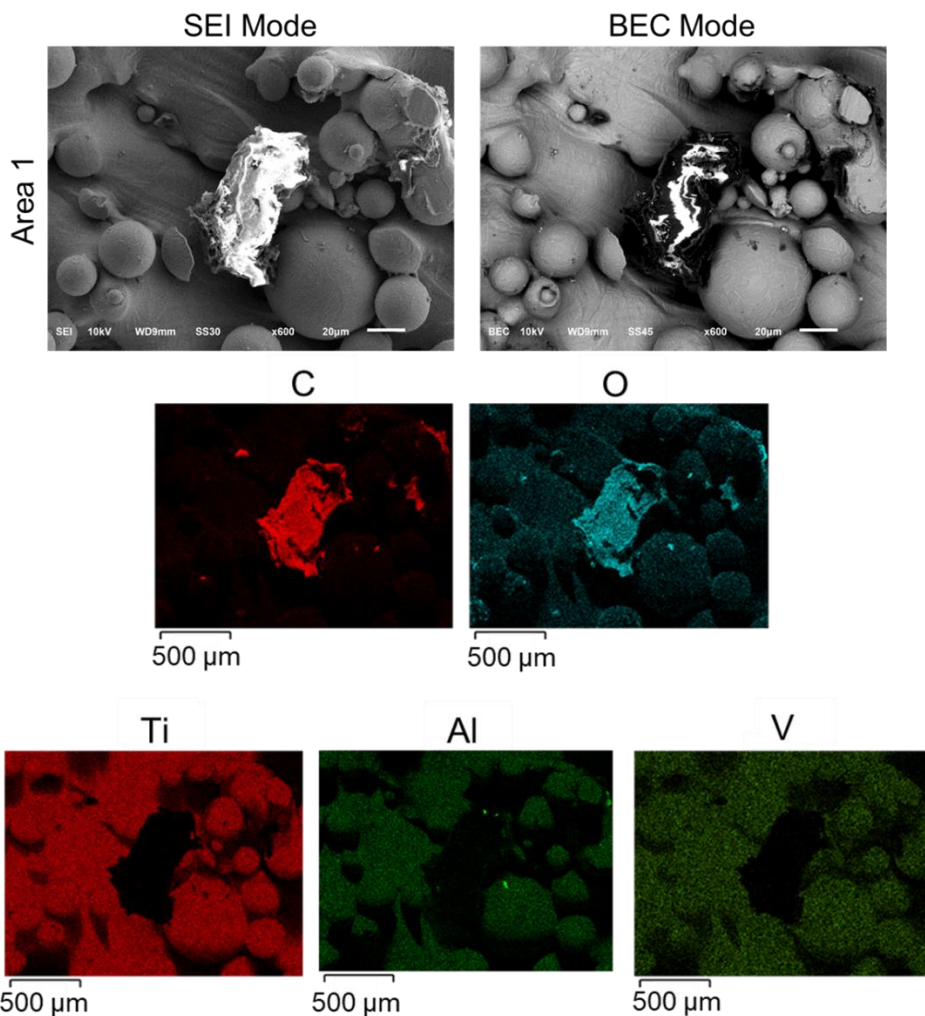


Figure 3.10: Example EDS images and elemental composition maps of an area of debris on the Ti64 disk including the elements of the alloy as well as carbon and oxygen as the main components in the make-up of the debris.

Using the semi-quantitative ability of EDS, percent by mass for each element of the alloy was calculated for irradiated disk and the non-irradiated disk. EDS measurements were collected in four similar areas of each disk – center, top center, top left, and bottom center (Figure 3.11) – and these measurements were used as n=4 for the standard deviation calculation in each value. These measurements resulted in very similar percent by mass measurements for the non-irradiated and irradiated disks. The results in Table 3.3 demonstrated that there was no

significant difference in elemental composition between the two disks according to the semi-quantitative data.



Figure 3.11: Depiction of the regions used for the semi-quantitative measurement of the elemental composition.

Table 3.3: Comparison of the semi-quantification of the elemental composition of the non-irradiated and irradiated Ti64 disks. All calculations are in weight percent.

	Titanium	Aluminum	Vanadium
Non-Irradiated	89.5(6)	5.4(4)	5.1(9)
Irradiation	89.6(1)	4.9(4)	5.5(4)

3.4 Conclusions

During this experiment, the first iteration of the water-filled target and water system were irradiated with a beam of 140 MeV/nucleon ^{40}Ca at a range of 0.1 to 0.4 pA over the course of 3.5 hours. The purposes of this irradiation included testing the stability and chemical resistance of the Ti64 alloy material chosen for the FRIB beam dump blocker, observing the radionuclides

produced in the aqueous and gaseous phases of the water system, measuring the production rate of hydrogen as a radiolysis product, and analyzing the Ti64 material surface post-irradiation.

This experiment demonstrated the ability to use a flowing-water target in order to produce and harvest radionuclides in both the aqueous and gaseous phases from a stable accelerated beam at the NSCL. ^{11}C was collected and identified on the soda lime trap in the gas line of the harvesting system, showing the potential of gas-phase harvesting in the future. The presence of ^{11}C on the soda lime trap also reinforced the concept that CO_2 was able to re-equilibrate within the water system during irradiation.

The production and effects of radiolysis products such as hydrogen were also observed during this experiment. The hydrogen gas produced through radiolysis was measured at the two different beam intensities and was compared to theoretical production estimates. The amount of hydrogen gas measured was lower than the predicted level, indicating that radiolysis products in our system may recombine to a larger extent than previously thought. Additionally, the value continued to decrease as the irradiation progressed, suggesting that the build-up of radiolysis products in the water led to a lower amount of H_2 being produced or escaping from the target. The observed hydrogen production was most likely indicative of what can be expected in future isotope harvesting experiments at both the NSCL and FRIB.

The effects of radiolysis on the system components, especially the target window, were explored by performing SEM and EDS analysis on the target window. The SEM images of the target window showed no observable changes in the topography of the irradiated target material and EDS compositional maps of the target window showed no statistical difference in the elemental abundance on the irradiated disk compared to an identical non-irradiated target disk.

The consistent elemental abundances in the two disks further supported the conclusion that there was no significant target degradation.

Based upon the visual observations of the titanium window, the SEM and EDS results, and ICP-OES results of the water, it was determined that the Ti64 alloy material was substantial enough to proceed with 3D printing the water-filled beam blocker to be used at the NSCL. Additionally, the materials used for the water system were found to be sufficient for isotope harvesting through this production method. However, there were several areas for improvement to optimize the harvesting system, including the replacement of the hydrogen sensor with a probe that would not require atmospheric air dilution for accurate measurements and remove the need for CO₂ re-equilibration in the system. The information obtained through this experiment was used for the future development of the system moving forward with higher intensity irradiations.

APPENDIX

THEORY OF INSTRUMENTATION UTILIZED IN CHAPTER 3

Gamma Spectroscopy

Gamma spectroscopy allows for the identification and quantification of radionuclides through the analysis of the gamma-ray energy spectrum. Nuclei have different energy levels similar to the energy levels of atoms and can emit photons of particular energies.¹⁸ The particular energy levels of nuclei are characteristic of each radionuclide, so that the photon energies of the gamma rays emitted correspond to the energy differences of the nuclei and can be used to identify particular elements and isotopes.¹⁸ In this work, gamma rays were detected using a BEGe or Broad Energy Germanium detector.¹⁹

Gamma-ray spectrometers must be calibrated for accurate quantification of radionuclide species. Calibration involves placing a known source, with multiple gamma-ray energy emissions, at a known distance from the detector to acquire a spectrum to be used as the calibration certificate. Quantification of activity requires knowledge of the detector efficiency, gamma-ray emission probability for each radionuclide, and a correction for radioactive decay during spectrum collection.¹⁹

Optical and Scintillation Imaging

In order to analyze the visual discoloration observed on the titanium window, both digital and scintillation images were taken of the disk. Digital images were collected using a Keyence VHX-6000 Digital Microscope (DM). Digital microscopes have many advantageous capabilities including a wide magnification range (1X to 5,000X), true color, and no need for sample preparation. The microscope which was used contained an “image stitching” feature which

allowed for numerous images of different areas of the disk to be captured and then combined to yield an image of the entire disk with higher resolution.²⁰

The scintillation images were taken using a PerkinElmer IVIS Lumina LT In Vivo Imaging System (part number CLS36331) with and without a scintillating coversheet. When using the scintillating material to cover the disk, electrons escaping the disk create excitation within the scintillator, causing it to glow. Using a digital camera charged-coupled device placed behind a lens, the number of photons produced by the scintillator could be counted, which would be proportional to the amount of radioactivity.²¹

Scanning Electron Microscopy

In addition to the optical images taken of the irradiated disk, scanning-electron microscopy (SEM) was used alongside energy-dispersive x-ray spectroscopy (EDS) for further surface analysis of the disk. SEM was used to produce magnified images of the surface of the titanium disk and these magnified images were used to compare the differences between the beam spot and the rest of the disk. This technique works by scanning the surface of a sample with a focused beam of electrons which will produce a variety of different signals based upon the interactions of the electron beam at various depths within the sample, demonstrated in Figure A.2.²² The varying signals will produce images of the sample.

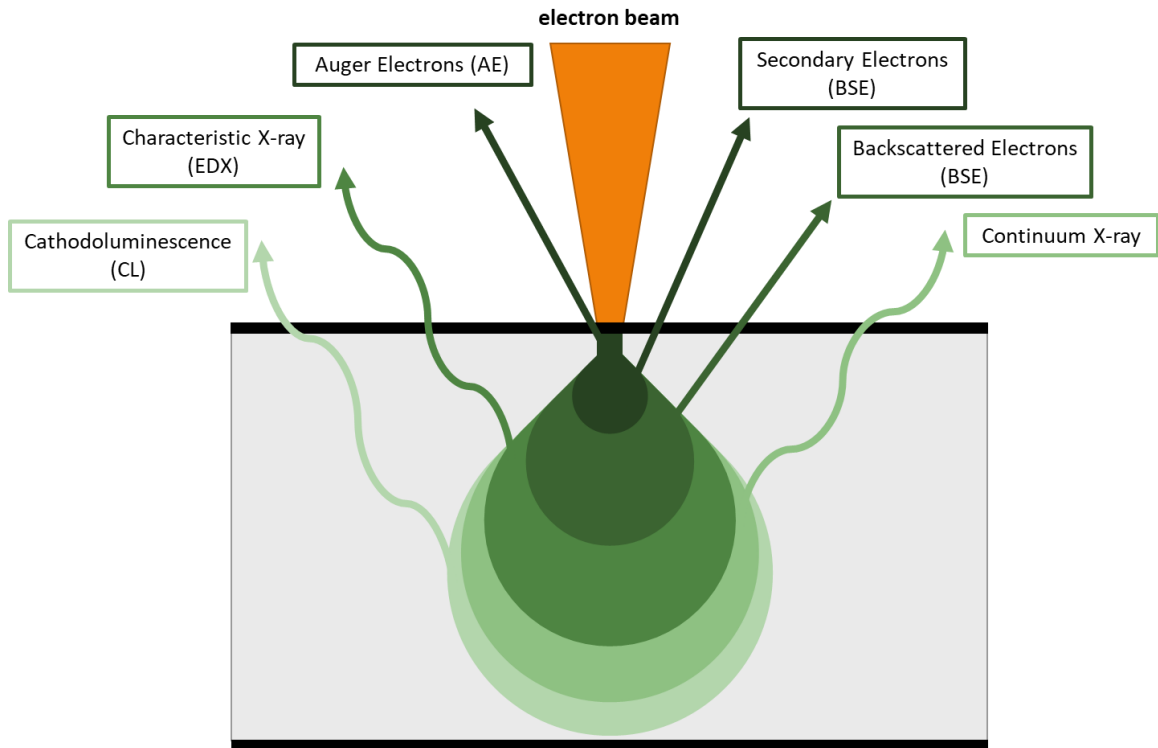


Figure A.1: Example of the variety of signals produced by the interaction of an electron beam with a sample surface. The depth of the beam interaction with the sample to produce each type of signal is also demonstrated.

The most common SEM signal is produced from secondary electrons utilizing secondary electron image (SEI) mode.²³ Secondary electrons have very low energies (around 50 eV), which means the electron-matter interaction only occurs on the top surface of the sample (<10 nm deep). Secondary electrons are ejected from conduction or valence bands of the sample through inelastic scattering interactions with the beam electrons. These electrons are typically detected using an Everhart-Thornly detector, which consists of a scintillator, Faraday cage, and photomultiplier for detection.²² A low positive voltage is applied to the Faraday cage in order to attract low energy electrons (<50 eV) and the scintillator has a high positive voltage (around 10,000 V) to accelerate the incoming electrons to be converted to light photons. From here, the

photons travel outside of the vacuum of the microscope to a photomultiplier tube for amplification.²³

Another common signal is produced from back-scattered electrons by utilizing BEC mode. Back-scattered electrons are reflected from the sample through elastic scattering and have much higher energy than secondary electrons.²³ Due to the higher energy, back-scatter electrons interact at locations much deeper within the sample (Figure A.3) and can provide information about the distribution of compounds within a sample. Heavier elements with high atomic numbers backscatter electrons more strongly than lighter elements with low atomic numbers; therefore, BEC mode can be used to image differences in chemical composition. Because of the higher energy of backscatter electrons, the low positive voltage on the Everhart-Thornly detector is not efficient enough to attract the electrons for detection. Instead, a semiconductor detector is placed on the bottom of the final lens pole piece in order to detect the backscatter electrons as they travel directly upwards from the sample.²³

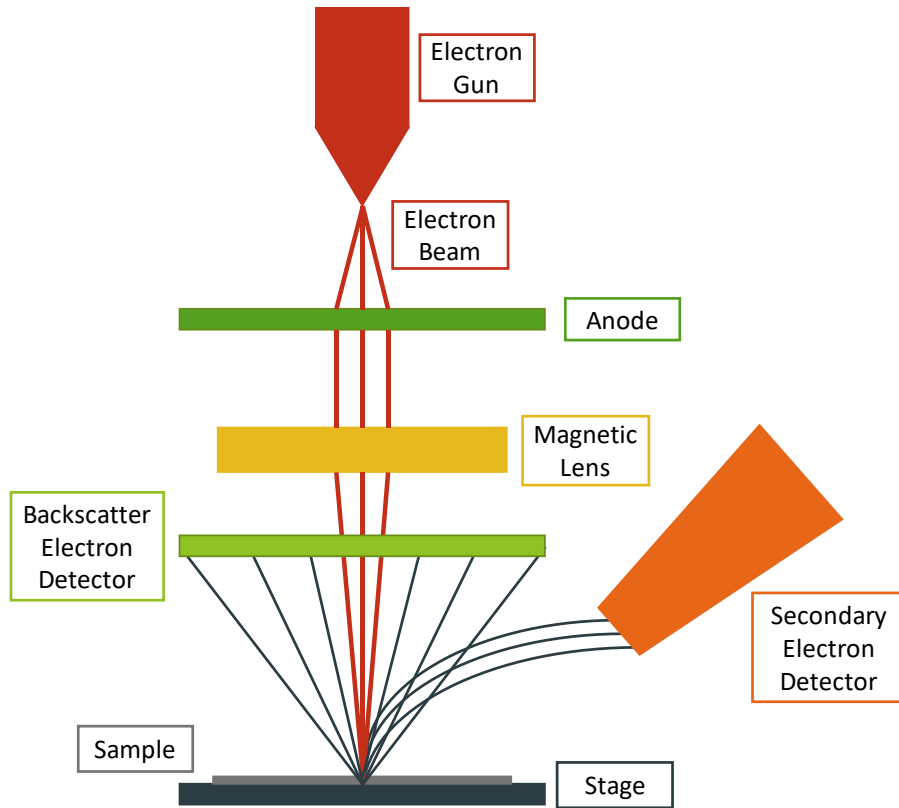


Figure A.2: Simple schematic of an SEM microscope and the components involved for imaging in both SEI and BEC modes.

Energy-Dispersive X-Ray Spectroscopy

In order to further characterize the Ti64 alloy disk further with chemical composition through elemental analysis, energy-dispersive x-ray spectroscopy (EDS) was used. When the beam of electrons from the SEM strike the sample, not only are secondary electrons and backscatter electrons emitted, but so are x-rays.²³

Characteristic x-ray production occurs through the following process. When an incident beam of electrons interacts with the surface of a sample, an electron from the inner shell can be displaced (Figure A.4). Following this imbalance, an electron from the outer shell can fill the vacancy in the inner shell. Outer shell electrons have greater energy than inner shell electrons and this excess energy can be released in the form of an x-ray.²³ The energies of the X-rays are

characteristic of the difference in energy between the two shells and of the atomic structure of the emitting element. As the number and energy of the emitted X-rays can be detected by an energy-dispersive spectrometer, the elemental composition of the sample can be measured.²³

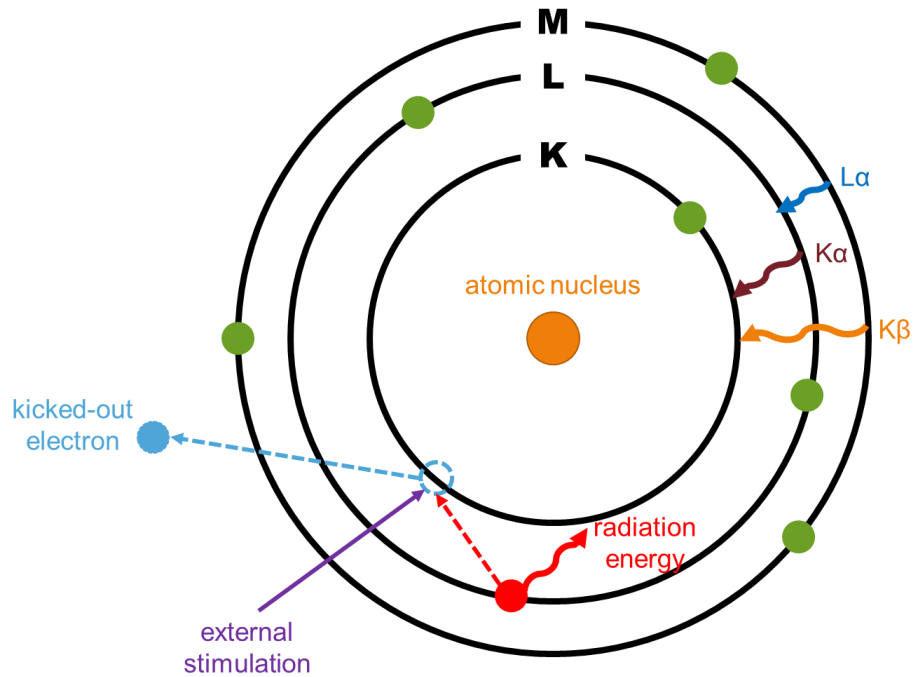


Figure A.3: Representation of X-ray production within an atomic nucleus

In order to detect the X-rays, additional hardware is included in the SEM set up (Figure A.5). This includes a collimator to absorb non-straight X-rays, an electron trap inside of the collimator to trap back-scattered electrons and ensure they are not misinterpreted as X-rays, a window to prevent contamination of the detector crystal, the detector crystal made of lithium and high purity silicon as a semiconductor, and a field effect transistor integrated into the detector crystal to separate the produced X-rays from the bias voltage.

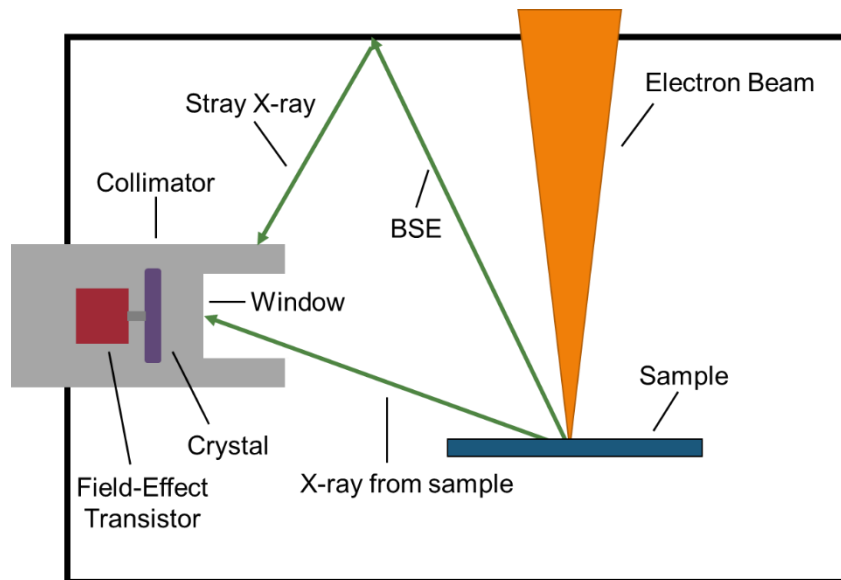


Figure A.4: Simple schematic of the additional hardware included with the SEM microscope for EDS spectra collection

The semi-quantitative properties of EDS are made possible through the use of a software with capabilities to perform complex functions for each characteristic peak. Part of these functions include matrix corrections, or ZAF corrections. The Z correction is for the atomic number effect. When there are multiple elements in a sample, there may be interferences that increase or decrease the number of x-rays detected for each element. The software calculates the impact of the other elements in the matrix on each specific element's X-rays and makes a correction. The A correction adjusts for absorption. The presence of multiple elements in a sample may lead to absorption of X-rays from one element to another. The distance traveled by the X-rays is imperative for the correction. And finally, the F correction adjusts for fluorescence. X-rays have the potential to produce other X-rays and an adjustment must be made to account for the extra production.

REFERENCES

REFERENCES

- 1) Pen, A.; Mastre, T.; Peaslee, G. F.; Petrasky, K.; Deyong, P. A.; Morrissey, D. J.; Lapi, S. E. Design and construction of a water target system for harvesting radioisotopes at the National Superconducting Cyclotron Laboratory. *Nucl. Instruments Methods Phys. Res. Section A. Accelerators and Spectrometers*. **2014**, 747, 62-68.
- 2) Mastren, T.; Pen, A.; Peaslee, G. F.; Wozniak, N.; Loveless, S.; Essenmacher, S.; Sobotka, L. G.; Morrissey, D. J.; Lapi, S. E. Feasibility of isotope harvesting at a projectile fragmentation facility: ^{67}Cu . *Scientific Reports*, **2014**, 4, 1-6.
- 3) Mastren, T.; Pen, A.; Loveless, S.; Marquez, B. V.; Bollinger E.; Marois, B.; Hubley, N.; Brown, K.; Morrissey, D. J.; Peaslee, G. F.; Lapi, S. E. Harvesting ^{67}Cu from the Collection of a Secondary Beam Cocktail at the National Superconducting Cyclotron Laboratory. *Analytical Chemistry*, **2015**, 87, 10323-10329.
- 4) Loveless, C. S.; Marois, B. E.; Ferran, S. J.; Wilkinson, J. T.; Sutherlin, L.; Severin, G.; Shusterman, J. A.; Scielzo, N. D.; Stoyer, M. A.; Morrissey, D. J.; Robertson, J. D.; Peaslee, G. F.; Lapi, S. E. Harvesting ^{48}V at the National Superconducting Cyclotron Laboratory. *Applied Radiation and Isotopes*, **2020**, 157, 109023.
- 5) Avilov, M.; Aaron, A.; Amroussia, A.; Bergez, W.; Boehlert, C.; Burgess, T.; Carroll, A.; Colin, C.; Durantel, F.; Ferrante, P.; Fourmeau T.; Graves, V.; Grygiel, C.; Kramer, J.; Mittig, W.; Monnet, I.; Patel, H.; Pellemoine F.; Ronningen R.; Schein, M. Thermal, Mechanical, and Fluid Flow Aspects of the High Power Beam Dump for FRIB. *Nuclear Instruments and Methods in Physics Research Section B. Interactions with Materials and Atoms*. **2016**, 376, 24-27.
- 6) Gade, A.; Sherrill, B. M. NSCL and FRIB at Michigan State University: Nuclear Science at the Limits of Stability. *Physica Scripta*. **2016**, 91 (5), 053003.
- 7) Campi, X.; Hüfner. Nuclear Spallation-Fragmentation Reactions Induced by High-Energy Projectiles. *Physical Review C*. **1981**, 24 (5), 2199-2209.
- 8) Sander, R. Compilation of Henry's law constants (version 4.0) for water as solvent. *Atmospheric Chemistry and Physics*, **2015**, 15, 4399-4981.
- 9) Meesungnoen, J.; Jay-Gerin, J. P. High-LET radiolysis of liquid water with $^1\text{H}^+$, $^4\text{He}^{2+}$, $^{12}\text{C}^{6+}$, and $^{20}\text{Ne}^{9+}$ ions: effects of multiple ionization. *Journal of Physical Chemistry*, **2005**, 109
- 10) Ziegler, J. F.; Ziegler, M. D.; Biersack, J. P. SRIM – The Stopping and Range of Ions in Matter. *Nucl. Instrum. Methods B268*. **2010**, 268, 1818 – 1823.

- 11) Bibler, N. E. Radiolysis of 0.4 M sulfuric acid solutions with fission fragments from dissolved californium-252. Estimated yields of radical and molecular products that escape reactions in fission fragment tracks. *Journal of Physical Chemistry*, **1975**, *79*, 1991-1995.
- 12) LaVerne, J. A. Detection of gaseous products in the radiolysis of aqueous solutions. *Journal of Physical Chemistry*. **1988**, *92*, 2808-2809
- 13) LaVerne, J.A. Chapter 14: Radiation Chemical Effects of Heavy Ions In: *Charged Particle and Photon Interactions with Matter: Chemical, Physicochemical, and Biological Consequences with Applications*, **2003**, 403-430
- 14) Digital Imaging: Introduction. *Microscopy Alliance*, **2021**, Accessed 7/12/2021, <http://microscopy.arizona.edu/learn/digital-imaging-introduction>
- 15) Bell, D. J.; Vajuhudeen, Z. Scintillator (gamma camera). *Radiopaedia*, **2021**
- 16) Scanning Electron Microscopy. *nanoScience Instrument*, **2021**, Accessed 07/12/2021 <https://www.nanoscience.com/techniques/scanning-electron-microscopy/>
- 17) Goldstein, J. Scanning Electron Microscopy and X-Ray Microanalysis. Springer. **2003**.
- 18) Knoll, G. *Radiation Detection and Measurement*. John Wiley & Sons, Inc. NY:2000, ISBN 0-471-07338-5.
- 19) Gorzkiewicz, K.; Mietelski, J. W.; Kierepko, R.; Brudecki, K. Low-background, digital gamma-ray spectrometer with BEGe detector and active shield. *Journal of Radioanalytical and Nuclear Chemistry*, **2019**, *322*, 1311-1321.
- 20) Digital Imaging: Introduction. *Microscopy Alliance*, **2021**, Accessed 7/12/2021, <http://microscopy.arizona.edu/learn/digital-imaging-introduction>
- 21) Bell, D. J.; Vajuhudeen, Z. Scintillator (gamma camera). *Radiopaedia*, **2021**
- 22) Scanning Electron Microscopy. *nanoScience Instrument*, **2021**, Accessed 07/12/2021 <https://www.nanoscience.com/techniques/scanning-electron-microscopy/>
- 23) Goldstein, J. Scanning Electron Microscopy and X-Ray Microanalysis. Springer. **2003**.

IV. The Investigation of Gas-Phase Harvesting Capabilities at the NSCL during a ^{78}Kr Irradiation

4.1 Introduction

By testing the first iteration target and water system during the ^{40}Ca irradiation, the proposed Ti64 alloy (grade 5 alloy: 6% Al, 4% V, mass balanced with Ti) was found to be stable under irradiation conditions and was determined to be a suitable material for moving forward with future irradiation experiments.¹ Following the ^{40}Ca irradiation, the second iteration of the beam blocker, closer in design to the beam dump to be used in the Facility for Rare Isotope Beams (FRIB), was developed as well as a new version of the harvesting system.^{2,3,4} The new system was tested during a ^{78}Kr irradiation, which provided the opportunity to test the capability of simultaneously harvesting radionuclides from the aqueous and gaseous phases. The results from aqueous phase harvesting during the ^{78}Kr irradiation were discussed by Domnanich *et al.*⁵ For the gas phase, an upgraded gas processing system was designed to move the dissolved gaseous radionuclides that were produced in the water to gas collection traps.⁴ The motivation for the development was to capture ^{76}Kr and ^{77}Kr and generate medically relevant bromine radioisotopes, ^{76}Br and ^{77}Br , respectively as a proof-of-concept for the ability to harvest gaseous radionuclides at the future FRIB facility.

As described in Chapter 1, radioisotopes of bromine, such as ^{76}Br and ^{77}Br , are uniquely suitable radiolabels for small molecule theranostic radiopharmaceuticals. As a radiohalogen theranostic pair, ^{76}Br and ^{77}Br could become a valuable tool for systemic targeted radiotherapy.^{6,7,8} Each isotope possesses many advantageous properties which have promise as PET imaging tracers and for therapy in small tumors.

Through the differences in half-lives of the parent $^{76/77}\text{Kr}$ radioisotopes, the two daughter radioisotopes, $^{76/77}\text{Br}$, can be generated and isolated from one another for use in nuclear medicine applications (Section 1.3).⁶⁻¹⁰ This generator process was tested utilizing the new gas processing system which included new components described in Section 2.2.2.

The results from this experiment demonstrate the successful use of the newly developed isotope harvesting gas-processing line to collect radioactive noble gases to generate pure radiohalogens. This experiment also provided more data about the chemical state of the water during irradiation as more data was collected measuring the rate of radiolytic hydrogen production.

4.2 Materials and Methods

4.2.1 ^{78}Kr Irradiation

The second iteration of the water-filled target described in Section 2.2.1 was irradiated at the NSCL with a 150 MeV/nucleon beam of ^{78}Kr . The irradiation took place over a period of 11 hours with an intensity range of 0 – 4 particle-nanoAmperes (pnA) for a total of 16 pnA·h. The beam current was measured using an unsuppressed target and was recorded approximately every second. The unsuppressed values were calibrated against a Faraday cup which was inserted periodically during the irradiation and intercepted the beam at the different ranges of current. A linear relationship between the accurate beam current values measured by the Faraday cup and the relative measurements on the target was determined in order to correct the unsuppressed recorded values. The results of this linear scale are demonstrated in Figure 4.1.

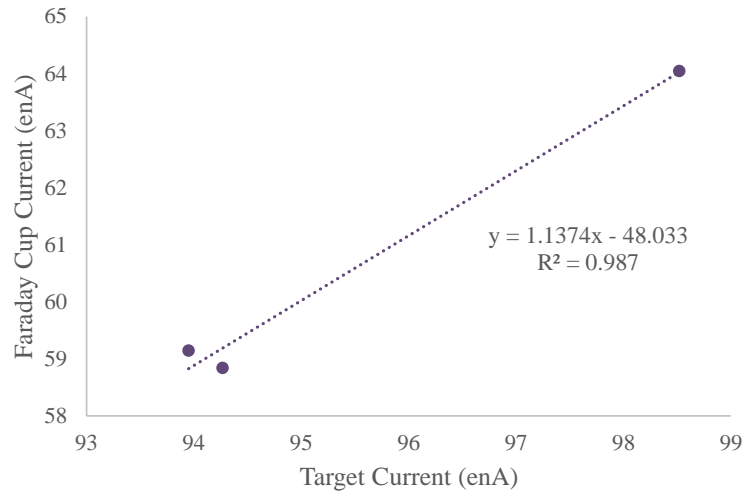


Figure 4.1: The result of the linear relationship between the current measured on the unsuppressed target and that measured on the more accurate Faraday cup. This was used to scale the target current measurements.

The beam was also intercepted multiple times in order to collect water samples during the irradiation as well and the time structure is shown in Figure 4.2

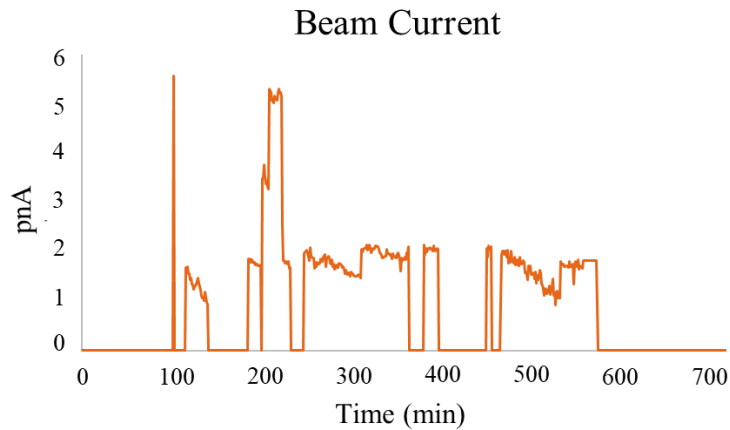


Figure 4.2: The observed beam current time structure during the irradiation. The average beam current was 1.9 pA.

Using the second iteration of the water system (Section 2.2.2) , the conditions of the water and gas line were monitored, specifically the dissolved oxygen content in the aqueous

phase, the conductivity of the water, the vary flow rates of each loop, the flow rate of the gas line, and the percentage of H₂ radiolytically produced in the gas stream.

The components in the gas line included a mass flow controller (Omega FMA5512A 0-500 mL/min Mass Flow Controller) to set the helium purge-gas stream to a constant flow rate of 135 mL/min, two gas traps to remove any unwanted gases from the stream (boric acid and soda lime), three cold gas traps placed in dewars to collect the desired ^{76/77}Kr isotopes (one molecular sieve trap and two stainless-steel traps), two cannisters of desiccant to remove water vapor from the gas stream, and finally a hydrogen analyzer (Hy-Optima 700B Series In-Line Hydrogen Process Analyzer).

4.2.2 ^{76,77}Kr Quantification and Qualification

Real-time gamma-ray measurements were taken to measure the distribution of activity through the harvesting system and gas line using a PHDS Nuclear Physics Imager (NPI) (PHDS Inc., Knoxville TN, USA). The NPI detector was placed approximately 1.7 m away from the aqueous and gas chemistry boxes behind three five-gallon water-filled carboys for shielding from the neutron flux in the room. During periods of time when the beam was intercepted by the Faraday cup, gamma spectra were collected using a pinhole collimator. Gamma spectra could not be collected while beam was interacting with the target due to the high level of neutron radiation interacting with the detector.

After the irradiation, the data collected was analyzed using the Imager 32 Software (PHDS Inc.) to determine the photopeak count rates after dead-time correction. These count rates were averaged over three regions of interest (ROIs) – the water tank and headspace, the cold traps in the gas line, and a background region between the aqueous chemistry and gas chemistry boxes. These regions are shown in figure 4.3a and b along with a photograph of the experimental

harvesting system set up and a heat map of the pinhole collimated intensity of 129 keV gamma rays.

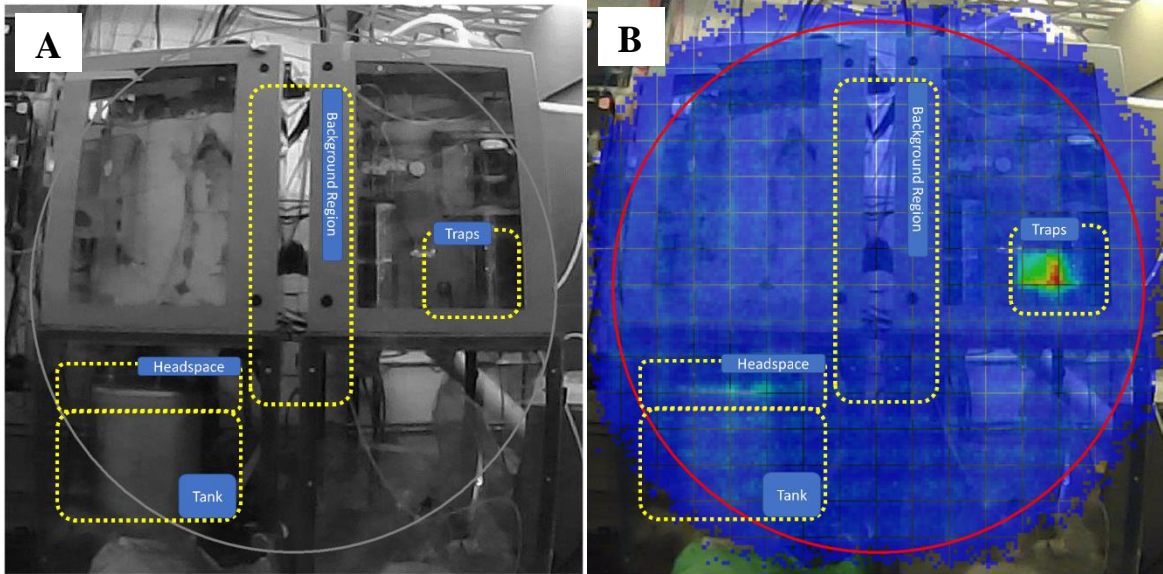


Figure 4.3: Example of the images collected with the NPI detector of the (a) experimental set up and a (b) heat map of the radiation produced and collected in the system. The ROIs selected to determine counts of activity in the headspace and the tank, the traps, and background measurements are depicted by the yellow boxes.

In order to model the mass transport of $^{76/77}\text{Kr}$ through the tank headspace and gas line of the harvesting system, a series of first order differential equations were used coupled with the gamma measurements collected by the NPI detector. The model was based upon parameters including the beam current measurements over time, the rate constant of equilibration of $^{76/77}\text{Kr}$ between the water and the gas phases, the flow rate of sparged gas from the tank headspace to through the gas line, and the production and decay of $^{76/77}\text{Kr}$ isotopes during the irradiation period.

To model the total activity of $^{76/77}\text{Kr}$ gas in the entire harvesting system, the following differential equation was used (Equation 4.1):

$$dA_{total} = dt [c_1 I(t) - \lambda A_{total}] \quad (\text{Equation 4.1})$$

where A_{total} is the total activity of $^{76/77}\text{Kr}$ at a given time, t ; c_I is a production factor which represents the production rate of the $^{76/77}\text{Kr}$ isotopes per incoming ^{78}Kr particle; $I(t)$ is the beam current at a given time, t ; and λ is the decay constant of the respective $^{76/77}\text{Kr}$ isotope.

The total activity within the entire harvesting system was then separated into the smaller regions of the system, including the tank (A_{tank}), the headspace of the tank (A_{head}), the cold traps (A_{trap}), and the gas collection bags (A_{bag}). Conservation of mass was followed through the use of Equation 4.2 and the differential Equation 4.3:

$$A_{total} = A_{tank} + A_{head} + A_{trap} + A_{bag} \quad (\text{Equation 4.2})$$

$$dA_{total} = dA_{tank} + dA_{head} + dA_{trap} + dA_{bag} \quad (\text{Equation 4.3})$$

For the purposes of this model, A_{tank} included not only the activity in the water tank, but also the activity produced in the target and traveling through the tubes between the target and water tank. The flow of the water traveling through this loop was rapid at a rate of 10 L/min. The activity of $^{76/77}\text{Kr}$ within the tank at any given time is described by the differential Equation 4.4:

$$dA_{tank} = dt [c_I I(t) - \lambda A_{tank} - k_1 A_{tank} + k_2 A_{head}] \quad (\text{Equation 4.4})$$

where the exchange kinetics of the dissolved gases in the aqueous phase and the gas phase are represented by k_1 and k_2 , respectively, and were fixed based upon Henry's law coefficient, k_H . This exchange rate was also dependent upon the volume of the water inside the tank, V_{tank} , the volume in the headspace of the tank, V_{head} , the temperature, T , and the ideal gas constant, R , using the following Equation 4.5:

$$k_2 = k_1 k_H \frac{V_{tank}}{V_{head}} RT \quad (\text{Equation 4.5})$$

The activity of $^{76/77}\text{Kr}$ in the headspace at any given time can be described in a similar manner, including the same exchange rate of gas between the liquid and gas phases, but adding

the additional term of the gas flow rate, f , of the $^{76/77}\text{Kr}$ as it was sparged from the water and through the gas line as seen in Equation 4.6.

$$dA_{head} = dt \left[-\lambda A_{head} + k_1 A_{tank} - k_2 A_{head} - \frac{f}{v_{head}} A_{head} \right] \quad (\text{Equation 4.6})$$

A similar differential equation was used to describe the activity of $^{76/77}\text{Kr}$ in the cold traps at any given time. The additional term in Equation 4.7, δ , represented the fractional trap inefficiency per unit time which accounted for any amount of activity that transferred out of the traps and into the gas collection bags at the end (Equation 4.8).

$$dA_{trap} = dt \left[-\lambda A_{trap} + \frac{f}{v_{head}} A_{head} - \delta A_{trap} \right] \quad (\text{Equation 4.7})$$

$$dA_{bag} = dt \left[-\lambda A_{bag} + \delta A_{trap} \right] \quad (\text{Equation 4.8})$$

A box diagram shown in Figure 4.4 represents the mass transport model broken down by each region of the harvesting system.

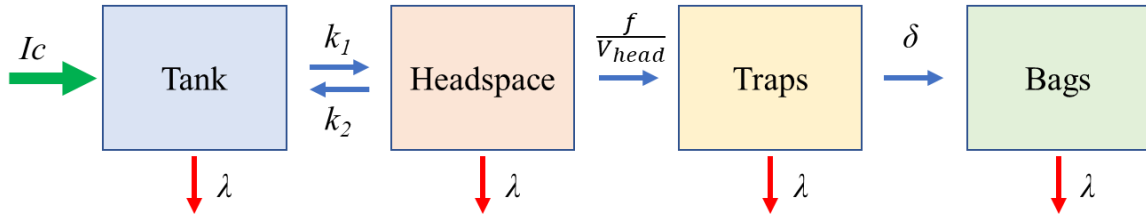


Figure 4.4: Box diagram representing the mass transport model of krypton gas as it travelled through the system and gas line.

The NPI data ($\bar{A}_{tank+head}$ and \bar{A}_{trap}) and the activity measurements obtained with the BEGe detector were used to fit, through chi-squared minimization, the constants c_1 , k_1 , δ and separate scaling constants for the tank-plus-headspace ROI, α_1 , and the cold trap ROI, α_2 , that accounted for the differing gamma-ray attenuation between the ROIs in the NPI detector.

The fit equations are described by Equations 4.9 and 4.10:

$$\bar{A}_{tank+head} = \frac{\alpha_1}{t_{off}-t_{on}} \int_{t_{on}}^{t_{off}} [A_{tank} + A_{head}] dt \quad (\text{Equation 4.9})$$

$$\bar{A}_{trap} = \frac{\alpha_2}{t_{off}-t_{on}} \int_{t_{on}}^{t_{off}} A_{trap} dt \quad (\text{Equation 4.10})$$

4.2.3 Online Collection of $^{76,77}\text{Kr}$

During the second iteration of the harvesting system as described in Section 2.2.2, ^{76}Kr and ^{77}Kr were trapped on the cold stainless-steel traps and cold molecular sieve trap. The trapped $^{76/77}\text{Kr}$ gas remained on the traps following the end of the irradiation until after the traps were safely removed from the system. This process was facilitated by quick-release fittings (Colder NS4 series couplings, 1/4" NPT) that were inserted between each trap to be removed (boric acid trap, soda lime trap, cold molecular sieve trap, two cold stainless-steel traps). For additional security of containment, each cold trap contained Swagelock turn valves (316 stainless-steel sealed valve, 1/4" Swagelock tube fittings), which were closed before unhooking the quick-release valves.

Following irradiation and gas collection, the boric acid and soda lime traps, the three cold gas traps, and the two air-tight gas collection bags were removed and analyzed using a Canberra Broad Energy Ge Gamma-ray Detector (BE2022) in order to identify and quantify the radionuclides collected on each trap. The measurements were taken approximately 2 hours after the end of the irradiation.

Calibration of the gamma-ray detector was performed using a ^{152}Eu source at 25 cm and 50 cm from the face of the detector. Additional calibrations were made by placing the ^{152}Eu source inside one of the cold-trap Dewars to account for attenuation through the Dewar walls. The Genie 2000 Software (Mirion Technologies) was used to analyze the data.

4.2.4 Generation of $^{76,77}\text{Br}$ from $^{76,77}\text{Kr}$

After the cold traps were removed from the gas line and the gamma measurements were taken to demonstrate the amount of $^{76,77}\text{Kr}$ activity which was collected during the irradiation, an offline experimental set-up was created in order to test the generation of $^{76,77}\text{Br}$ from $^{76,77}\text{Kr}$. The offline set-up connected the two traps using quick-release valves and Swagelock turn valves with polypropylene tubing. After the traps were connected, the collected gases could be transferred cryogenically from the initial trap to the receiving trap. A schematic of this process is shown in Figure 4.5.

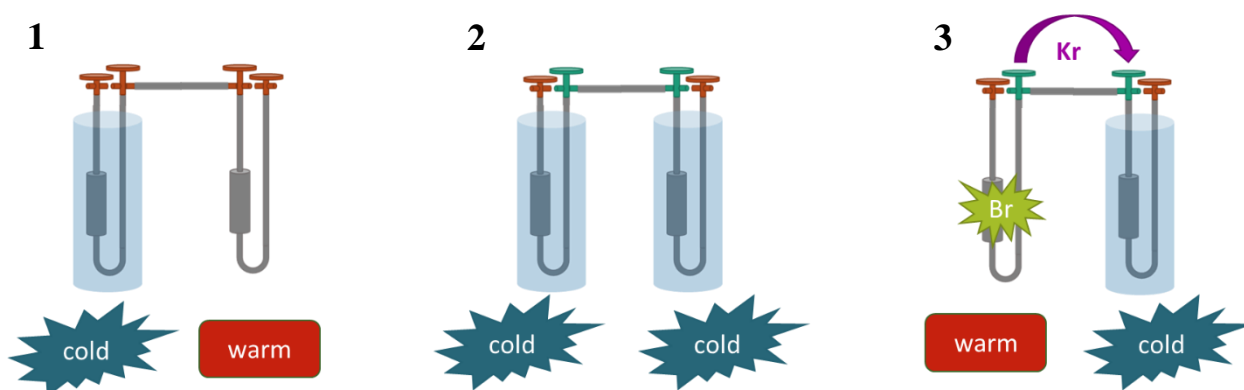


Figure 4.5: 1) The initial trap is cold, and the receiving trap is warm. 2) Both traps are cold and the valves between them are opened to allow gas transfer. 3) The initial trap is warmed, forcing gas into the receiving trap. In this process, the daughter $^{76,77}\text{Br}$ isotopes would remain in the initial trap and the parent $^{76,77}\text{Kr}$ isotopes would transfer to the receiving trap.

The transfer of the collected gases was done using a series of steps starting with the connection of the initial trap (cold) in a liquid nitrogen Dewar and receiving trap (room temperature) with all valves closed. The second step involved inserting the receiving trap into a liquid nitrogen Dewar to begin cooling the trap to the same temperature as the initial trap. During the third step, the two inner turn valves connecting the traps together were opened to allow the passage of gas flow from one trap to the other. The final step involved the removal of the initial

trap from the liquid nitrogen Dewar to warm it up to room temperature. The heating of the original trap caused the gas molecules to move faster; therefore, expanding the volume and increasing the pressure inside the trap. This increase in pressure forced the gas to travel to the receiving trap of much lower temperature, where the gas volume and pressure inside the trap decreased. Since the ^{76}Kr and ^{77}Kr gas decay into ^{76}Br and ^{77}Br in a solid form, respectively, only the gas transferred from one trap to another. The bromine was left behind in the initial trap at room temperature.

This transfer process was performed three times (Figure 4.6). Transfer 1 was performed immediately following the gamma spectroscopy measurements were taken in order to combine all of the collected $^{76/77}\text{Kr}$ gas from the molecular sieve trap and the first stainless-steel trap (trap 1) in the gas line onto the second stainless-steel trap (trap 2) in the gas line. After allowing approximately 6 hours of residence time in trap 2 for the $^{76/77}\text{Kr}$ parent isotopes to decay into the $^{76/77}\text{Br}$ daughter isotopes, transfer 2 was done. In this transfer, the gaseous isotopes in trap 2 were transferred into a new stainless-steel trap (trap 3). At the time of the transfer, all captured ^{77}Kr had decayed, leaving only ^{76}Kr as a parent in trap 3. Finally, transfer 3 was performed approximately 28 hours later to allow for the majority of the trapped ^{76}Kr to decay into the desired ^{76}Br . The small amount of leftover ^{76}Kr was transferred out of trap 3 into a discard trap. In all transfers, the $^{76/77}\text{Br}$ isotopes did not move, leaving traps 1 and 2 with mixed samples of ^{76}Br and ^{77}Br , while trap 3 contained purified ^{76}Br (Figure 4.6).

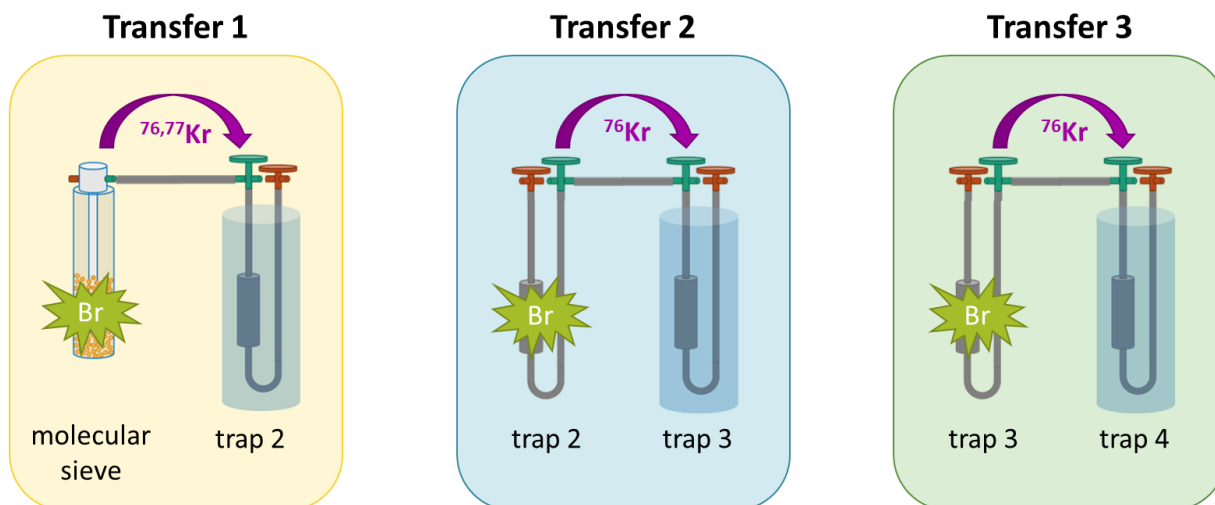


Figure 4.6: Schematic of the three transfers which were performed in order to generate and isolate ^{76}Br from ^{77}Br .

4.2.5 Radioactive Bromine Elutions

In order to access the $^{76/77}\text{Br}$ which remained behind in the stainless-steel traps after transferring the gases, an experimental protocol was used in which each trap was rinsed through with water and the eluent was collected into individual sample vials. The setup involved removing the quick-release and Swagelok turn valves from the inlet and outlet of each trap. The valves on the inlet of the traps were replaced with syringes to dispense known volumes of water through the trap for collection at the end. A schematic of this set up is demonstrated in Figure 4.7.

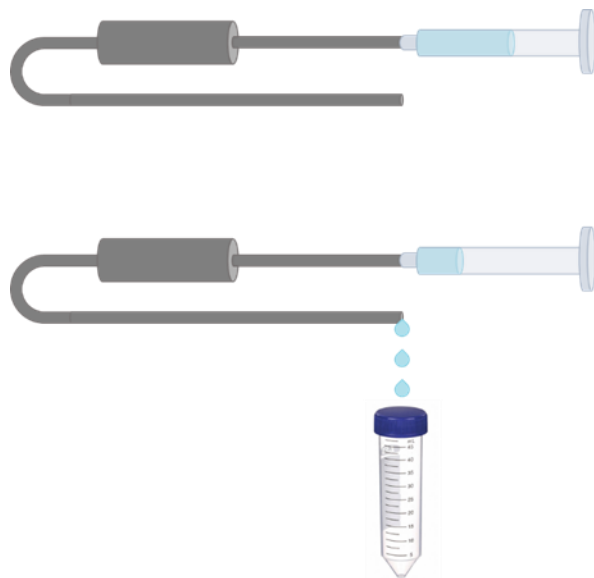


Figure 4.7: Example of the elution wash process of attaching a syringe of water to each trap and passing varying amounts of water through to a collection vessel.

The amount of $^{76/77}\text{Br}$ activity in each trap was again quantified using gamma spectroscopic measurements that were taken of trap 1, 2, and 3 before and after the elution rinses. The percentage of the total $^{76/77}\text{Br}$ activity that was removed from each trap was calculated. The volumes of water used for each rinse of each trap can be found in Table 4.1. For traps 1 and 2, two elution rinses were used. For trap 3, three elution rinses were used all of varying volumes.

Table 4.1: Volumes of water used to elute $^{76/77}\text{Br}$ isotopes from traps 1, 2, and 3.

Trap Name	Elution 1 Volume (mL)	Elution 2 Volume (mL)	Elution 3 Volume (mL)
trap 1	17	10	--
trap 2	10	10	--
trap 3	7	4	10

4.3 Results and Discussion

4.3.1 ^{78}Kr Irradiation

During the irradiation, the percent of hydrogen in the gas stream flowing through the gas line was measured and the results are shown with respect to the beam current in Figure 4.8. The maximum percentage of hydrogen measured was 0.92% over the course of the experiment, with the average being 0.40%, well below the explosive limit. Based upon the average LET during this irradiation in comparison to the G-values from the literature described in Chapter 3, the predicted G-value of hydrogen was 1.37 molecules of $\text{H}_2/100\text{ eV}$.¹⁰⁻¹⁴ The experimental *apparent* G-value was calculated to be 1.06 molecules of $\text{H}_2/100\text{ eV}$, which was closer to but once again lower than the predicted value.

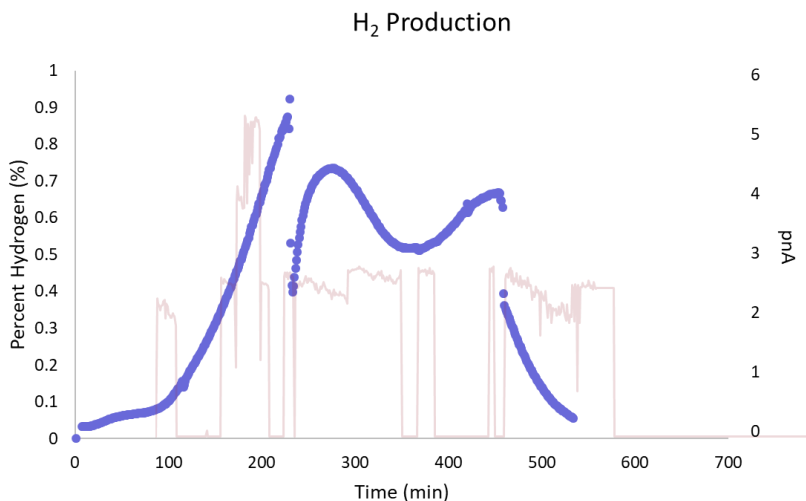


Figure 4.8: The hydrogen measurements during ^{78}Kr irradiation (blue points) compared to the corrected beam current time structure (red histogram).

4.3.2 ^{76,77}Kr Quantification and Qualification

Using the NPI detector, 13 gamma-ray measurements were made while the beam was intercepted by the target during the irradiation. These measurements were taken from certain regions of the water system – the tank and headspace region as well as the traps region. The results and uncertainties of the measurements are depicted by the orange data points in Figures 4.9a and 4.9b as well as in Table 4.2.

Table 4.2: Activity calculated from the real-time gamma measurement results from the NPI detector. These activities were used to fit the mass transport model.

Time Scale (s)	Tank + Headspace Activity (MBq)	Tank + Headspace Uncertainty	Trap Activity (MBq)	Trap Uncertainty
0	16.6	2.4	5.7	0.6
5407	79.9	5.6	15.4	0.8
5578	74.0	3.0	15.7	0.5
20204	69.4	5.7	32.9	1.8
21287	60.3	2.8	30.8	1.7
22155	57.2	4.7	28.5	0.3
22791	51.6	4.4	29.1	0.7

The mass transport model was fit to the data collected by the NPI and the resulting rate constant for the sparging of ⁷⁷Kr gas (k_I) was determined to be $4.1(4) \times 10^{-5}$ Hz. The inefficiency of collection on the traps (δ) was zero with an uncertainty of 4×10^{-8} Hz. By comparing the predicted mass transport to the NPI measurements of the whole system during irradiation with the BEGe gamma-ray spectra collected of the components in the gas line post-irradiation, the production rates of ^{76/77}Kr were found to be $2.7(1) \times 10^{-4}$ nuclei of ⁷⁶Kr produced per incident ⁷⁸Kr ion and $1.18(6) \times 10^{-2}$ nuclei of ⁷⁷Kr produced per incident ⁷⁸Kr ion.

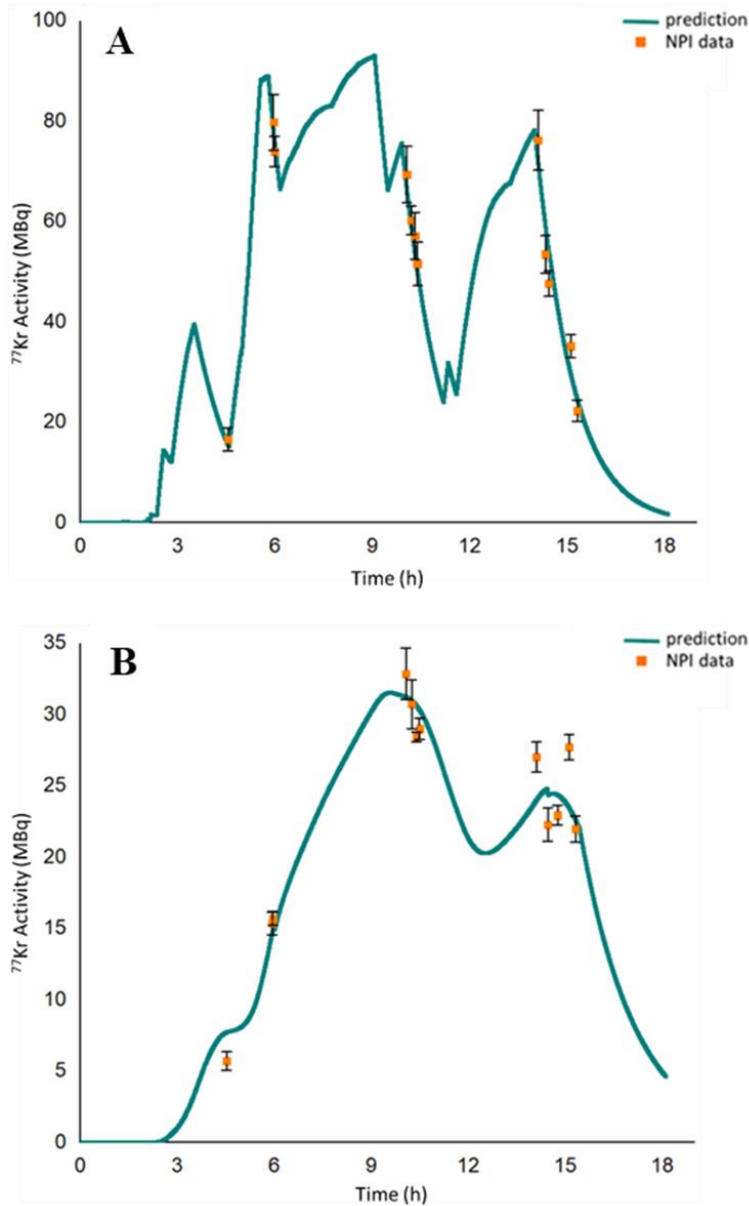


Figure 4.9: The mass transport of ^{77}Kr was predicted (blue line) for different locations within the harvesting system – (a) the water and the headspace in the tank and (b) the traps. Real time data of the ^{77}Kr activity calculated from the gamma spectra from the NPI detector are shown (orange points) for comparison to the predictions.

The time structure that is evident in Figures 4.9a and 4.9b resulted from the periods of beam-on-target and beam intercepted. The data collected with the NPI detector followed the same time structure as the activity decreased during periods where the beam was off. This was

important for the determination of the production rates of $^{76/77}\text{Kr}$. The determination of the mass transport model was only successful for ^{77}Kr using the NPI data as only the 129 keV gamma ray emission was clearly visible without any overlap. Using the information determined about ^{77}Kr , the mass transport model for ^{76}Kr was predicted and the time structure is demonstrated in Figure 4.10.

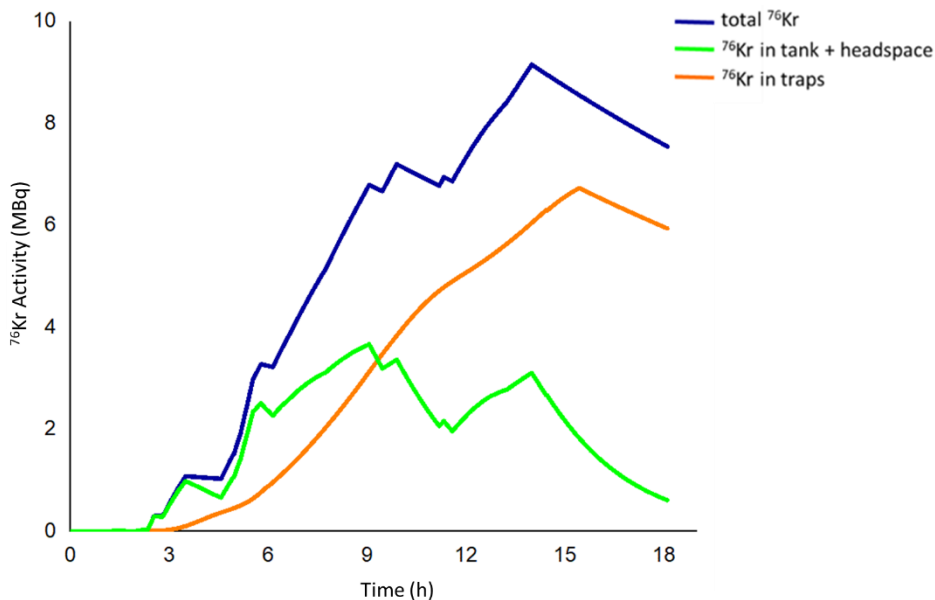


Figure 4.10: The predicted mass transport of ^{76}Kr for different locations within the harvesting system – (blue) the total ^{76}Kr , (orange) the ^{76}Kr in the tank and the headspace of the tank, (green) the ^{76}Kr in collected on the traps.

To measure the activity of $^{76/77}\text{Kr}$ collected on the traps, they were removed from the system and analyzed with gamma spectroscopy. A total of 7.2(1) MBq of ^{76}Kr and 19.1(6) MBq of ^{77}Kr were trapped in the online collection system as shown in Table 2. The table demonstrates how much activity was contained in each trap, with the molecular sieves trapping the most gas.

Table 4.3: Production and the location of online collection results of ^{76}Kr and ^{77}Kr *

Trap Name	Activity of ^{76}Kr (MBq)	Activity of ^{77}Kr (MBq)
Trap 1	0.089(5)	0.48(2)
Trap 2	0.51(1)	2.05(8)
Molecular Sieve Trap	6.6(1)	16.6(6)
Total Activity	7.2(1)	19.1(6)

*All activity was measured after the irradiation at approximately 16 hours in relationship to the plots in Figures 6 and 7

4.3.3 Generation of $^{76,77}\text{Br}$ from $^{76,77}\text{Kr}$

^{76}Br was isolated from ^{77}Kr , ^{76}Kr , and ^{77}Br through a series of transfers. The first transfer, which involved combining the gaseous krypton isotopes that were collected online during irradiation, is qualitatively demonstrated with the BEGe gamma-ray spectra, shown in Figure 4.11. A small portion of the $^{76/77}\text{Kr}$ gas remained in the molecular sieve trap after the transfer, but overall, 0.99(1) MBq of ^{76}Kr and 3.8(2) MBq of ^{77}Kr were transferred onto trap 2.

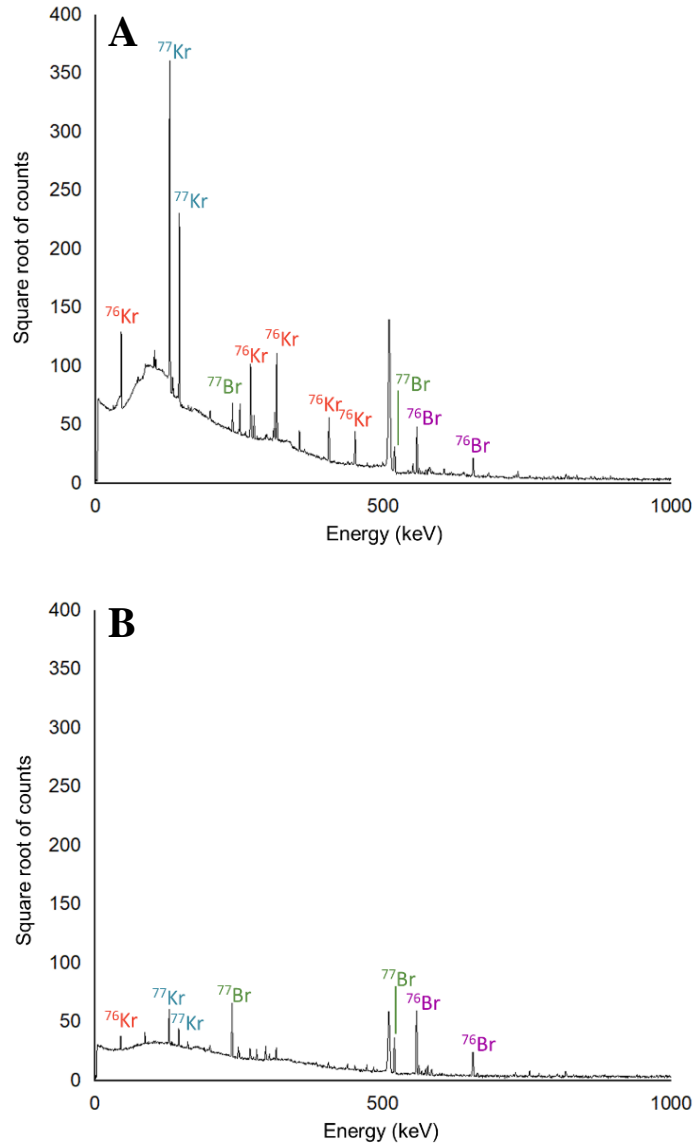


Figure 4.11: Example gamma-ray spectra (count time = 300 s) of stainless-steel trap 2 before (a) and after (b) the transfer of krypton gas to stainless steel trap 3. The successful movement of krypton gas due to changes in temperature is demonstrated by the decrease in counts of activity of ^{76}Kr and ^{77}Kr .

Following the accumulation of all gaseous activity onto trap 2, the $^{76/77}\text{Kr}$ isotopes were left to decay for approximately 7 hours. Then the activity of trap 2 was re-measured to demonstrate that ^{76}Kr was the main krypton isotope left in the trap. The gamma measurement results can be seen in Figure 4.12. The activity of ^{77}Kr had decreased significantly from 3.8 MBq

to 0.03 MBq, making it possible to generate ^{76}Br in a new trap without ^{77}Br as a contaminant.

The transfer from stainless steel trap 2 to stainless steel trap 3 resulted in some ^{76}Kr remaining in trap 2 along with ^{76}Br and ^{77}Br (Figure 4.12).

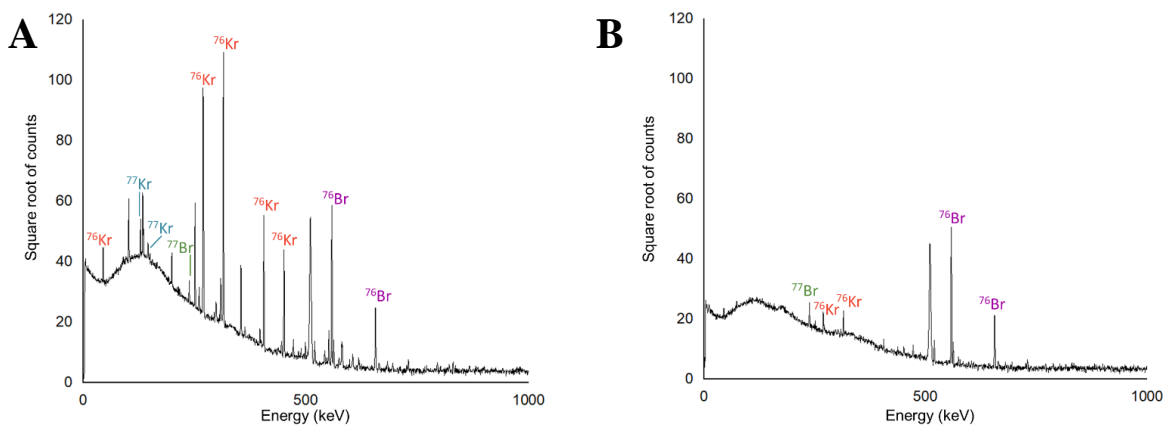


Figure 4.12: Example gamma-ray spectra (count time = 300 s) of stainless steel trap 3 before (a) and after (b) the transfer of ^{76}Kr gas to stainless steel trap 4. The successful movement of krypton gas due to changes in temperature is demonstrated by the lack of counts of activity of ^{76}Kr .

The final transfer from stainless steel trap 3 to stainless steel trap 4 left pure ^{76}Br remaining in trap 3 and removed the excess ^{76}Kr gas, which is demonstrated by the absence of contaminating gamma rays in the gamma spectrum in Figure 4.13. Through the transfer process, it was demonstrated that ^{76}Br could be generated and isolated from ^{77}Br due to the differences in half-lives of the parent isotopes. The radionuclidic purity of the ^{76}Br was 99.9%.

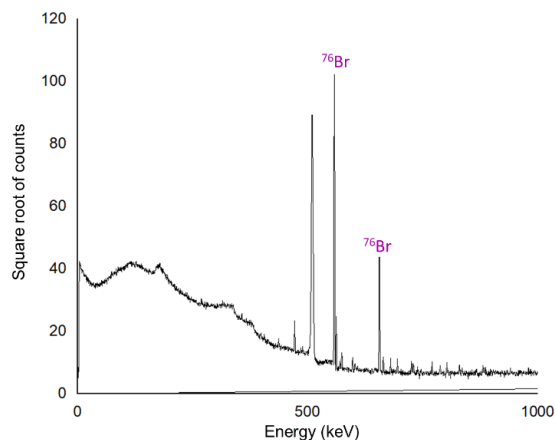


Figure 4.13: Gamma-ray spectrum (count time = 300 s) of stainless steel trap 3 after the transfer of ^{76}Kr gas to stainless steel trap 4. The successful movement of krypton gas due to changes in temperature is demonstrated by the lack of counts of activity of ^{76}Kr . The isolation of ^{76}Br is demonstrated.

4.3.4 Radioactive Bromine Elutions

Using the previously described elution procedure, the bromine remaining in each trap after the transfer of krypton, was eluted using different volumes of water. Performing quantitative gamma spectrometry measurements before the rinsing steps and of each eluent vial, the efficiencies of the procedure were determined. An example of the differences in gamma spectrometry measurements before, during, and after the rinsing procedure can be seen in Figure 4.14.

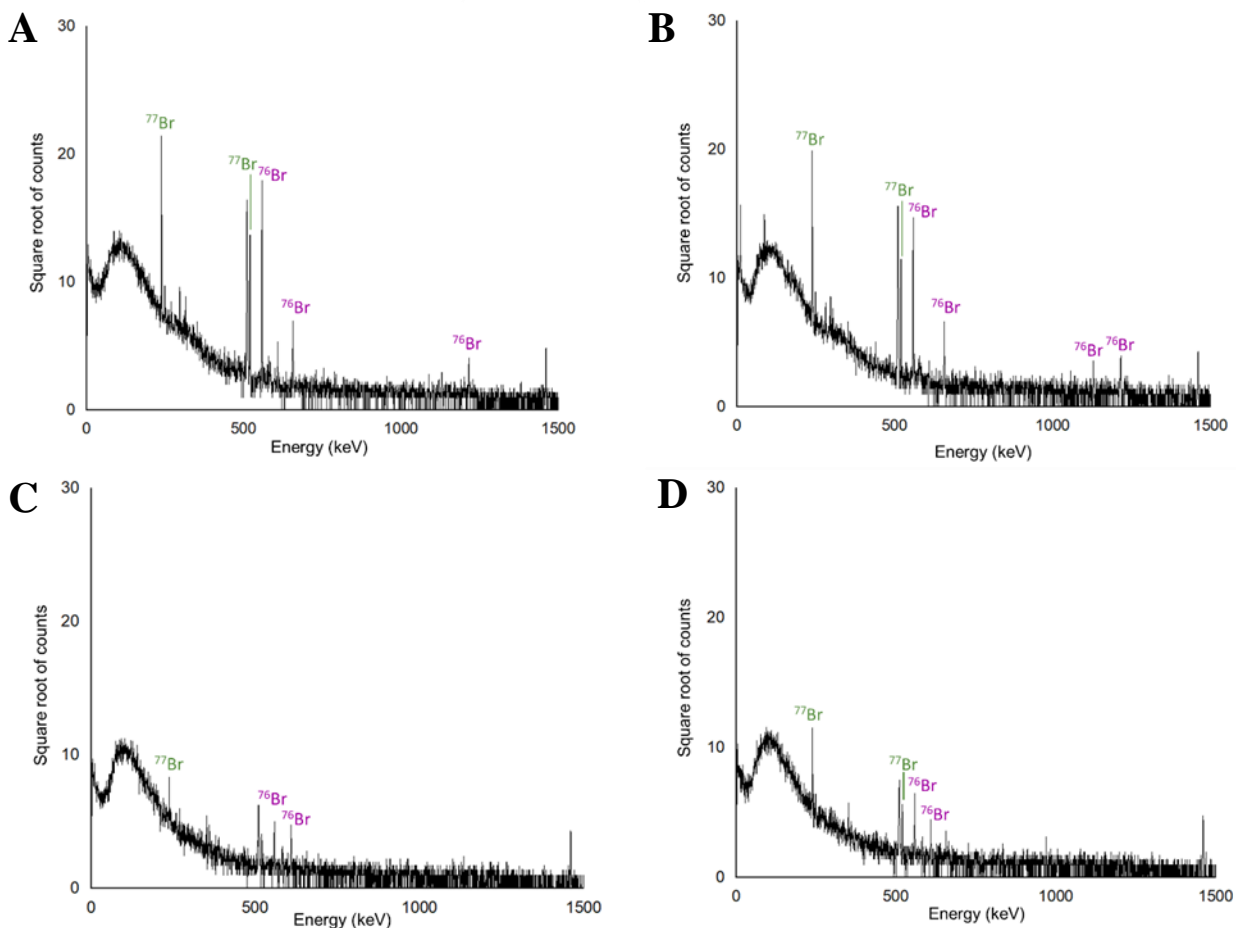


Figure 4.14: Example gamma-ray spectra (count time = 300 s) of trap 1 before elution (a), the eluent from rinse 1 (b), the eluent from rinse 2 (c), and the trap after washing (d).

The rinsing procedure of trap 1, which was directly removed from the online set up with no generator transfers, consisted of two separate elutions with 17 mL and 10 mL water, respectively. This trap contained a mixture of $^{76/77}\text{Br}$ radioisotopes. This was the first trial of the rinsing procedure; therefore, a larger volume of water was used to test the ability to remove the $^{76/77}\text{Br}$ from the trap with water. In total, 89% of the $^{76/77}\text{Br}$ contained in the trap was eluted with the 27 mL of water. The rinsing of trap 2 was also performed with two rinsing steps; however, the volume of water used was reduced to 10 mL for each rinse. This trap also contained a mixture of $^{76/77}\text{Br}$ radioisotopes and a total of 79% was eluted with the 20 mL of water. And

finally, the rinsing procedure of trap 3 consisted of three separate rinses with 7 mL, 4 mL, and 10 mL of water, respectively. In this rinsing trial, only ^{76}Br was present in the trap to be removed, and the elution efficiency was 64%.

The elution efficiency of $^{76/77}\text{Br}$ decreased with decreasing total volume (Table 4.4) and had the lowest efficiency in the trial using a greater number of small volume washes. While it is important to use small volumes of water for eventually using the eluted bromine in radiolabeling procedures, it is also important to obtain as much bromine from the traps as possible to increase overall production yields using this method.

Table 4:4: Total bromine activity measurements (kBq) resulting from elution rinses

	Pre-elution	Elution 1	Elution 2	Elution 3	Total	Efficiency (%)
Trap 1	37.0 (1.5)	29.6 (0.7)	3.3 (0.4)	--	32.9 (1.9)	89.0
Trap 2	269.7 (6.7)	180.6 (4.1)	32.6 (0.7)	--	213.1 (7.8)	79.0
Trap 3	361.9 (7.8)	170.2 (4.4)	42.2 (1.5)	18.5 (0.7)	230.9 (9.3)	63.8

4.4 Conclusions

The irradiation of the second iteration of the beam blocker and water system with a 150 MeV/nucleon ^{78}Kr beam at an average beam current of 1.9 pA for approximately 11 hours facilitated the successful collection of 7.2(1) MBq of ^{76}Kr and 19.1(6) MBq of ^{77}Kr in the new gas collection line. This irradiation experiment demonstrated the ability of the developed harvesting system to collect radionuclides of interest simultaneously from the aqueous and gas phases. This experiment also demonstrated the potential of this production method for the generation of $^{76/77}\text{Br}$ from $^{76/77}\text{Kr}$ harvesting.

The real-time gamma spectroscopic measurements that were possible utilizing the NPI detector from PHDS generated maps of the $^{76/77}\text{Kr}$ distribution as it flowed through the system and was collected on the cold traps. This data collected in real-time made it possible to predict

and model the mass transport of both ^{76}Kr and ^{77}Kr through the system based upon their production rates in the tank water, Henry's law for the sparging of krypton into the gas phase, the flow rate of gas from the headspace to the traps for collection, and the decay of the $^{76/77}\text{Kr}$ isotopes over the irradiation time. From this, the production rates of ^{76}Kr and ^{77}Kr were determined to be $2.7(1) \times 10^{-4}$ nuclei of ^{76}Kr and $1.18(6) \times 10^{-2}$ nuclei of ^{77}Kr formed per incident ^{78}Kr ion. Looking forward to higher intensity irradiations at FRIB, it will be very beneficial to have the mass transport model of $^{76/77}\text{Kr}$ through this system to apply the model to higher production rates.

After the online collection of radioactive $^{76/77}\text{Kr}$ gas, utilizing differences in temperature, the gas was transferred between different collection traps to generate samples of the daughter bromine isotopes. This $^{76}\text{Kr}/^{76}\text{Br}$ and $^{77}\text{Kr}/^{77}\text{Br}$ generator concept proved successful with the isolation of ^{76}Br from ^{77}Br . The ^{76}Br and ^{77}Br products were eluted from the vessels using water rinses with an average efficiency of $77 \pm 12\%$. Radionuclidically pure elutions of ^{76}Br were obtained by a separation based on different half-lives of mother/daughter radionuclides.

The information gathered from this experiment about the transport of gases through the system, the efficiency of gas collection, and the production rate of hydrogen can be used to improve the system in preparation for FRIB gas-phase harvesting experiments in the future. Furthermore, with extension to other noble gases, the Kr/Br work presented here has implications for future gas-phase harvesting at FRIB to create generators like $^{122}\text{Xe}/^{122}\text{I}$ or $^{211}\text{Rn}/^{211}\text{At}$.¹⁵

APPENDIX

THEORY OF INSTRUMENTATION UTILIZED IN CHAPTER 4

PHDS Nuclear Physics Imager

During the irradiation, a PHDS Germanium Gamma-ray Imager (GeGI) was used to measure the real-time distribution of activity through the harvesting system. This portable, handheld detector has the capability to detect, identify, and quantify radioactivity, using high-resolution spectroscopy and imaging techniques.¹⁶ With the ability to generate both Compton and pinhole images, a map of radiation is produced and gamma spectroscopy from specific areas on the map can be generated. During this experiment, GeGI the pinhole images were used to detect, identify, locate, and quantify ⁷⁷Kr. The pinhole imaging energy range is approximately 40 keV to 662 keV, with high contrast and spatial resolution of approximately 1°.

REFERENCES

REFERENCES

- 1) Abel, E. P.; Clause, H. K.; Severin, G. W. Radiolysis and Radionuclide Production in a Flowing-Water Target during Fast $^{40}\text{Ca}^{20+}$ Irradiation. *Appl. Radiat. Isot.* **2020**, *158* (January), 109049.
- 2) Gade, A.; Sherrill, B. M. NSCL and FRIB at Michigan State University: Nuclear Science at the Limits of Stability. *Phys. Scr.* **2016**, *91* (5), 053003
- 3) Avilov, M.; Aaron, A.; Amroussia, A.; Bergez, W.; Boehlert, C.; Burgess, T.; Carroll, A.; Colin, C.; Durantel, F.; Ferrante, P.; Fourmeau T.; Graves, V.; Grygiel, C.; Kramer, J.; Mittig, W.; Monnet, I.; Patel, H.; Pellemoine F.; Ronningen R.; Schein, M. Thermal, Mechanical, and Fluid Flow Aspects of the High Power Beam Dump for FRIB. *Nuclear Instruments and Methods in Physics Research Section B. Interactions with Materials and Atoms.* **2016**, *376*, 24-27.
- 4) Domnanich, K. A.; Abel, E. P.; Clause, H. K.; Kalman, C.; Walker, W.; Severin, G. W. An Isotope Harvesting Beam Blocker for the National Superconducting Cyclotron Laboratory. *Nucl. Instruments Methods Phys. Res. Sect. A Accel. Spectrometers, Detect. Assoc. Equip.* **2020**, *959* (November 2019), 163526.
- 5) Domnanich, K. A.; Vyas, C. K.; Abel, E. P.; Kalman, C.; Walker, W.; Severin, G. W. Harvesting ^{62}Zn from an Aqueous Cocktail at the NSCL. *New J. Chem.* **2020**, *44*, 20861 – 20870.
- 6) Mason, N. S.; Mathis, C. A. Radiohalogens for PET Imaging. In *Positron Emission Tomography: Basic Science and Clinical Practice*; Valk, P. E.; Bailey, D. L.; Townsend, D. W.; Maisy, M. N. Springer-Verlag: London 2003; 217-236.
- 7) Glaser, M.; Luthra, S. K.; Brady, F. Applications of positron-emitting halogens in PET oncology (Review). *Int. J. Oncol.* **2003**, *22*, 253 – 267.
- 8) Stepanek, J.; Larsson, B.; Weinreich, R. Auger-Electron Spectra of Radionuclides for Therapy and Diagnostics. *Acta Oncologica.* **1996**, *35* (7), 863 – 868.
- 9) Singh, B. Nuclear Data Sheets Update for A=76. *Nuclear Data Sheets.* **1995**, *74*, 63.
- 10) Singh, B.; Nica, N. Nuclear Data Sheets for A=77. *Nuclear Data Sheets.* **2012**, *113*, 1115 – 1314.
- 11) Meesungnoen, J.; Jay-Gerin, J. P. High-LET radiolysis of liquid water with $^1\text{H}^+$, $^4\text{He}^{2+}$, $^{12}\text{C}^{6+}$, and $^{20}\text{Ne}^{9+}$ ions: effects of multiple ionization. *Journal of Physical Chemistry,* **2005**, *109*

- 12) Bibler, N. E. Radiolysis of 0.4 M sulfuric acid solutions with fission fragments from dissolved californium-252. Estimated yields of radical and molecular products that escape reactions in fission fragment tracks. *Journal of Physical Chemistry*, **1975**, *79*, 1991-1995.
- 13) LaVerne, J. A. Detection of gaseous products in the radiolysis of aqueous solutions. *Journal of Physical Chemistry*. **1988**, *92*, 2808-2809
- 14) LaVerne, J.A. Chapter 14: Radiation Chemical Effects of Heavy Ions In: *Charged Particle and Photon Interactions with Matter: Chemical, Physiochemical, and Biological Consequences with Applications*, **2003**, 403-430
- 15) Abel, E. P.; Avilov, M.; Ayres, V.; Birnbaum, E.; Bollen, G.; Bonito, G.; Bredeweg, T.; Clause, H.; Couture, A.; DeVore, J.; Dietrich, M.; Ellison, P.; Engle, J.; Ferrieri, R.; Fitzsimmons, J.; Friedman, M.; Georgobiani, D.; Graves, S.; Greene, J.; Lapi, S.; Loveless, C. S.; Mastren, T.; Martinez-Gomez, C.; McGuinness, S.; Mittig, W.; Morrissey, D.; Peaslee, G.; Pellemoine, F.; Robertson, J. D.; Scielzo, N.; Scott, M.; Severin, G.; Shaughnessy, D.; Shusterman, J.; Singh, J.; Stoyer, M.; Sutherlin, L.; Visser, A.; Wilkinson, J. Isotope Harvesting at FRIB: Additional Opportunities for Scientific Discovery. *J. Phys. G Nucl. Part. Phys.* **2019**, *46* (10), 100501
- 16) PHDS Gamma Ray Imaging Detectors. [Online] <https://phdsco.com/products/np-imager>. (Accessed 2021).

V. Improvements to the System in Preparation for Gas-Phase Harvesting at FRIB

5.1 Introduction

As discussed in Chapter 3, the ^{40}Ca irradiation provided data for analysis of the target material and a first test run of the water system. Testing of the water system revealed that some sensors should be replaced to optimize accurate data collection, the system should be completely closed to alleviate any re-equilibration with the atmosphere, and that the resins and gas traps used to collect radioisotopes in the aqueous and gaseous phases worked as expected. During this experiment, the rate of hydrogen production due to radiolysis was also studied. At a low average intensity of approximately 0.4 pA, the rate of hydrogen production was lower than expected; however, more testing is required to learn more about radiolysis (Figure 3.5 in Section 3.3.3).

The ^{78}Kr irradiation described in Chapter 4 tested the gas-phase harvesting capabilities of the harvesting system at a slightly increased intensity ranging from 0 – 4 pA over the course of 11 hours. The revised gas processing line successfully collected krypton gas online and most of the activity was collected on the molecular sieve cold trap. This trap was at the end of the three cold traps used in the experiment and the molecular sieves added a substantial amount of surface area for trapping purposes in comparison to the stainless-steel traps. During this experiment, the production of hydrogen was also measured, reaching a maximum of 0.92% H_2 in the gas stream (Figure 4.8 in Section 4.3.1), still below the expected value.

Following the ^{78}Kr experiment, a ^{48}Ca irradiation (140 MeV/nucleon, at the maximum available intensity at the NSCL) experiment was performed to test the system at higher intensities and to continue testing the aqueous-phase harvesting capabilities. There were two segments of varying beam currents – a 2-hour segment at 60 pA and a 7.7-hour segment at the

maximum 80 pA – for a total integrated beam current of 703 pA·h. The experiment also provided the opportunity to measure H₂ and O₂ production during a 12-hour irradiation with full beam power at the NSCL. Results of the production of H₂ and O₂ over time in comparison to the beam current are shown in Figure 5.1. The maximum amount of H₂ produced during the irradiation was 2.7% with an average of 1.6%. The maximum amount of O₂ produced in the gas stream was 1.5% with an average of 0.7%. It should be noted that the flow rate of gas in this experiment was higher than in previous experiments at approximately 1.4 L/min of Helium instead of 300 mL/min in order to dilute the concentrations of both H₂ and O₂ in the He carrier gas stream.

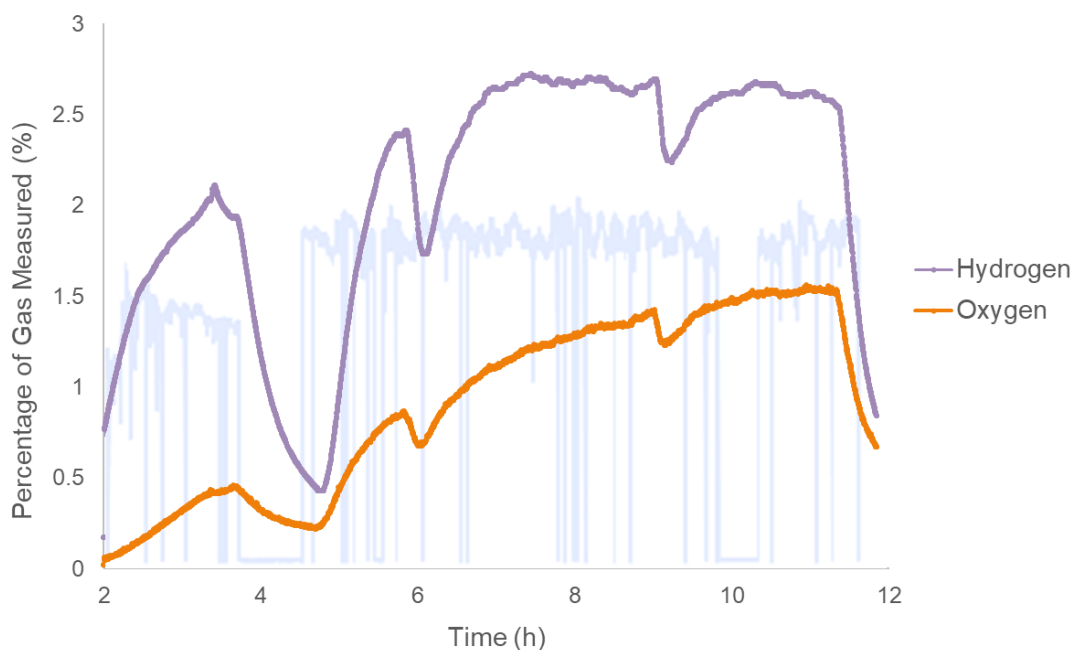


Figure 5.1: The measured percentages of hydrogen and oxygen during a ⁴⁸Ca high-intensity irradiation with the time structure of the beam current shown.

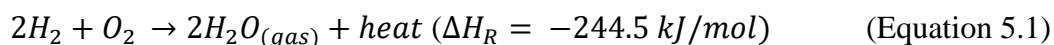
For safety of personnel and the laboratory environment, it is important to keep the concentrations of H₂ and O₂ well below the lower explosive limit. A hard limit was set to not exceed 2.5% O₂ and 6.5% H₂, which was met during this irradiation. However, a harvesting

experiment at FRIB using a higher intensity ^{78}Kr stable beam would have the potential to produce levels above these safety limits. Without determining a way to reduce the production of H_2 and O_2 in the system, the flow rate of carrier gas would need to increase to a level which would make it difficult to harvest gaseous radioisotopes in traps.

In this work, there was preliminary investigation into methods of improvement to optimize the gas processing line. One improvement involves the use of a catalyst to recombine the hydrogen and oxygen radiolytically produced to form water to ensure the concentrations are safely under the lower explosive limits without the need for increasing the gas flow rate. A second improvement to the gas line is the use of novel metal organic frameworks (MOFs) instead of cold traps to increase the collection efficiency of noble gases in the gas processing line.

5.2 Catalytic Recombination of Hydrogen and Oxygen

Using a catalyst, hydrogen and oxygen molecules will react at low temperatures (as low as 15°C) and low hydrogen concentration. One such catalyst is the OxiGone 130 Palladium Catalyst (Research Catalysts, Inc.) which consists of 2-4 mm aluminum oxide beads coated with 0.3% by weight palladium. The removal of hydrogen works best when there is an excess of oxygen available in the system and follows Equation 5.1 written below:



Stoichiometrically, twice as much hydrogen is consumed in order to recombine with oxygen and form water, leading to the removal of hydrogen from the system in the presence of excess oxygen.

A hydrogen recombiner made of the OxiGone catalyst or a similar catalyst from a different company is included in the proposed FRIB beam dump harvesting system. Therefore;

testing of the efficiency of recombination and optimization of gas flow conditions in a similar harvesting system is necessary before relying on the catalyst during an irradiation experiment.

5.2.1 Hydrogen Recombiner Testing Materials and Methods

To test the efficiency of hydrogen recombination via the OxiGone catalyst, a simple version of the harvesting system was created for cold testing purposes, which consisted of a water loop and a gas line (identified by the purple and blue arrows, respectively, in Figure 5.2). The water loop was made up of a water tank (Spike Brewing CF10 Conical Unitank, 14 gal, 304 SS, Kynar Coated) filled with approximately 10 gallons of water that was pumped at approximately 3 gallons per minute using a Grundfos CRNE 1-6 water pump. A flowmeter (Flowmeter Totalizer Product, 316 SS) was used to measure the flow of the water during experiments. The water loop also consisted of a column of OxiGone catalyst in the aqueous phase to breakdown H_2O_2 (700 mL volume) followed by a dissolved oxygen probe (Mettler-Toledo Ultra-Pure Water Polarographic ISM Dissolved Oxygen Probe) to measure the concentration of dissolved oxygen in the water after H_2O_2 degradation.

The gas line consisted of 3.460% H_2 in He carrier gas to represent the source of H_2 and the mixed gas was set to a given flow rate using mass flow controller (Sierra SmartTrak 100 0-20 SLPM Mass Flow Controller). A bed of the OxiGone 130 Palladium Catalyst was designed using an approximate catalyst volume of 280 mL. This volume consisted of 1104 g of Al_2O_3 and 3.3 g of Pd. The size of the beads ranged from 2-4 mm with a surface area of $90 \text{ m}^2/\text{g}$. On either side of the catalyst bed were two canisters filled with desiccant to remove water vapor for accurate oxygen and hydrogen concentration measurements as well as to collect all of the condensed water vapor which was produced from the catalytic reaction. Also on either side of the catalyst an oxygen and hydrogen sensor were used to measure the O_2 and H_2 concentrations in the gas

line before and after the recombiner. At the end of the gas line was a second mass flow controller to record the flow rate as the gas left the gas processing line.

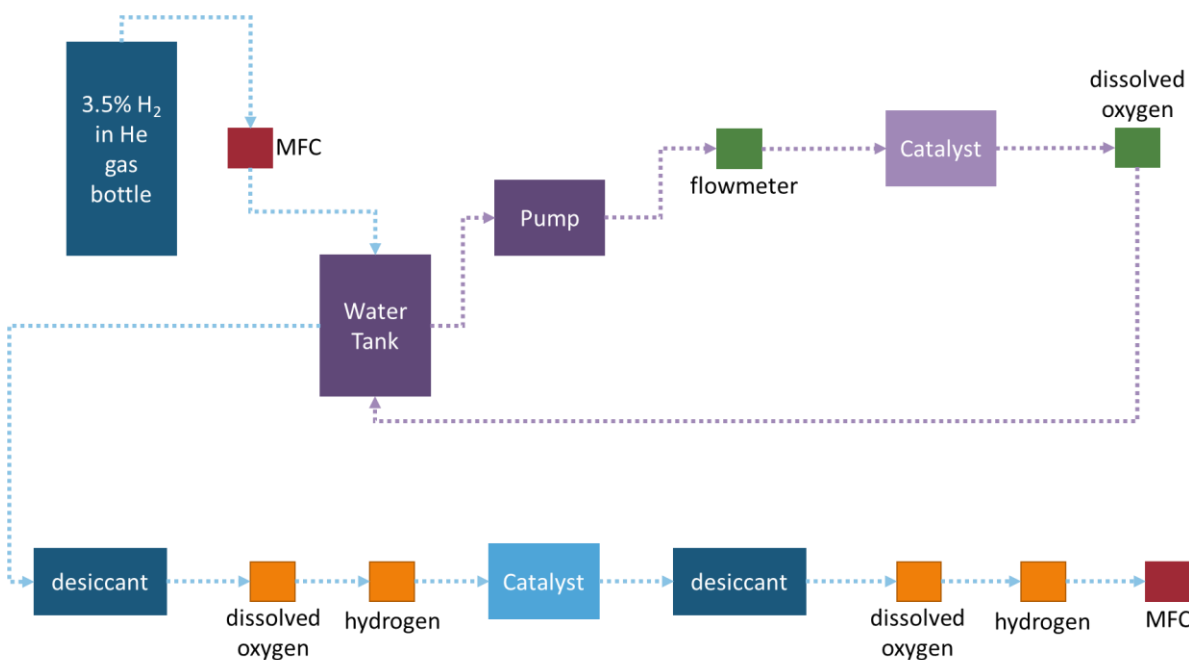


Figure 5.2: A simple schematic diagram of the small-scale water system used for testing of the catalytic hydrogen recombiner. The purple loop represents the flow of water and the blue line represents the flow of gas.

In order to simulate a system containing similar levels of H₂ and O₂ as seen in previous irradiation experiments, a carrier gas composed of 3.46% H₂ in He was used and small volumes of H₂O₂ were injected into the water system at known time intervals. The catalyst decomposed the H₂O₂ to produce O₂. Several initial tests were performed with excess oxygen in the system to demonstrate the efficiency of recombination in the ideal case. To perform these tests, the carrier gas was set to a flow rate of approximately 1.3 L/min. The system was run for 4 hours and each hour, 50 mL of H₂O₂ was injected into the system through a syringe. During these tests, the tank was opened for the injection of H₂O₂, allowing atmospheric air to enter the tank and increasing the concentration of O₂ to levels much higher than expected during irradiation. Following those

tests, trials with oxygen as the limiting reagent were performed in order to test the ability of the catalyst to remove hydrogen from the system under various conditions. These tests were performed under conditions with similar percentages of hydrogen and oxygen present in the gas stream in previous irradiation experiments. The same carrier gas was set at approximately the same flow rate. However, only 10-15 mL of H₂O₂ were added every 1 to 1.5 hours without opening the water tank. Therefore, no atmospheric air was added to the headspace of the tank to falsely increase the concentration of O₂. The results of the concentrations of both hydrogen and oxygen before and after the catalyst were compared in all situations and the stoichiometric ratio of hydrogen to oxygen was determined for each trial.

5.2.2 Hydrogen Recombiner Testing Results

The preliminary testing of the OxiGone catalyst demonstrated the efficient removal of hydrogen by a hydrogen recombiner in a small-scale water system and gas-processing line. In Figure 5.3, the results of hydrogen concentration measured before and after the catalyst are represented by the blue and red lines. The green line represents the oxygen concentration before the catalyst, which reacted with the hydrogen.

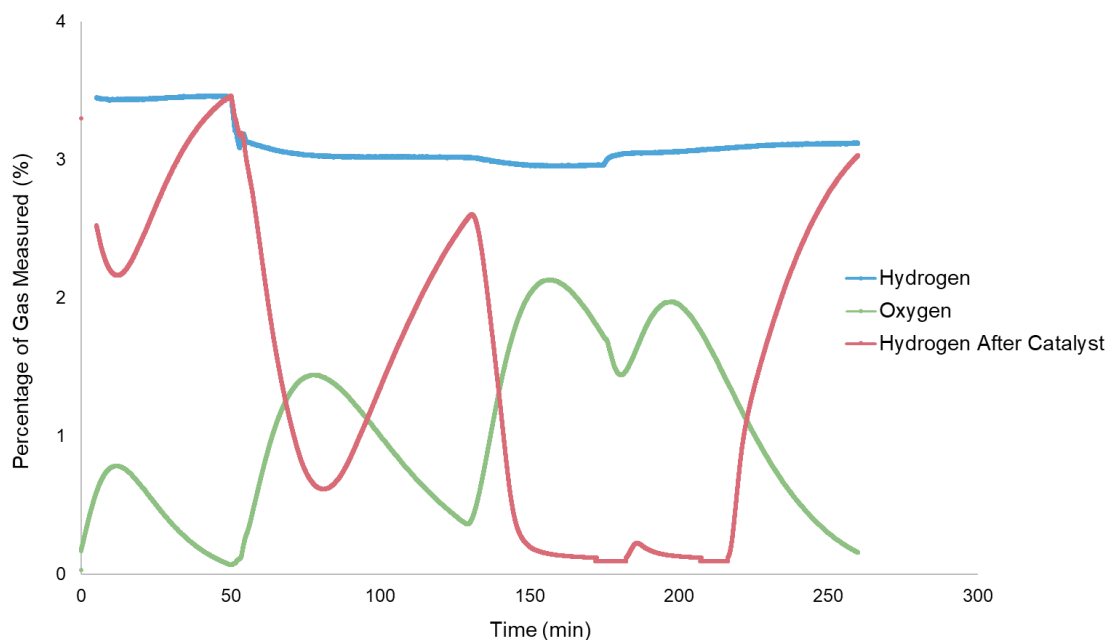


Figure 5.3: Results of the hydrogen concentration in the gas phase before (blue) and after (red) the catalyst in comparison to the oxygen concentration that passed through the catalyst (green).

Four separate volumes of 10 mL of H_2O_2 were injected into the water in a completely closed system during this test, which can be seen by the four increases in O_2 concentration in Figure 5.3. Each instance of increasing the O_2 concentration was matched with a resulting decrease in H_2 concentration, eventually leading to the complete removal of H_2 from the gas stream when the O_2 concentration reached above 1.8%. Therefore, the catalyst worked as expected – once the oxygen level reached a concentration above the stoichiometric ratio of 1 molecule of O_2 to 2 molecules of H_2 and was no longer the limiting reagent, hydrogen removal (within the error of the hydrogen sensor measurement) was achievable. As the system was depleted of hydrogen, oxygen breakthrough was observed as shown in Figure 5.4.

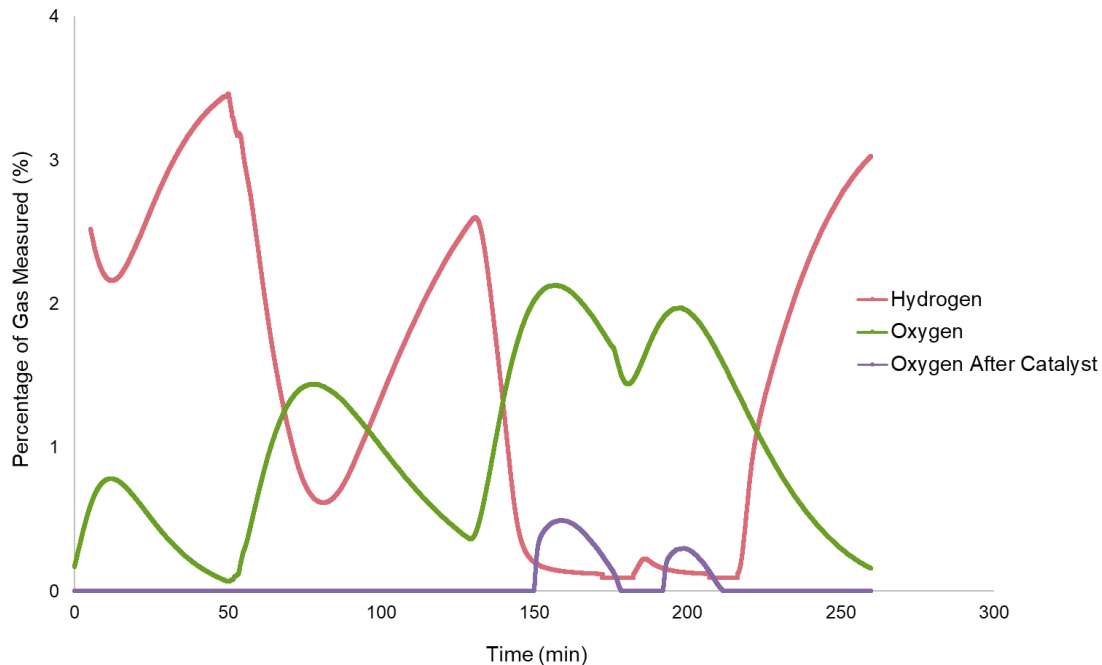


Figure 5.4: Results of the oxygen concentration before (green) and after (purple) the catalyst in comparison to the hydrogen concentration that passed through the catalyst (red).

The relationship between the decrease in H_2 with increasing O_2 was demonstrated by observing the concentration of each gas during the first two injections of H_2O_2 (where oxygen was still the limiting reagent). During these trials, there was a linear relationship with slopes averaging around -1.8 shown in Figures 5.5a and 5.5b. This slope can be related to the stoichiometric relationship between hydrogen and oxygen in the reaction of recombination. A slope of -1.8 means that 1.8 moles of hydrogen reacted with each mole of oxygen in the catalyst yielding a recombination efficiency of 90% when oxygen was the limiting reactant.

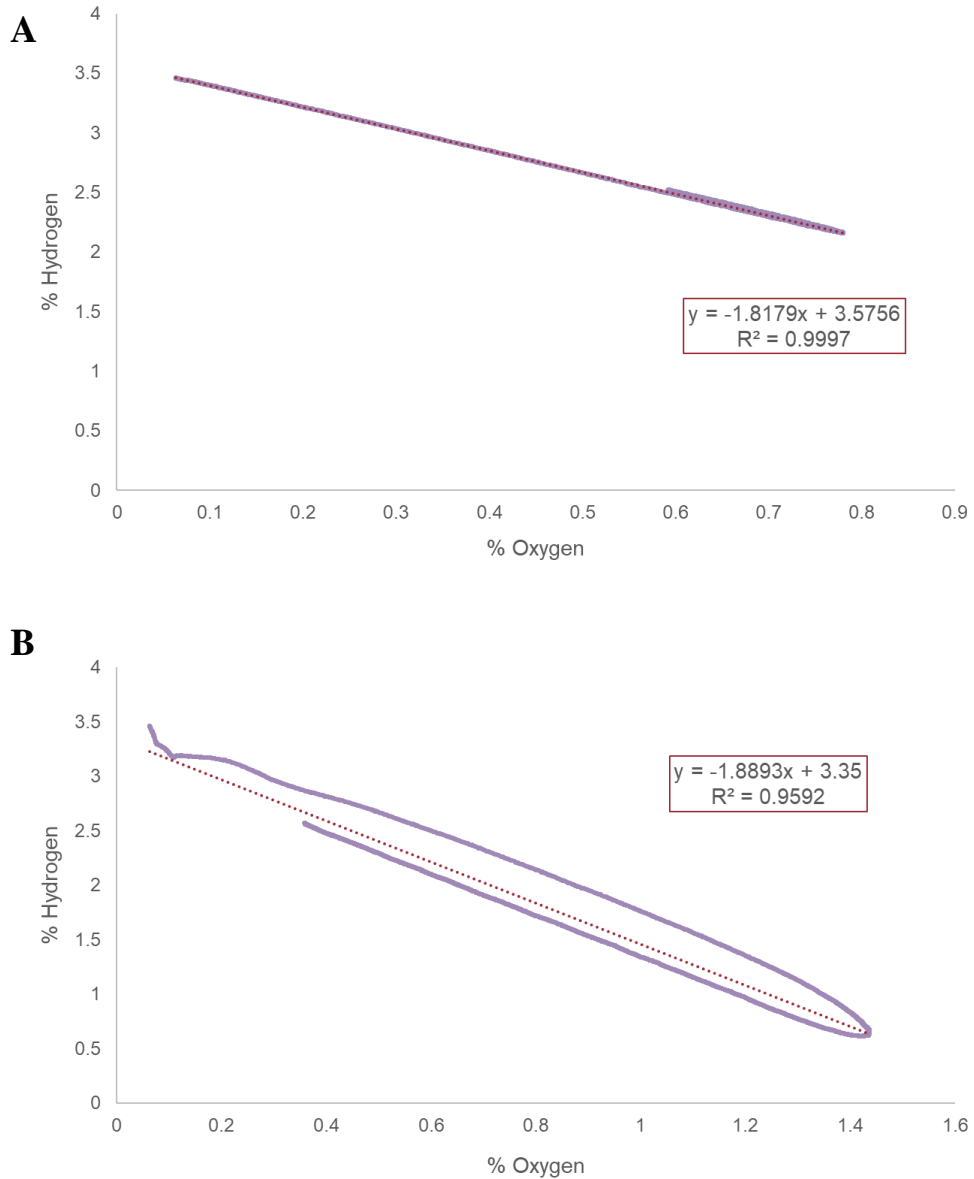


Figure 5.5: Demonstration of the relationship between decreasing output H_2 with increasing input O_2 concentration. (A) includes the data resulting from the first injection of H_2O_2 and (B) includes data from the second injection.

The change in hydrogen concentration per incoming oxygen level for each measured value over the entire test was also calculated using the following Equation 5.2:

$$\frac{H_{2(f)} - H_{2(i)}}{O_{2(i)}} \quad (\text{Equation 5.2})$$

where $H_{2(f)}$ was the concentration of hydrogen after the catalyst, $H_{2(i)}$ was the concentration of hydrogen before the catalyst, and $O_{2(i)}$ was the concentration of oxygen passing through the catalyst to react with the hydrogen. The values were averaged across the entire test period and resulted in a value of -1.7 ± 0.4 , which could be used as a rough prediction of the decrease in hydrogen concentration when using the catalyst. This value is also related to the stoichiometric relationship between hydrogen and oxygen in the recombination reaction.

5.2.3 Hydrogen Recombiner Testing Conclusions

Preliminary testing of the OxiGone catalyst used as a hydrogen recombiner in the harvesting system demonstrated the feasibility of decreasing the hydrogen and oxygen concentrations during irradiation experiments. While these tests did not determine the optimal conditions for the use of the catalyst in the system, the efficiency of hydrogen removal through recombination with oxygen was apparent.

Looking back at the hydrogen and oxygen measurements collected during the ^{48}Ca high-intensity irradiation, a prediction was made to roughly determine the concentration of hydrogen if the catalyst had been used (Figure 5.6). Instead of a maximum of 2.7% hydrogen in the gas stream and an average of 1.6%, the maximum would have been around 1.5% with an average of 0.7% hydrogen in the gas stream. In addition, most of the oxygen would have been depleted as it would have reacted with the excess hydrogen in the system.

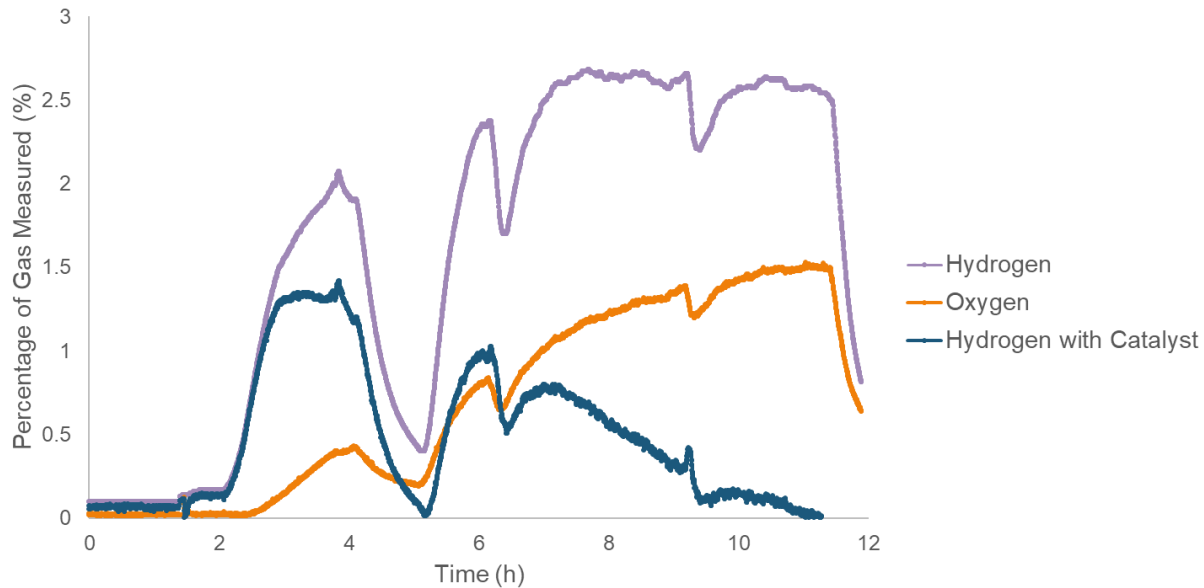


Figure 5.6: The prediction of hydrogen concentration during the ^{48}Ca high-intensity irradiation with the use of the catalyst for hydrogen recombination in comparison to the measured values.

As indicated by the data in Figure 5.6, the rate of O_2 radiolysis production is slower than that of H_2 radiolysis production at the beginning of the irradiation period. During this period, oxygen is the limiting reagent in the recombination reaction and only some of the hydrogen is removed. As the irradiation progresses, the H_2 concentration begins to saturate, while the rate of O_2 production continues to increase. During this period of irradiation, efficient removal of H_2 from the system is possible when oxygen reaches the maximum of 1.5%, and stays more than two times the concentration of hydrogen. Because of this requirement, it has been proposed to manually add oxygen to the harvesting system during irradiation to increase the recombination of hydrogen if necessary; however, more analysis into this proposal should be performed.

5.3 Metal Organic Frameworks for Gas Collection

The second improvement to the gas processing line involves utilizing a more novel approach for noble gas separation by metal-organic frameworks (MOFs). MOFs are a class of hybrid crystalline structures that consist of either metal ions or clusters that are coordinated to organic ligands. Various MOF structures and properties can be attained based on the metal ions and organic linkers used. These structures are known for comprising reticular chemistry that can be tailor-made for certain functions. Some of these functions include gas storage, gas purification, and gas separation. It is relatively simple to tailor MOFs to the needed architecture by post-synthetic modifications through the exchange of organic linkers and metal exchange, and the best structure for a specific function can be predicted through Monte Carlo simulations and screening the vast number of options.

Recently, MOFs have been used during the reprocessing of used nuclear fuels. This recycling process has the advantage of limiting the amount of radioactive waste that is produced from nuclear fuels, but yields volatile radionuclides, such as the noble gases of xenon and krypton. These gaseous radionuclides must be captured before they are released into the environment, and MOFs are a promising replacement of the currently used, expensive cryogenic distillation methods. Noble gas separation with MOFs is possible by synthesizing structures with pore sizes which will selectively capture molecules that have a specific atomic radius. The size of the atomic radius of each noble gas increases down the periodic table. The pore size and shape within an MOF structure is dependent upon the coordination of the metal chosen as well as the number of ligands which will bind to that metal and in what orientation.

In the literature, many studies have been reported to optimize the architecture of MOFs in order to improve the function of noble gas capture, specifically that of both xenon and krypton.

One such set of MOF's that shows promise for the selective adsorption of krypton is the SIFSIX-3-M series. The SIFSIX-3-M series falls under a subcategory of MOFS called hybrid ultra-microporous materials (HUMs), which consist of a 2D net formed by a metallic center connected by dipyritylacetylene ligands and then extend to a third dimension with inorganic pillars made of SiF_6^{2-} . SIFSIX-3-M can be tailored for the collection of krypton through the substitution of different metal centers – one being copper.

5.3.1 The Potential of SIFSIX-3-Cu MOF for Gas Collection

A study by Elsaidi *et al.* demonstrated the stability of SIFSIX-3-Cu under high levels of radiation as well as the MOFs selectivity for krypton over nitrogen. In this study, the testing was done to mimic conditions observed during used nuclear fuel reprocessing with a mixture of gases including CO_2 , N_2 , O_2 , Kr, and Xe. Therefore; a two-bed breakthrough set up was used to preferentially remove Xe and CO_2 in the first column and selectively absorb Kr over N_2 and O_2 on the second. In the harvesting system, a He carrier gas was used to remove the possibility of competitive adsorption because most MOFs are more selective of Kr over He. When undergoing irradiation to produce Kr, Xe will not be produced in the water-filled target. The main competitors will be O_2 and H_2 from radiolysis in the harvesting system.

SIFSIX-3-Cu was exposed to 0-200 kGy of gamma radiation with a ^{60}Co source and was determined to be the most stable under radiation conditions compared to other SIFSIX-3-M metal centers. A single-bed breakthrough experiment with a mixture of Kr, N_2 , and O_2 demonstrated the ability of SIFSIX-3-Cu to selectively adsorb Kr out of the mixture.

As SIFSIX-3-Cu appears to be a promising novel method of Kr collection, ongoing work into the synthesis and characterization of the MOF at Michigan State University and Lawrence Livermore National Laboratory is underway. There are future plans to test the MOF in the

harvesting system during cold tests using a residual gas analyzer to quantify noble gases and eventually during irradiation experiments at FRIB.

5.4 Conclusions

The experiments described in previous chapters of this work have provided insight on the physical and chemical behavior in both the aqueous and gaseous phases of the harvesting system. Through this work, target materials have been tested, radiolysis production has been measured, and the first true test of the gas-phase harvesting capabilities at the NSCL and FRIB was demonstrated. And following the analysis of the data from these experiments, there were several potential areas of improvement including the decrease of hydrogen radiolytically produced in the system for safety and the use of a more tailored method of gas collection to increase trapping efficiency.

The testing of a catalyst for hydrogen recombination resulted in the successful removal of hydrogen from a small-scale system. However, this testing was solely preliminary and more testing must be done in order to implement the hydrogen recombiner into the system during irradiation experiments.

Initial research into MOFs for the collection of krypton gas has led to a promising candidate: SIFSIX-3-Cu. This MOF has demonstrated resilience to radioactivity and selectivity of krypton in the literature; however, there has been no testing of the MOF with the harvesting system. There is ongoing work into the synthesis and characterization of SIFSIX-3-Cu as well as plans to test the MOF in a small-scale harvesting system with gas processing line. These improvements to the gas processing line will increase the likelihood of success for gas-phase harvesting at FRIB.

REFERENCES

REFERENCES

- 1) Abel, E. P.; Isotope Harvesting of Aqueous Phase Ions from Heavy-Ion Fragmentation Facilities for the Production of a $^{47}\text{Ca}/^{47}\text{Sc}$ Generator, Ph.D., Michigan State University, **2020**.
- 2) Sandeep, K. C.; Bhattacharyya R.; Warghat, C.; Bhanja, K.; Mohan, S. Experimental Investigation on the Kinetics of Catalytic Recombination of Hydrogen with Oxygen in Air. *International Journal of Hydrogen Energy*, **2014**, *39* (31), 17906-17912.
- 3) Research Catalysts, Inc. Products. [Online] <https://www.catalyst-central.com/product> (Accessed 2021).
- 4) Banerjee, D.; Thallapally, P. K.; et al. Potential of Metal Organic Frameworks for Separation of Xenon and Krypton. *Accounts of Chemical Resesarch*. **2014**, *48* (2), 211-219.
- 5) Banerjee, D.; Simon C. M.; Plonka, A. M.; Motkuri, R. K.; Liu J.; Chen, X.; Smit, B.; Parise, J. B.; Haranczyk, M.; Thallapally, P. K. Metal-organic framework with optimally selective xenon adsorption and separation. *Nature Communications*, **2016**, DOI: 10.1038/ncomms11831.
- 6) Parkes, M. V.; Staiger, C. L.; Perry IV, J. J.; Allendorf, M. D.; Greathouse, J. A. Screening metal-organic frameworks for selective noble gas adsorption in air: effect of pore size and framework topology. *Phys. Chem. Chem. Phys.* **2013**, *15*, 9093 – 9106.
- 7) Shekhah, O.; Belmabkhout, Y.; Chen Z.; Guillerm, V.; Cairns, A.; Adil, K.; Eddaoudi, M. Made-to-order metal-organic frameworks for trace carbon dioxide removal and air capture. *Nature Communications*, **2014**, DOI: 10.1038/ncomms5228.
- 8) Elsaidi, S. K.; Mohamed, M. H.; Helal, A. S.; Galanek, M.; Pham, T.; Suepal, S.; Space, B.; Hopkinson, D.; Thallapally, P. K.; Li J. Radiation-resistant metal-organic framework enables sufficient separation of krypton fission gas from spent nuclear fuel. *Nature Communications*, **2020**, *11*, 3103.

VI. Conclusions and Future Work

6.1 Conclusions

As the Facility for Rare Isotope Beams (FRIB) prepares to come online for experimental use and the beam dump is developed for harvesting opportunities in the future, testing must be performed on the proposed materials of the beam blocker and harvesting system as well as on the harvesting capabilities of the proposed design. In order to achieve this testing under similar conditions to the FRIB facility, two iterations of a beam blocker made of the proposed Ti64 alloy (grade 5 alloy: 6% Al, 4% V, mass balanced with Ti) and two iterations of a water harvesting system made up of similar components to the beam dump were tested in a series of irradiation experiments at the National Superconducting Cyclotron Laboratory (NSCL) as a function of beam power.^{1,2}

During a low intensity (0.1-0.4 pA) 140 MeV/nucleon ^{40}Ca irradiation, the durability of the Ti64 alloy material was tested and proved sturdy enough to withstand irradiation for 4 hours. The material was also resistant to the chemical environment that was produced in the water due to the beam interactions. The overall environment of the water was observed during this experiment and important preliminary data was collected on the radiolytic production of hydrogen at low intensity beam current.¹

During another low intensity (0-4 pA) 150 MeV/nucleon ^{78}Kr irradiation, a beam blocker more similar in design to the FRIB beam dump blocker was developed and tested to study the feasibility of gas-phase harvesting with the water system. A gas processing line was designed to remove unwanted gases from the gas stream while trapping the desired ^{76}Kr and ^{77}Kr radioisotopes online. This experiment demonstrated successful gas-phase harvesting of krypton

isotopes to generate ^{76}Br and ^{77}Br as 7.2(1) MBq of ^{76}Kr and 19.1(6) MBq of ^{77}Kr were collected during the 11-hour irradiation. A model of the mass transport of krypton through the system was created based upon real-time gamma spectroscopy measurements that were collected during the irradiation. From the model, the production rates of ^{76}Kr and ^{77}Kr were determined to be $2.7(1) \times 10^{-4}$ nuclei of ^{76}Kr and $1.18(6) \times 10^{-2}$ nuclei of ^{77}Kr formed per incident ^{78}Kr ion. The knowledge learned from this experiment was used to begin making improvements to the system in preparation for FRIB experiments.

The use of a catalyst to recombine hydrogen and oxygen in the system to resolve potential safety concerns during experiments of higher intensity was studied and resulted in the successful removal of hydrogen and even the depletion of hydrogen when the correct ratio of oxygen is also present in the system.³ Secondly, a more novel method of gas collection is currently being explored. Metal-organic frameworks (MOFs) can be tailored for specific purposes and have the potential increase the selectivity of krypton or other noble gas capture to increase collection efficiencies, especially at FRIB where the concentration of the desired gas in the rest of the gas stream will most likely be very low.⁴⁻⁶

Through this work, target materials have been tested, radiolysis production has been measured, and the first true test of the gas-phase harvesting capabilities at the NSCL was demonstrated. The insight gained from the experiments performed here will lead to successful gas-phase harvesting experiments at FRIB to produce and collect noble gas generators.

6.2 Future Work

The improvements to the gas processing line of the water system have only been studied through preliminary testing in this work. In order to successfully implement the hydrogen recombiner into the system, more testing should be done to determine the best flow rate of gas

through the gas processing line to still allow for the recombination of hydrogen and oxygen, but also allow for successful gas collection in the traps. Additionally, long-term cold testing of the catalyst material should be performed as well as testing during a low intensity irradiation experiment to ensure the durability of the catalyst under irradiation conditions. While the literature has demonstrated that the MOF, SIFSIX-3-Cu, exhibits the necessary characteristics in order to be used in the gas processing line, the MOF has not been tested in the harvesting system.^{7,8} Continuation of the synthesis and characterization of SIFSIX-3-Cu at Michigan State University will provide more MOF material for testing purposes. Cold testing of the adsorption kinetics of krypton on SIFSIX-3-Cu through a small-scale gas processing line should be performed using a residual gas analyzer (RGA), which ionizes a small fraction of gas molecules and the resulting ions are separated, detected, and measured according to their molar masses. The optimal column loading procedure should also be determined as MOFs are sensitive to the air and all of the adsorption sites may become occupied by unwanted air molecules prior to use in the gas collection line. And finally, the MOF should be tested during an irradiation to determine the collection efficiency of krypton and compare the results to the results presented here.

When FRIB becomes available to experimental users, there will be several beams of interest for further testing the gas processing line. Some examples are presented in Table 6.1.⁹ Radioisotopes of noble gases such as Kr, Xe, and Rn, which have applications in fields of medicine and biochemistry, will be produced in large quantities at FRIB and can be harvested from the gas phase. Radon-211 is a particular radioisotope of interest because it decays into astatine-211, a highly desired radionuclide for medical research. The current production methods limit production of ²¹¹At to a few specific institutions with the proper equipment and the relatively short half-life of ²¹¹At (7 h) limits the distance the isotope can be distributed for use.

Using a $^{211}\text{Rn}/^{211}\text{At}$ generator production method increases possibilities. At FRIB, ^{211}Rn will be produced when using a stable ^{238}U beam for irradiation.⁹ The testing performed in this work of the current harvesting system to produce a $^{76/77}\text{Kr}/^{76/77}\text{Br}$ generator system has implications for the future of a $^{211}\text{Rn}/^{211}\text{At}$ generator produced by FRIB. The techniques and methods learned during the experiments at the NSCL will assist in the transition of gas-phase harvesting of other noble gases during FRIB irradiations.

Table 6.1: Examples of possible gaseous radioisotopes for harvesting at FRIB.⁹

Element	Mass #	$t_{1/2}$	Research Field	Beam	Production Rate
Kr	76	14.8 h	Medicine	^{78}Kr	9.3×10^4 MBq/d
Kr	77	71.25 m	Materials, biochemistry	^{78}Kr	2.5×10^5 MBq/h
Xe	122	20 h	Medicine	^{124}Xe	1.0×10^5 MBq/d
Rn	211	14.6 h	Medicine	^{238}U	1.6×10^4 MBq/wk

REFERENCES

REFERENCES

- 1) Abel, E. P.; Isotope Harvesting of Aqueous Phase Ions from Heavy-Ion Fragmentation Facilities for the Production of a $^{47}\text{Ca}/^{47}\text{Sc}$ Generator, Ph.D., Michigan State University, **2020**.
- 2) Domnanich, K. A.; Abel, E. P.; Clause, H. K.; Kalman, C.; Walker, W.; Severin, G. W. An Isotope Harvesting Beam Blocker for the National Superconducting Cyclotron Laboratory. *Nucl. Instruments Methods Phys. Res. Sect. A Accel. Spectrometers, Detect. Assoc. Equip.* **2020**, 959 (November 2019), 163526.
- 3) Research Catalysts, Inc. Products. [Online] <https://www.catalyst-central.com/product> (Accessed 2021).
- 4) Banerjee, D.; Thallapally, P. K.; et al. Potential of Metal Organic Frameworks for Separation of Xenon and Krypton. *Accounts of Chemical Resesarch.* **2014**, 48 (2), 211-219.
- 5) Banerjee, D.; Simon C. M.; Plonka, A. M.; Motkuri, R. K.; Liu J.; Chen, X.; Smit, B.; Parise, J. B.; Haranczyk, M.; Thallapally, P. K. Metal-organic framework with optimally selective xenon adsorption and separation. *Nature Communications*, **2016**, DOI: 10.1038/ncomms11831.
- 6) Parkes, M. V.; Staiger, C. L.; Perry IV, J. J.; Allendorf, M. D.; Greathouse, J. A. Screening metal-organic frameworks for selective noble gas adsorption in air: effect of pore size and framework topology. *Phys. Chem. Chem. Phys.* **2013**, 15, 9093 – 9106.
- 7) Shekhah, O.; Belmabkhout, Y.; Chen Z.; Guillerm, V.; Cairns, A.; Adil, K.; Eddaoudi, M. Made-to-order metal-organic frameworks for trace carbon dioxide removal and air capture. *Nature Communications*, **2014**, DOI: 10.1038/ncomms5228.
- 8) Elsaidi, S. K.; Mohamed, M. H.; Helal, A. S.; Galanek, M.; Pham, T.; Suepal, S.; Space, B.; Hopkinson, D.; Thallapally, P. K.; Li J. Radiation-resistant metal-organic framework enables sufficient separation of krypton fission gas from spent nuclear fuel. *Nature Communications*, **2020**, 11, 3103.
- 9) Abel, E. P.; Avilov, M.; Ayres, V.; Birnbaum, E.; Bollen, G.; Bonito, G.; Bredeweg, T.; Clause, H.; Couture, A.; DeVore, J.; Dietrich, M.; Ellison, P.; Engle, J.; Ferrieri, R.; Fitzsimmons, J.; Friedman, M.; Georgobiani, D.; Graves, S.; Greene, J.; Lapi, S.; Loveless, C. S.; Mastren, T.; Martinez-Gomez, C.; McGuinness, S.; Mittag, W.; Morrissey, D.; Peaslee, G.; Pellemoine, F.; Robertson, J. D.; Scielzo, N.; Scott, M.; Severin, G.; Shaughnessy, D.; Shusterman, J.; Singh, J.; Stoyer, M.; Sutherlin, L.; Visser, A.; Wilkinson, J. Isotope Harvesting at FRIB: Additional Opportunities for Scientific Discovery. *J. Phys. G Nucl. Part. Phys.* **2019**, 46 (10), 100501